CHALMERS

Sensorless scalar and vector control of a subsea PMSM

Master of Science Thesis

Dimitrios Stellas

Department of Energy and Environment
Division of Electric Power Engineering
Chalmers University of Technology
Göteborg, Sweden, 2013

THESIS FOR THE DEGREE OF MASTER OF SCIENCE

Sensorless scalar and vector control of a subsea PMSM

Dimitrios Stellas

Performed at: Chalmers University of Technology,
Göteborg, Sweden,
FMC Kongsberg Subsea,
Asker, Norway

Examiner: Professor Torbjörn Thiringer
Department of Energy and Environment
Division of Electric Power Engineering
Chalmers University of Technology
Göteborg, Sweden

Supervisor: Torbjørn Strømsvik
FMC Kongsberg Subsea
Asker, Norway

Department of Energy and Environment
Division of Electric Power Engineering
Chalmers University of Technology
Göteborg, Sweden, 2013

Sensorless scalar and vector control of a subsea PMSM

Dimitrios Stellas

Department of Energy and Environment
Division of Electric Power Engineering
Chalmers University of Technology
SE - 412 96 Göteborg, Sweden
Telephone: +46 (0) 31-772 1000

Chalmers Bibliotek, Reproservice
Göteborg, Sweden, 2013

Abstract

This thesis deals with the position-sensorless control of a subsea PMSM, which is fed by a remote VSD. Two V/f control alternatives are implemented for the startup of the PMSM and a sensorless vector controller is designed for operation at higher speeds.

Several simulations are performed, in order to investigate the performance of the implemented models and to determine the optimal control settings. The conclusions drawn from the simulation results are validated with measurements on a lab model.

The obtained results demonstrate that the implemented V/f control schemes can provide secure startup for the PMSM. The smoothness of the startup depends on the initial rotor position and on the load of the motor. One of the two V/f controllers accelerates the PMSM with significantly lower current, thanks to its ability to produce a more precise voltage reference.

During vector-controlled operation, maximum efficiency can be achieved and the response of the system to load disturbances is almost ideal. Furthermore, the implemented field-weakening algorithm can extend the speed range of the PMSM by up to 17.6% for the considered load.

Index terms: PMSM, sensorless, scalar control, vector control, V/f.

Acknowledgement

First of all, I would like to express my gratitude for the workplace and the equipment that were provided to me by the Division of Electric Power Engineering at Chalmers University of Technology.

I am grateful to my examiner at Chalmers, Professor Torbjörn Thiringer, for his valuable guidance and his insightful suggestions throughout this work.

Furthermore, I would like to thank Magnus Ellsén and Alvaro Bermejo Fernández for their help with the data acquisition system and Tarik Abdulahovic for his support with software issues.

I also wish to express my sincere thanks to Georgios Stamatiou for his supportive attitude and his knowledgeable advice throughout my master studies.

The financial support provided by FMC Kongsberg Subsea and the opportunity to conduct a part of this thesis in the company's facilities are gratefully acknowledged.

Many thanks go to my supervisor at FMC, Torbjørn Strømsvik, for his valuable support and guidance during this thesis.

I am also thankful to Morten Thule Hansen, whose contribution in the experimental part of this work was crucial, and Harald Bjørn Ulvestad, who kindly shared his knowledge and previous experience on the investigated system.

I also wish to thank Ola Jemtland, Vidar Kragset and Ragnar Eretveit for some useful and interesting technical discussions during this thesis.

Finally, I am deeply indepted to my family for their unceasing support and encouragement.

Dimitrios Stellas
Göteborg, 2013

.

Contents

List of symbols

a_c	Bandwidth of current controller
c_l	Stabilizer gain constant
e	Back-EMF
f	Electrical frequency
F_b	Voltage-boosting factor
i	Current
J	Moment of inertia
k	Gain
k_l	Proportional gain of stabilizer
L	Inductance
n_r	Mechanical speed (rpm)
n_p	Number of pole pairs
p_e	Electric power
R	Resistance
R_a	Active-damping resistance
t	Time
t_r	Rise time
T_e	Electromagnetic torque
T_L	Load torque
T_s	Sampling period
u	Voltage
θ	Transformation angle
κ	Sampling number
ϕ	Angular position
ϕ_0	Power factor angle
ψ	Flux linkage
Ψ_m	Flux linkage of magnets
ω	Electrical speed
Ω	Mechanical speed

List of abbreviations

AC	Alternating Current
DC	Direct Current
EMF	Electromotive Force
HPF	High-Pass Filter
IMC	Internal Model Control
LC	Inductive-Capacitive
LPF	Low-Pass Filter
$MTPA$	Maximum Torque Per Ampere
PI	Proportional-Integral
$PMSG$	Permanent Magnet Synchronous Generator
$PMSM$	Permanent Magnet Synchronous Motor
PWM	Pulse-Width Modulation
RL	Resistive-Inductive
VSD	Variable Speed Drive

List of subscripts

0	Initial value
a	Phase-a quantity
aw	Anti-windup
b	Phase-b quantity
c	Phase-c quantity
C	Cable parameter
$comp$	Compensating value
cor	Corrected value
cr	Critical value
d	Direct-axis quantity
e	Electrical quantity
est	Estimated value
gen	Generator
i	Integral
lim	Limited quantity
m	Mechanical quantity
max	Maximum value
p	Proportional
pr	Predicted value
q	Quadrature-axis quantity
r	Rotor quantity
$rated$	Rated value
s	Stator quantity
T	Transformer parameter
tr	Transmission system parameter
upd	Updated value

List of superscripts

$*$	Reference quantity
$'$	Equivalent quantity
s	Stationary-frame vector

List of accents

$\hat{}$	Peak value
$\bar{}$	Space vector

Chapter 1

Introduction

This chapter introduces the problem that is addressed in this thesis, presents some previous work that has been conducted on the investigated system and states the scope and the objectives of this thesis.

1.1 Problem background

Induction motors are the most traditional option for driving submersible pumps. However, as the oil production moves to deeper waters, it becomes necessary to consider alternatives that can facilitate higher performance.

PMSMs have the potential to meet the emerging challenges in subsea applications, thanks to positive features such as high efficiency, high power density and high-speed capabilities.

The VSDs that are used for the control of submersible PMSMs are often installed on oil platforms, which can be located several kilometers away from the subsea pumping activities. The long eletrical connection between the motor and the drive in these cases introduces new challenges in the control of the PMSM.

Although the control requirements of pump drives are usually low, the recent development of advanced pumping solutions calls for more efficient and precise motor regulation.

The new performance demands can be met by vector control, a control type which is usually applied in advanced drive systems, which require fast and accurate current and speed regulation. Typical examples of applications that use vector control can be found within the automotive industry.

The harsh operating conditions imposed by the deepwater environment of submersible PMSMs necessitate the sensorless operation of the applied control schemes. This means that the used vector controllers must not rely on mechanical measurements, but should have position-estimating capabilities.

Since the performance of position-sensorless vector control is usually problematic during the startup of the PMSM, a more traditional control type, called scalar control, can be used during the low-speed operation of the system.

1.2 Previous work

The offshore system considered in this thesis consists of a submersible motor, which is remotely controlled by a VSD through a transmission system. The transmission system consists of a step-up transformer, a long cable and a step-down transformer.

A small-scale lab model of this system was designed and implemented as part of a previous work [1]. Computer simulations were also performed during the same work, in order to study the startup performance of the downscaled system under scalar control. A separate task included the setup of the scalar and vector control configurations in the VSD of the lab model.

Since the measurements that are presented in this thesis were taken on the small-scale lab model and since the aforementioned drive configurations were used to control the PMSM during the performed experiments, it is clear that the experimental tasks performed in this thesis are based on previously conducted work.

The control schemes implemented in this thesis are mainly based on concepts that have been found in literature. The designed models have resulted from the combination of ideas from different papers and the adaptation of these ideas to the peculiarities of the investigated system.

1.3 Purpose and scope

The first objective of this thesis is to develop sensorless scalar and vector control models for the studied system and to simulate their performance both during the startup and during high-speed operation of the PMSM. The modeling and the simulations are performed with MATLAB and Simulink.

Since this work focuses on the development of control schemes, the modeling of the physical components is not handled in detail. The PMSM model is obtained from the SimPowerSystems toolbox and the transmission system parameters are integrated into the motor parameters. The VSD and its output filter are represented by a simplified interface between the control circuit and the power circuit.

The second objective of this thesis is to verify the results of the simulations with measurements on the lab model of the system. The preparation for these measurements includes the development of a data-acquisition system, which can be used to monitor different quantities during the conducted experiments. The implemented monitoring system is based on LabVIEW and CompactRIO.

Chapter 2

Theoretical background

This chapter presents some theoretical considerations that are related to the studied system. The increasingly important role of PMSMs for subsea operations is discussed and different options for the placement of drives in offshore applications are presented.

In cases where the submersible motor is controlled by a remote VSD, the combination of the PWM voltage output of the drive and the long cable connection between the motor and the drive introduces certain challenges, which are discussed in this chapter.

Finally, some theoretical background about the sensorless scalar and vector control of PMSMs is presented and the combination of these two control types is introduced, as a way to achieve safe motor startup and high control performance during high-speed operation.

2.1 Motors for subsea applications

PMSMs have positive features that make them popular in a variety of applications. When it comes to deepwater pumping operations, the advantages of PMSMs become even more significant, as explained in this section.

Due to the high deepwater pressures involved, subsea motors typically operate with fluid-filled mechanical gaps. The presence of pressurized fluid between the rotor and the stator helps the motor withstand the high pressure of its subsea surroundings, but also results in increased friction and causes higher drag losses, compared to the case of air-filled gaps.

Whereas the electrical losses are dominant in conventional motors with air-filled gaps, this is not the case for motors that operate subsea. The highly effective cooling that is available in subsea applications makes the impact of the electrical losses less significant, compared to that of frictional losses [2].

A typical breakdown of the total losses in this case shows that approximately 70% of them are drag losses, almost 20% are losses from the impeller which circulates the fluid and only 10% are electrical losses [3].

Apparently, the high drag losses pose severe limitations in the operating speed of motors

with fluid-filled gaps. Since high speeds are increasingly important for subsea pumping applications [2], it is crucial to decrease the frictional losses in submersible motors.

Induction motors have been traditionally used in subsea applications, thanks to their simplicity, robustness and low cost. However, as the oil production moves to deeper waters [4], it becomes harder for them to meet the increased speed and efficiency requirements, mainly because their need for a small mechanical gap results in high frictional losses.

PMSMs on the other hand, can be constructed with much larger mechanical gaps, which results in higher efficiency and greater speed capabilities. Their decreased sensitivity to larger gaps allows smaller rotor diameters and extra space for the placement of a sleeve in the fluid-filled gap of the motor [2].

Additionally, the absence of rotor windings or conductive bars in PMSMs eliminates the resistive rotor losses. This allows even higher efficiencies and superior thermal performance compared to induction motors.

Apart from their high efficiency and high speed capabilities, PMSMs are characterized by high power density, compact size and low weight [5, 6]. Their construction is simple and the absence of brushes results in higher robustness and lower maintenance needs [7].

On the negative side, the high cost of the permanent magnets increases the overall cost of PMSMs [8]. Moreover, the risk of magnetic property loss makes the reliability of this motor type questionable under certain circumstances [6].

2.2 Drives for submersible motors

The use of VSDs for the control of submersible motors improves the reliability and the efficiency of pumping operations.

This section presents different options regarding the placement of the drive and discusses some problematic issues that arise from the combination of the PWM voltage generated by the VSD and the long cable that connects the motor and the drive.

2.2.1 Placement of the drive

The VSDs that are used for the control of submersible motors can be placed either on the seabed, in the vicinity of the controlled motor [9], or on a platform, which might be located several kilometers away from the actual pumping activity [10, 11].

Placement in low-pressure subsea enclosures

In the first case, the drive is enclosed in a vessel, which is installed subsea. Since power electronic converters that are based on present technology cannot withstand high-pressure environments, the interior of the drive vessel needs to be at low pressure [12].

Due to the high deepwater pressure, the drive enclosure in this case must be able to withstand a significant pressure difference between its interior and its subsea surroundings. For this reason, the walls of the used vessel need to be thick and heavy.

Naturally, the bulky design of the enclosure results in an increase in the size and cost of the drive system, but also in problematic heat dissipation [12]. Due to the thick walls of the vessel, the heat conduction from the power electronic components to the sea water becomes more difficult, which results in higher operating temperatures for the drive.

Placement on the platform

The second option is to install the converter on a platform. Although the topside environment eliminates the necessity of a large and costly enclosure, it introduces the need for a long electrical connection between the VSD and the controlled PMSM [10, 11].

In order to decrease the transferred current and thus reduce the transmission losses and the voltage drop in the cable connection, higher transmission voltage levels are needed for longer step-out lengths. For this reason, a topside transformer can be used to step up the voltage output of the VSD.

In this case, either the submersible PMSM needs to operate at the voltage levels of the transmission system [1], or an additional transformer needs to be installed on the seabed, so that the transmitted voltage can be stepped down before reaching the motor. In the framework of this thesis, the latter alternative is considered.

A potential drawback of this solution is that the control of the PMSM through the transmission system could introduce new filtering requirements [13]. More specifically, the transmission of the PWM pulses of the drive through the long cable could subject the windings of the PMSM to significant electrical stress, if the necessary measures are not taken. This issue is discussed in greater detail in Section 2.2.2.

Development of pressure-tolerant power electronics

The development of pressure-tolerant power electronics could facilitate the possibility of placing the drive in subsea enclosures of reasonable size and cost. The vessel in this case could be filled with a pressurized insulating liquid, which would improve the heat dissipation and would eliminate the differential pressure that the vessel would otherwise have to withstand.

The insulating liquid must protect the converter components from mechanical damage and electrical flashovers. It should have good dielectric and thermal properties, in order to provide reliable insulation and effective heat removal. It should be uncompressible and should have a uniform and stable structure, which would not cause any chemical reactions or change its character for any reason [12, 14].

A dielectric liquid, which has been tested for the described purpose and appears to have several desirable features, is Midel 7131. Its properties include high breakdown strength, low thermal expansion, high temperature stability, biodegradability and non-toxicity [14].

A strategy that has been proposed for the development of power electronic components that could withstand the high pressure of the insulating liquid is the removal of the insulating gas that originally surrounds the converter chips and its replacement with an uncompressible liquid. This liquid should ideally fill every void in the converter [12].

Although the development of pressure-tolerant power electronics could enable the placement of the VSD in high-pressure submersible enclosures in the future, such a solution is not an option for present applications.

2.2.2 Effects of PWM voltage

The PWM voltage produced by the topside VSD is transmitted through the cable to the submersible PMSM. The high-frequency voltage pulses generated by the inverter could have detrimental effects on the motor and the cable.

As discussed in this section, the effects of the PWM voltage may be quite severe in the investigated application, due to the long transmission distance and the subsea environment of the cable.

Impact of high-order harmonics

Compared to a purely sinusoidal voltage excitation, the PWM pulses that are supplied to the motor result in increased losses, mechanical vibrations, noise generation, higher electromagnetic emission, more severe insulation stress, and undesirable currents induced to the shaft and bearings of the motor [15, 16].

The high-order harmonics of the PWM voltage induce high-frequency currents and thus create minor hysteresis loops in the steel of the motor. These currents are the cause of additional losses, which reduce the efficiency of the system and result in higher operating temperatures. Furthermore, the interaction of the induced currents with flux harmonics may result in stray forces that cause mechanical vibrations and increase the generated noise [15].

Increasing the switching frequency of the drive is a way to reduce the harmonic content of the motor currents and thus mitigate the negative effects of the high-frequency current components. However, this also results in higher switching losses in the drive and increases the possibility of voltage overshoots in the motor terminals [17].

Voltage overshoots at the terminals of the motor

The high-frequency voltage pulses generated by the VSD cause travelling waves in the transmission cable between the drive and motor. When each travelling wave reaches the PMSM, voltage reflection occurs, due to the mismatch between the cable impedance and the motor impedance [18].

The magnitude of the reflected voltage depends on the cable length, the rise time of the pulses, the characteristic impedances of the motor and the cable, the propagation velocity

of the waves and the dielectric medium surrounding the cable [13].

Shielded cables and cables that are submersed in water have significantly higher capacitance than cables in air. This results in lower characteristic impedances for submersible cables and therefore a more significant mismatch between the cable impedance and the motor impedance [13].

Since the impedance of the motor is much higher than the one of the cable, the reflected wave is expected to be almost equal in magnitude to the incident wave. Since the voltage at the motor terminals is equal to the sum of the two waves, its magnitude is expected to reach twice the magnitude of the VSD voltage [19].

Due to the occuring voltage reflection phenomena, when the distance between the motor and the drive is long, as in the case of the investigated application, the voltage pulses at the motor terminals may be different than the ones generated by the drive.

More specifically, the distributed inductance and capacitance of the cable result in high-frequency voltage oscillations at the motor end of the cable. These oscillations are usually referred to as 'voltage ringing' [18].

Moreover, the high voltage derivatives experienced by the PMSM during PWM operation cause the voltage peaks to be unevenly distributed across the motor windings. In this case, the largest portion of the supplied voltage may appear between the first turns of the windings, thus causing the insulation of these turns to experience higher stress and faster degradation [17].

It can be concluded that the combination of voltage reflection and voltage ringing can cause the motor to experience voltages higher than twice the DC-link voltage of the VSD [17], while the high voltage derivatives can subject the motor windings to additional electrical stress.

If these phenomena are not taken into account during the design of the system, the repeated overvoltages can cause significant stress to the insulation of the motor and eventually reduce its lifetime.

Cable-charging current pulses

Every time the voltage output of the VSD changes, the distributed cable capacitance must be charged or discharged. This results in pulses of charging current that not only increase the losses of the system, but can also cause overcurrent problems in the inverter and affect the control performance of the drive [18].

The magnitude of the charging current is proportional to the derivative of the voltage supplied by the drive and to the cable capacitance. Since PWM pulses are characterized by rapid voltage variations and since the capacitance of submersible cables is large, the charging currents are expected to be high in the investigated application.

The frequency of the cable-charging current pulses depends on the frequency of the voltage pulses generated by the inverter. Therefore, for higher switching frequencies of the VSD, the distributed cable capacitance is charged and discharged more often, which increases the transmission losses of the system.

Mitigation of the PWM effects

Based on the aforementioned considerations, the combination of PWM operation and the long cable connection between the VSD and the PMSM can potentially cause significant stress to the insulation of the motor and decrease the efficiency of the system.

These negative issues can be mitigated by filtering the voltage that is generated by the VSD, or by eliminating the impedance mismatch at the end of the cable. There are different types of filters that can be used for these purposes, the most common ones being output line inductors, output limit filters, sine wave output filters and motor termination filters [18]. The cost and the effectiveness of the aforementioned solutions vary.

The use of sine wave filters has been suggested in several papers [13, 16, 19], as a way to eliminate the high-order harmonics of the PWM pulses and therefore supply the motor with almost sinusoidal voltage.

The advantages of this solution include the absence of transient overvoltages at the terminals of the motor, the elimination of power losses due to harmonic currents, the reduction of motor noise and the decrease of electromagnetic emission [19].

Moreover, when applications with submersible motors and long step-out distances are considered, the use of sine wave filters is expected to eliminate the negative phenomena that are associated with voltage reflection and high voltage derivatives [13].

A sine wave filter is essentially a LC filter, whose resonance frequency is much lower than the lowest harmonic frequency of the inverter voltage and much higher than the fundamental frequency of the system [16].

An alternative solution, which has been introduced as an effort to eliminate the requirement for filters, is the use of a multilevel inverter in the VSD [10]. The special topology of this inverter results in a significant reduction in the high-order harmonics at the output of the drive and eliminates several problems that are associated with common PWM voltage pulses.

2.3 Control of permanent magnet motors

Depending on the requirements of each application, different methods can be used to control PMSMs. This section introduces scalar control as a simple control method, which is suitable for low-cost drive systems, and vector control as a more advanced option, which is well-suited for applications that demand higher dynamic performance.

2.3.1 Scalar control

In drive systems where simple, low-cost control is desired and where reduced dynamic performance is acceptable, open-loop control methods can be used. Typical applications of such systems include pump and fan drives [20]. Open-loop control methods (or scalar control methods, as they are often called) exist in different variations, which include V/f schemes [21] and I-f schemes [22].

Despite their simplicity and their ability to operate over a wide speed range, it has been found that the performance of open-loop methods often depends on the motor parameters and the load conditions of the system. Such methods can experience power swings within specific speed ranges, which might cause the motor to lose synchronism [5].

Furthermore, the behaviour of some open-loop schemes is heavily dependent on the selected parameters of the controller. The selection of the control settings for these schemes is often based on a trial-and-error approach and is therefore quite time-consuming [21].

The term 'open-loop' often refers to the fact that no speed or position feedback is needed for the operation of these schemes. In this thesis however, this term is used to denote that neither electrical nor mechanical feedback is required by a controller.

For instance, a scalar control method which uses current feedback has been presented in [23]. Although this method does not require any position or speed measurements, it is called 'closed-loop' in this thesis, in order to differentiate it from schemes with no feedback at all.

2.3.2 Vector control

For more advanced drive systems, which require higher dynamic performances, vector control is a more appropriate option than scalar control. Demanding applications that need vector control can be found, for instance, within the automotive industry [20].

Vector control allows the torque and the flux of the PMSM to be controlled separately from each other, through a control structure which is similar to that of a separately excited DC machine [20]. This decoupled control results in the precise and efficient regulation of the motor.

However, a major issue with vector controllers is that their operation requires information about the rotor position and the speed of the PMSM. The most direct approach for obtaining this information, is the use of mechanical sensors on the shaft of the PMSM [24].

In many applications however, the presence of mechanical sensors is undesirable or unacceptable, since it increases the cost and the complexity of the system [25].

Numerous position-estimating techinques have been developed, as an effort to eliminate the need for mechanical sensors. The position estimation can be based, among others, on the flux linkage, the back-EMF or the inductance of the PMSM [26, 27]. The effec-

tiveness of these techniques is not universal, but depends on the motor topology and the application requirements.

Several proposed vector control schemes utilize flux-linkage-based estimation techniques [5, 21]. Such a technique has been described in [26] and is implemented in this thesis, after being adapted to the peculiarities of the investigated system. Variations of the implemented estimating algorithm have also been presented in [25, 28, 29].

Field-weakening algorithms are often integrated into vector control schemes, in order to allow the PMSM to operate above its rated speed. Several papers have presented theoretical considerations on field-weakening [30, 31] and have applied different field-weakening strategies [32, 33]. A field-weakening algorithm, which has been derived in [34], is implemented and tested in this thesis.

2.3.3 Combination of scalar and vector control

A problem with most position-estimating techniques is their inability to produce accurate estimates at zero speed. Due to this problem, the startup of PMSMs with position-sensorless vector controllers is often problematic, unless the initial rotor position is known [29].

A solution would be to bring the rotor to a known position before the actual acceleration [25]. This could be achieved by injecting a proper DC current into the windings of the PMSM, thus forcing the rotor to align in the desired direction. For the investigated system however, such a solution is not acceptable, since the presence of the transformers does not allow the injection of DC currents.

Due to the startup issue of position-sensorless vector controllers, scalar control schemes are often used for the initial acceleration of PMSMs [5, 22]. Provided that their control parameters are properly set, these schemes should be able to accelerate the PMSM for every initial rotor position [29]. After a certain speed is reached, the scalar controller can be dismissed and the position-sensorless vector controller can be deployed.

This well-known strategy is also applied in this thesis. Two V/f control alternatives are presented for the startup of the PMSM and a position-sensorless vector controller is implemented and tested for higher speeds of the motor. A vector control scheme with mechanical sensors is also designed, as an intermediate step before the implementation of the sensorless controller.

Chapter 3

System description

This chapter describes the models that have been implemented in this thesis and the considerations that determined their design. The described models correspond both to the power components and the drive controller of the studied system.

The considered power system consists of a PMSM, which drives a multiphase pump and which is fed by a remote VSD through a transmission system. The transmission system consists of a step-up transformer, a long cable and a step-down transformer. The topology of the system is shown in Fig. 3.1.

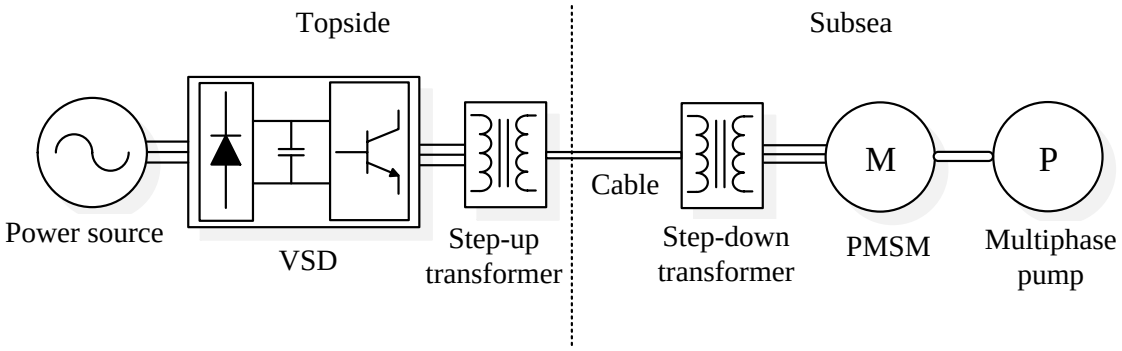

Figure 3.1: Topology of the investigated power system, consisting of a PMSM, which is connected to a pump and is fed by a remote VSD through a transmission system.

The controller of the VSD determines the voltage output of the drive and therefore the voltage input of the motor. The application of proper control schemes is essential, in order to achieve the required performance during different types of operation.

Two different V/f control models, an open-loop and a closed-loop model, are implemented for the initial acceleration of the PMSM and are presented in this chapter. The former one is simpler but the latter one provides higher control performance.

Moreover, two different vector control models are designed for higher operating speeds of the PMSM. In the first model a position sensor is present, while in the second model this sensor is eliminated, in order to decrease the cost and increase the robustness of the

system.

3.1 Permanent magnet synchronous motor

This section presents the equations which dictate the electrical and mechanical performance of the PMSM and provide the basis, not only for the implementation of the motor model, but also for the design of its control.

3.1.1 Electrical equations

It is generally convenient to express the electrical equations of the PMSM in the dq reference frame [35]. By using this representation, the steady-state AC quantities of the motor are transformed into DC values, which are easier to analyze and control.

The space vector of the stator voltage is denoted as $\bar{u}_s$ and is given by

$$\bar{u}_s = R_s \bar{i}_s + \frac{d\bar{\psi}_s}{dt} + j\omega_r \bar{\psi}_s \tag{3.1}$$

where R_s is the stator resistance, $\bar{i}_s$ is the space vector of the stator current, $\bar{\psi}_s$ is the space vector of the stator flux linkage and ω_r is the electrical speed of the motor. The stator flux linkage $\bar{\psi}_s$ is obtained from

$$\bar{\psi}_s = L_{sd} i_{sd} + j L_{sq} i_{sq} + \Psi_m \tag{3.2}$$

where Ψ_m is the amplitude of the flux linkage of the permanent magnets, L_{sd} and L_{sq} are the d-axis and q-axis stator inductances and i_{sd} and i_{sq} are the d-axis and q-axis currents respectively.

It can be observed from (3.2) that Ψ_m lies in the d direction, thus the magnetic axis of the PMSM is the same with the d axis of the selected dq frame. This is achieved by using a proper angle θ_r for the dq tranformations.

The back-EMF of the PMSM depends on the flux linkage Ψ_m and the speed ω_r. Its space vector $\bar{e}$ is given by

$$\bar{e} = j\omega_r \Psi_m \tag{3.3}$$

By combining (3.1) and (3.2), the d-axis and q-axis stator voltages, denoted as u_{sd} and u_{sq} respectively, can be obtained as

$$u_{sd} = R_s i_{sd} + L_{sd} \frac{di_{sd}}{dt} - \omega_r L_{sq} i_{sq} \tag{3.4}$$

$$u_{sq} = R_s i_{sq} + L_{sq} \frac{di_{sq}}{dt} + \omega_r L_{sd} i_{sd} + \omega_r \Psi_m \tag{3.5}$$

where the term $\omega_r \Psi_m$ represents the magnitude of the back-EMF vector $\bar{e}$, or equivalently, the amplitude of the three-phase back-EMF. It is important to note that, since

amplitude-invariant transformations are used in this thesis, the magnitudes of space vectors correspond to the amplitudes of three-phase quantities.

Next, the electromagnetic torque T_e of the motor can be calculated from

$$T_e = \frac{3n_p}{2} Im[\bar{\psi}_s^* \bar{i}_s] = \frac{3n_p}{2} [\Psi_m i_{sq} + (L_{sd} - L_{sq}) i_{sd} i_{sq}] \tag{3.6}$$

where n_p is the number of pole pairs. The values of the inductances L_{sd} and L_{sq} depend on the geometry of the motor and the placement of the permanent magnets [8, 36].

PMSM topologies with inset-mounted or interior-radial magnets are characterized by dq saliency, which results in a difference between L_{sd} and L_{sq}. On the other hand, in motors with surface-mounted magnets, the saliency is often negligible and the two inductances can be considered to be equal, thus $L_{sd} = L_{sq} = L_s$. In the latter case, (3.6) is simplified to

$$T_e = \frac{3n_p}{2} \Psi_m i_{sq} \tag{3.7}$$

The inductances L_{sd} and L_{sq} of the PMSM considered in this thesis differ slightly from each other. However, for the sake of simplicity, the difference between them is neglected and the simplified expression (3.7) is used for the calculation of the electromagnetic torque.

It is interesting to observe that the torque in (3.7) is proportional to the current i_{sq} and independent of i_{sd}. The current i_{sd} on the other hand, has a more significant effect on the stator flux linkage magnitude than i_{sq} according to (3.2), since the first one lies on the same axis with the main flux linkage component Ψ_m, while the second one lies on a perpendicular axis.

3.1.2 Mechanical equations

The equation that dictates the mechanical performance of the PMSM, by relating the electromagnetic torque T_e, the load torque T_L and the electrical speed ω_r, is

$$\frac{J}{n_p} \frac{d\omega_r}{dt} = T_e - T_L \tag{3.8}$$

where J is the moment of inertia of the system. The relation between the electrical speed and the electrical rotor position is given by

$$\frac{d\phi_r}{dt} = \omega_r \tag{3.9}$$

where ϕ_r corresponds to the angle between the magnetic axis of the motor and the a axis of the three-phase system.

In order to achieve perfect-field orientation, thus in order to align the magnetic axis of the PMSM with the d axis of the dq frame, the electrical rotor angle ϕ_r needs to be equal

to the selected dq-transformation angle θ_r, thus $\phi_r = \theta_r$.

The motor model which is used in this thesis is based on the electrical equations (3.4) - (3.6) and the mechanical equations (3.8) - (3.9).

3.2 Transmission system

The transmission system in the studied application consists of a step-up transformer, a cable and a step-down transformer. In order to reduce the computational complexity of the simulations and to simplify the selection of the control settings, the electrical parameters of the transmission components are integrated into the respective parameters of the PMSM.

3.2.1 Simplifying assumptions

The aforementioned treatment of the transmission system is facilitated by two basic assumptions.

Firstly, it is assumed that the short-line model can represent the cable of the system with adequate accuracy, thus the shunt capacitance of the cable can be ignored, without introducing any significant error. Under this assumption, which is generally valid for lines with length up to 80 km [37], the transmission cable can be modelled as an inductance L_C connected in series with a resistance R_C.

Secondly, it is assumed that none of the two transformers experience saturation, thus they are both considered to remain in the linear magnetic region under all operating conditions of the system. Under this assumption, the magnetizing branch of their equivalent circuit can be ignored and each transformer can be modelled as an inductance L_T connected in series with a resistance R_T.

3.2.2 Considerations on transformer saturation

In general, the core of a transformer gets saturated when the applied V/f ratio becomes too high. In such a case, the rise in the magnetic flux linkage of the transformer is accompanied by a disproportionally large increase in its magnetizing current and, therefore, a significant decrease in its magnetizing inductance.

Clearly, saturation is an undesirable condition for transformers and should be avoided by dimensioning their core properly, so that they remain in the linear magnetic region even for the maximum applied V/f ratio.

The aforementioned requirement bears particular significance for the studied application. As discussed in Section 3.3.3, the system has to operate at a high V/f ratio during the initial stage of the PMSM startup. This may lead to the inconvenient necessity of oversizing the transformer core for the sake of a few seconds of low-frequency operation.

The problem applies mainly to the topside step-up transformer, since the V/f ratio that is experienced by the subsea step-down transformer is lower, due to the voltage drop in the cable.

In order to minimize the size and cost of the topside transformer, it is necessary to optimize the control of the PMSM during the early stages of its startup, thus to find the minimum V/f ratio that can safely accelerate the motor.

3.2.3 Introduction of equivalent quantities

By neglecting the shunt capacitance of the cable and the magnetizing branch of the transformers, the transmission system can be simply modelled as a series RL circuit. Its resistance R_{tr} and and its inductance L_{tr} can be written as

$$R_{tr} = R_C + 2R_T \tag{3.10}$$

$$L_{tr} = L_C + 2L_T \tag{3.11}$$

respectively. Since the transmission system is connected in series with the stator windings of the PMSM, its parameters can be integrated into the motor parameters. In this case, the combination of the actual PMSM and the transmission system can be regarded as an equivalent PMSM, the parameters of which can be written as

$$R'_s = R_s + R_{tr} \tag{3.12}$$

$$L'_s = L_s + L_{tr} \tag{3.13}$$

where R'_s is the equivalent stator resistance and L'_s is the equivalent stator inductance.

The control of the actual motor through the transmission system can then be regarded as direct control of the equivalent motor. The implemented controllers compensate for the voltage drop in the transmission system, by considering the equivalent stator parameters R'_s and L'_s, an equivalent stator voltage $\bar{u}'_s$ and an equivalent stator flux linkage $\bar{\psi}'_s$, whenever needed.

Having integrated the transmission system parameters into the motor parameters, the actual voltage $\bar{u}_s$ of the PMSM can be calculated by subtracting the voltage drop in the transmission impedance from the equivalent voltage $\bar{u}'_s$, which is the voltage produced by the VSD. The voltage drop, in turn, can be easily obtained when the transmission parameters R_{tr} and L_{tr} and the stator current $\bar{i}_s$ are known.

The system should be designed in a proper way, so that a specified steady-state voltage drop occurs in the transmission system. In the actual application, where the transmission distance is fixed, this could be achieved by selecting an appropriate level for the operating voltage and a cable with suitable parameters.

In the performed simulations on the other hand, the voltage level and the transmission system parameters are considered to be fixed and the desired voltage drop is obtained by selecting the proper cable length.

3.3 Open-loop V/f control

This section discusses the basic idea of V/f control, explains the need for a low startup frequency and introduces a voltage-boosting factor for low-speed operation of the PMSM.

It also describes the implemented open-loop V/f regulator, which is deployed to accelerate the motor from standstill up to a certain speed level. The term 'open-loop' refers to the fact that no feedback is received by the controller and therefore no current or speed measurements are needed for its operation.

3.3.1 Basic idea of the V/f controller

The fundamental idea of V/f control can be demonstrated by considering (3.1) under the assumptions that the stator flux linkage is constant and that the resistive term is negligible. This gives

$$\bar{u}_s \simeq j\omega_r \bar{\psi}_s \Rightarrow \hat{\psi}_s \simeq \frac{\hat{u_s}}{\omega_r} \Rightarrow \hat{\psi}_s \simeq \frac{\hat{u_s}}{2\pi f} \tag{3.14}$$

where f is the electrical frequency and $\hat{\psi}_s$ and $\hat{u_s}$ are the magnitudes of the flux linkage vector and the voltage vector respectively, thus the amplitudes of the respective three-phase quantities.

Equation (3.14) shows that in order to keep the stator flux linkage approximately constant, the amplitude of the supplied stator voltage must be varied proportionally to the electrical frequency.

With the exception of field-weakening operation, it is generally desirable to maintain the value of the stator flux linkage around its nominal level, which is approximately equal to the rated voltage over the rated speed [20].

For high values of the V/f ratio, the motor becomes overexcited and a rise in the current i_{sd} occurs, according to (3.2). A low V/f ratio on the other hand, causes the motor to experience underexcitation, which is associated with a negative i_{sd}.

Both overexcited and underexcited states are accompanied by a rise in the stator current, as a result of the increased magnitude of its d-axis component. Since the current i_{sd} does not contribute to any torque production, according to (3.7), the increase of its magnitude is translated into a rise in power losses. Although this might be tolerated in the special case of field-weakening operation, it is in general clearly undesirable.

3.3.2 Necessity of low initial frequency

During the initial stage of its startup, the PMSM tries to establish synchronism with the supplied magnetic field. For high values of the applied frequency however, the rotor might be unable to follow the fast rotation of the field, leading to an unsuccessful startup with rotor vibrations.

In order to avoid scenarios of unsuccessful startup, it is necessary to supply the motor with low frequency in the beginning. Then, as the rotor accelerates, the supplied frequency can be gradually increased up to its steady-state value. In order to safeguard the stability of the system, the rate at which the frequency is increased should be kept adequately low [7].

According to the discussion in Section 3.3.1, in order to achieve approximately constant stator flux linkage and therefore avoid the undesirable states of overexcitation and underexcitation, the increasing frequency must be accompanied by an almost proportionally increasing voltage.

3.3.3 Voltage boosting at low speeds

According to (3.14), the applied V/f ratio must be approximately equal to the rated voltage over the rated speed of the motor.

However, it must be borne in mind that (3.14) was derived from (3.1) under the assumption that the resistive term of the equation is negligible. This assumption is not valid for very low speeds, when the speed-dependent term is comparable to the resistive voltage drop in the stator.

This issue is handled by using a voltage-boosting factor for electrical speeds below a low critical value $\omega_{r,cr}$. This factor, whose mission is to compensate for the resistive drop at low frequencies, is denoted as F_b and is defined as

$$F_b = \frac{\hat{i}_{s,rated} R'_s + \omega_{r,cr} \Psi_m}{\omega_{r,cr} \Psi_m} \tag{3.15}$$

where $\hat{i}_{s,rated}$ is the peak value of the rated stator current.

According to (3.3), the term $\omega_{r,cr} \Psi_m$ represents the back-EMF of the motor at $\omega_r = \omega_{r,cr}$. The numerator of (3.15), consisting of the back-EMF term and the resistive drop in the equivalent PMSM (calculated for the rated stator current), is a rough approximation of the needed voltage amplitude at $\omega_r = \omega_{r,cr}$.

When the electrical speed ω_r is below its critical value $\omega_{r,cr}$, the voltage-boosting factor F_b is included in the calculation of the stator voltage amplitude reference u_s^* according to

$$\hat{u}_s^* = \omega_r^* F_b \Psi_m \Rightarrow \hat{u}_s^* = 2\pi f^* F_b \Psi_m \tag{3.16}$$

where f^* is the frequency reference and ω_r^* is the corresponding electrical speed reference.

Clearly, this method of compensating for the resistive voltage drop at low speeds is approximate, mainly because the stator current used in (3.15) is considered to be constant and equal to $\hat{i}_{s,rated}$.

More accurate compensation can be achieved by measuring the actual stator currents and including them in the calculation of the stator voltage. Such an improved method is discussed in the section of the closed-loop V/f controller.

3.3.4 Simplifying assumption

For the sake of simplicity, it has been assumed during the design of the different models in this thesis that the voltage at the output of the VSD is sinusoidal and equal to the three-phase voltage reference produced by the implemented controllers.

In practice, the three-phase reference signal at the output of the controller enters a PWM stage, where it is compared with a carrier wave. The result of the comparison determines the form of the voltage pulses that are generated by the VSD.

In the designed models however, the PWM stage is not taken into account. Instead, a simplified interface between the control circuit and the power circuit is used to transform the voltage reference produced by the controller into a power-level voltage of the same form.

The aforementioned simplification can be justified by the following considerations.

By assuming that the voltage output of the VSD is properly filtered, according to the discussion in Section 2.2.2, the high-order harmonics of the PWM pulses produced by the inverter can be neglected and only the fundamental component of the VSD output can be taken into account during the design of the control models.

Since the form of the fundamental component for each phase is expected to match the form of the respective voltage reference provided by the controller [38], the latter one can be transformed into a power-level signal, which can be applied directly at the output of the VSD.

3.3.5 Implementation of the controller

The mission of the open-loop V/f controller is to supply the PMSM with a voltage of proper magnitude and frequency, so that successful acceleration from standstill up to a desired speed level is achieved.

Since no feedback is received by the controller in the open-loop scheme, the voltage output of the VSD is pre-determined and is not affected by the actual response of the PMSM.

As shown in Fig. 3.2, the calculation of the output voltage of the controller is a straightforward process, which consists of three steps.

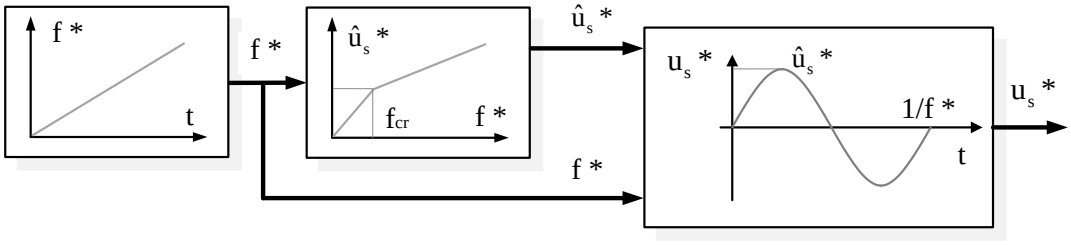

Figure 3.2: Block diagram of the open-loop V/f controller

The first step is the generation of a frequency reference ramp, the slope of which is determined by the desired acceleration of the PMSM, but also by the stability requirements of the system. It is important to ensure that the increase-rate of the frequency reference curve is not too high, otherwise the synchronism of the PMSM may be at risk.

The second step is the calculation of the voltage amplitude reference, according to predefined V/f ratios.

When the frequency reference f^* is below a critical value f_{cr} (corresponding to the critical electrical speed $\omega_{r,cr}$), voltage boosting is necessary and the voltage amplitude reference is calculated according to (3.16).

On the other hand, when the frequency reference has exceeded the critical value f_{cr}, the V/f controller calculates the voltage amplitude reference $\hat{u}_s^*$ from

$$\hat{u}_s^* = \frac{\hat{u'}_{s,rated} - \hat{u}^*_{s(f^*=f_{cr})}}{f_{rated} - f_{cr}} f^* \tag{3.17}$$

where $\hat{u'}_{s,rated}$ is the peak value of the equivalent rated stator voltage, f_{rated} is the rated frequency and $\hat{u}^*_{s(f^*=f_{cr})}$ is the voltage amplitude reference at the critical frequency (calculated from (3.16)). The value $\hat{u'}_{s,rated}$ represents the voltage output of the VSD which corresponds to the rated voltage $\hat{u}_{s,rated}$ of the PMSM, increased by the desired voltage drop in the transmission system.

The third step for the calculation of the output voltage of the controller is to insert the generated frequency reference and the calculated voltage amplitude reference into the sinusoidal equations that produce the three-phase voltage output of the controller. These equations are written as

$$\begin{aligned} u^*_{sa}(t) &= \hat{u}^*_s(t)\cos\theta^*_r(t) \\ u^*_{sb}(t) &= \hat{u}^*_s(t)\cos[\theta^*_r(t) - 120^o] \\ u^*_{sc}(t) &= \hat{u}^*_s(t)\cos[\theta^*_r(t) + 120^o] \end{aligned} \tag{3.18}$$

where u^*_{sa}, u^*_{sb} and u^*_{sc} are the reference voltages for the three phases and θ^*_r is the electrical angle reference, which is given by

$$\theta_r^*(t) = \int \omega_r^*(t)dt = \int 2\pi f^*(t)dt \tag{3.19}$$

The implemented open-loop V/f control scheme is based on (3.15) - (3.19). Its most important advantages are the simplicity of its control algorithm and the absence of feedback, which eliminates the need for current, speed and position sensors.

On the negative side, the control algorithm is based on rough approximations, which may have a negative effect on the performance of the controller.

3.4 Closed-loop V/f control

A second V/f control scheme has been implemented, based on a method presented in [23], and is discussed in this section. Unlike the open-loop method which was presented in Section 3.3, this scheme uses current feedback to determine the voltage reference with higher accuracy. A built-in stabilizer is included in the closed-loop controller, in order to ensure that the PMSM does not lose synchronism.

3.4.1 Voltage reference calculation

The calculation of the voltage reference of the closed-loop V/f controller is based on (3.1). Considering steady-state operation, the space vector $\bar{u'}_s$ of the equivalent stator voltage is given by

$$\bar{u'}_s = R'_s\bar{i}_s + j\omega_r\bar{\psi'}_s \tag{3.20}$$

where $\bar{\psi'}_s$ is the space vector of the equivalent stator flux linkage. The magnitude $\hat{u'}_s$ of the voltage vector can be obtained by algebraically adding the projections of the terms $R'_s\bar{i}$ and $j\omega_r\bar{\psi'}_s$ in the direction of $\bar{u'}_s$ [23]. This gives

$$\hat{u'}_s = R'_s\hat{i}_s\cos\phi_0 + \sqrt{(\omega_r\hat{\psi'}_s)^2 + (R'_s\hat{i}_s\cos\phi_0)^2 - (R'_s\hat{i}_s)^2} \tag{3.21}$$

where $\hat{i}_s$ is the peak value of the stator current and $\cos\phi_0$ is the power factor.

As was discussed in Section 3.1, the d-axis current i_{sd} usually has a more significant effect on the magnitude of the stator flux linkage than the q-axis current i_{sq}. By neglecting the q-axis current term in (3.2), it can be observed that when the d-axis current i_{sd} is set to zero, the magnitude $\hat{\psi'}_s$ of the equivalent stator flux linkage vector is equal to the flux linkage Ψ_m of the permanent magnets.

Since i_{sd} does not contribute to any torque production, the aforementioned condition yields the most efficient operating point of the PMSM, thus the point at which the torque-to-current ratio is maximum. Based on this statement, the stator flux linkage $\hat{\psi'}_s$ in (3.21) can be set equal to Ψ_m, so that approximately optimal efficiency is achieved. The voltage amplitude reference $\hat{u}_s^*$ can then be calculated from

$$\hat{u}_s^* = R'_s(\hat{i}_s\cos\phi_0) + \sqrt{(\omega_r^*\Psi_m)^2 + [R'_s(\hat{i}_s\cos\phi_0)]^2 - (R'_s\hat{i}_s)^2} \tag{3.22}$$

It should be borne in mind that the accuracy of (3.22) depends on the validity of the assumption that the effect of i_{sq} on the stator flux linkage is negligible. This assumption is weaker for motors with high q-axis inductance L_{sq} or high torque output (therefore high i_{sq} according to (3.7)).

Even though, according to the presented derivation, the current amplitude $\hat{i}_s$ and the power factor $\cos\phi_0$ in (3.22) are steady-state quantities, their instantaneous values can be considered during the calculation of the voltage amplitude reference $\hat{u}_s^*$ [23].

Assuming balanced operation of the system, these values can be obtained by performing current measurements in two of the three phases of the PMSM. The stator current magnitude $\hat{i}_s$ is then given by

$$\hat{i}_s = \sqrt{\frac{1}{3}(i_{sa} + 2i_{sb})^2 + i_{sa}^2} \tag{3.23}$$

where i_{sa} and i_{sb} are the measured phase currents. The term $\hat{i}_s \cos\phi_0$ is calculated as

$$\hat{i}_s \cos\phi_0 = \frac{2}{3}[i_{sa}\cos\theta_r^* + i_{sb}\cos(\theta_r^* - 120^o) - (i_{sa} + i_{sb})\cos(\theta_r^* + 120^o)] \tag{3.24}$$

where θ_r^* is the electrical angle reference, the calculation of which is discussed in Section 3.4.4.

3.4.2 Need for stabilization

A problematic issue that is commonly associated with V/f control schemes is their proneness to instability, thus the tendency of the controlled PMSMs to lose synchronism within specific speed ranges [24, 26].

The instability phenomena are accompanied by power and speed oscillations, which result in the inability of the motor to stay synchronized with the rotating magnetic field of its stator.

In order to safeguard the stability of the system, the settings and the parameters of the V/f controller must be selected carefully. For instance, it is important to choose a proper slope for the speed reference curve, since too high increase rates may prevent the PMSM from establishing synchronism.

Furthermore, the transitions between the different intervals of the speed reference curve should be as smooth as possible, since the existence of sharp edges might cause overcurrents and loss of synchronism [21].

However, even if the control parameters are selected properly, the performance of the system is still dependent on the motor parameters and on the load conditions [5].

For the closed-loop V/f control scheme which has been implemented in this thesis, it has been previously found that when a certain applied frequency is exceeded, the control

poles of the rotor pass into the instability region of the s-plane and synchronism is lost [23].

In order to improve the stability of the system, PMSMs are sometimes designed with damper windings in their rotor. However, since this solution increases the manufacturing costs and complicates the motor construction, a more convenient way to stabilize the motor is needed.

A more flexible solution is to add damping to the system, not by modifying its physical topology, but by including a stabilizing algorithm in the V/f controller.

3.4.3 Basic idea of the stabilizer

A stabilizing loop has been implemented according to [23] and has been included in the closed-loop V/f controller, in order to prevent the PMSM from losing synchronism. The mission of the stabilizing loop is to provide extra damping to the system, so that the control poles of the PMSM are kept in the stable region for the whole applied frequency range.

If a control scheme with speed sensors was considered, the stabilizing loop would counteract the perturbations in the measured speed, by modulating the applied frequency. By adjusting the electrical excitation of the motor according to the mechanical response of the PMSM, the stabilizer would contribute to the attenuation of the mechanical oscillations and would help the motor stay in synchronism.

Of course, since the implemented control scheme is position- and speed-sensorless, the operation of the stabilizing loop cannot depend on speed measurements.

However, based on the observed relation between the speed perturbations and the resulting power oscillations, the stabilizer can utilize the available current measurements, in order to calculate the power perturbations and modulate the applied frequency accordingly.

3.4.4 Implementation of the stabilizer

The operation of the implemented stabilizing loop relies on the approximately linear relation between the speed perturbations of the PMSM and the resulting power oscillations [23].

Using the term $\hat{i}_s \cos\phi_0$, which is calculated from (3.24), and the voltage amplitude reference $\hat{u}_s^*$, which is given by (3.22), the electric power p_e' of the equivalent motor can be obtained from

$$p_e' = \frac{3}{2}\hat{u}_s^*\hat{i}_s \cos\phi_0 \tag{3.25}$$

In order to extract the power perturbations $\Delta p_e'$ from the calculated power p_e', a high-pass filter is used. Based on the obtained value of $\Delta p_e'$, the stabilizer produces a frequency modulation signal $\Delta\omega_r^*$, which is obtained from

$$\Delta\omega_r^* = -k_l \Delta p_e' \tag{3.26}$$

where k_l is the speed-dependent gain of the stabilizer, given by

$$k_l = \frac{c_l}{\omega_r^*} \tag{3.27}$$

where c_l is a constant, which is determined by trial and error. The block diagram of the stabilizer is shown in Fig. 3.3.

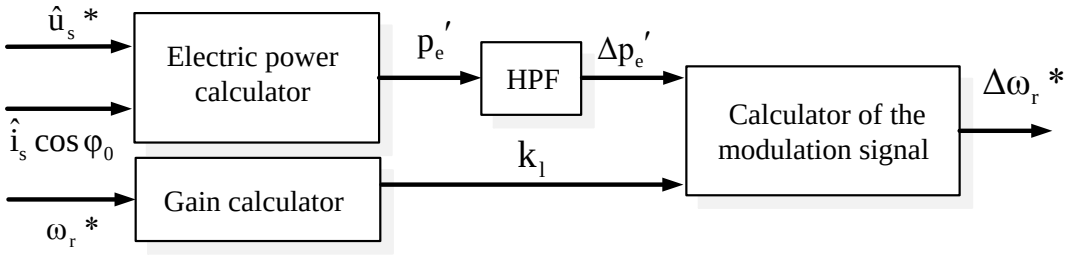

Figure 3.3: Block diagram of the stabilizer

During the early stages of the startup, thus when the PMSM operates at very low speeds, (3.27) gives a large value for the gain k_l, which might result in problematic operation of the stabilizing loop.

Considering that the implemented control method experiences stability issues only when a certain frequency is exceeded (as mentioned in Section 3.4.2), the stabilizer can be disabled at very low speeds, without any risks for the synchronism of the PMSM.

The frequency modulation signal $\Delta\omega_r^*$, which is calculated from (3.26), is included in the calculation of the electrical angle reference θ_r^* according to

$$\theta_r^*(t) = \int [\omega_r^*(t) + \Delta\omega_r^*(t)]dt = \int [2\pi f^*(t) + \Delta\omega_r^*(t)]dt \tag{3.28}$$

To summarize, the stabilizer detects possible oscillations in the electric power of the system and modulates the frequency reference f^* (or, equivalently, the electrical angle reference θ_r^*) of the controller, by producing a signal which opposes the detected oscillations.

3.4.5 Structure of the controller

Compared to the structure of the open-loop controller, which was described in 3.3.5, the implementation of the closed-loop V/f control scheme is significantly more complex, as can be observed in Fig. 3.4.

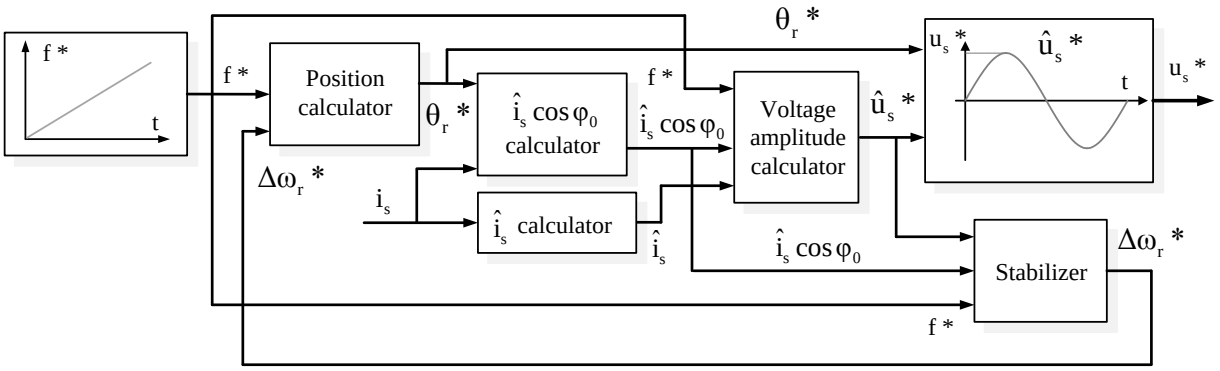

Figure 3.4: Block diagram of the closed-loop V/f controller

Its operation relies on stator current measurements and includes an increased amount of calculations, the aim of which is to produce an accurate voltage reference and to safeguard the stability of the system.

Similarly to the open-loop scheme, a frequency reference ramp is initially generated by the controller. In order to eliminate sharp edges from the transition intervals of the ramp, a low-pass filter is used to smoothen the curve. According to the discussion in Section 3.4.2, the generation of a smooth frequency reference $f^*(t)$ is expected to have a positive effect on the performance of the controller.

Based on the generated frequency signal f^*, the electrical angle reference θ_r^* is obtained. Together with the measured stator currents i_{sa} and i_{sb}, the angle θ_r^* is used to calculate the current terms $\hat{i}_s$ and $\hat{i}_s \cos\phi_0$ from (3.23) and (3.24) respectively. In order to eliminate the high-frequency ripple in $\hat{i}_s$ and $\hat{i}_s \cos\phi_0$, two low-pass filters are needed.

Next, the current terms are used for the determination of the voltage amplitude reference $\hat{u}_s^*$ from (3.22). A voltage limiter has been included in the controller, in order to ensure that the calculated value of the voltage amplitude reference is within acceptable limits.

Eventually, the electrical angle reference θ_r^* and the voltage amplitude reference $\hat{u}_s^*$ are inserted into (3.18), so that the three-phase voltage reference of the controller is obtained.

By using the generated frequency reference f^*, the calculated term $\hat{i}_s \cos\phi_0$ and the produced voltage amplitude reference $\hat{u}_s^*$, the stabilizer generates a frequency modulation signal $\Delta\omega_r^*$ from (3.26). This signal is added on top of the generated speed reference when calculating the angle θ_r^* according to (3.28). A stabilizing loop is therefore formed, the mission of which is to protect the PMSM from losing synchronism.

3.4.6 Comments on the controller

Despite its increased complexity, the designed closed-loop V/f controller is expected to provide higher control precision, compared to the open-loop scheme. The need for current measurements is not a problem, since the availability of current sensors is necessary for the vector controller anyway.

Having the measured stator currents at its disposal, the controller is capable of taking the resistive voltage drop of the PMSM stator into account, when calculating the voltage reference. This eliminates the need for a voltage-boosting factor for the initial stage of the PMSM startup, in other words, voltage boosting is inherent in the closed-loop control method.

In contrast to the open-loop scheme, where the frequency reference is fixed and independent of the motor response, the closed-loop V/f controller can indirectly detect speed oscillations and modify its frequency reference, so that the PMSM does not lose synchronism. This is expected to result in higher reliability and lower sensitivity to load changes.

On the negative side, the voltage reference calculation in the closed-loop V/f controller is based on equation (3.22), which has been derived for steady-state operation. Considering that the V/f control method is deployed during the startup of the PMSM, this assumption could slightly affect the performance of the controller.

3.5 Vector control with position sensor

Although the presence of position or speed sensors is undesirable for the studied application, a vector control scheme with such sensors has been implemented, as an intermediate step towards the development of a position-sensorless method. The design of this scheme is discussed in this section.

3.5.1 Structure of the controller

The structure of the implemented vector controller is presented in Fig. 3.5.

The currents of the system are measured and are transformed into the dq reference frame. The rotor position, which is necessary for the dq transformation of the currents, is measured with a mechanical sensor.

The vector controller receives an external torque command and calculates the current

references in the dq reference frame. The calculated references, together with the transformed stator currents, enter the current controller.

The knowledge of the rotor speed is necessary for the operation of the current controller. The speed is assumed to be measured directly from the shaft of the PMSM, although it can also be calculated as the derivative of the measured rotor position.

The current controller produces a reference voltage in the dq reference frame. By using the measured rotor position, this voltage is transformed into the three-phase system and is used to determine the output of the VSD.

In the actual application, the three reference voltage waveforms, which are generated by the controller, enter a PWM stage, where they are compared with a carrier wave. The result of the comparison determines the state of the switches of the inverter and, therefore, the form of the voltage pulses at the output of the VSD.

However, as in the case of the V/f control models, the PWM stage is omitted and the reference voltage generated by the vector controller is assumed to be equal to the voltage output of the drive. Therefore, it is assumed that the VSD produces sinusoidal voltage waveforms, instead of PWM pulses.

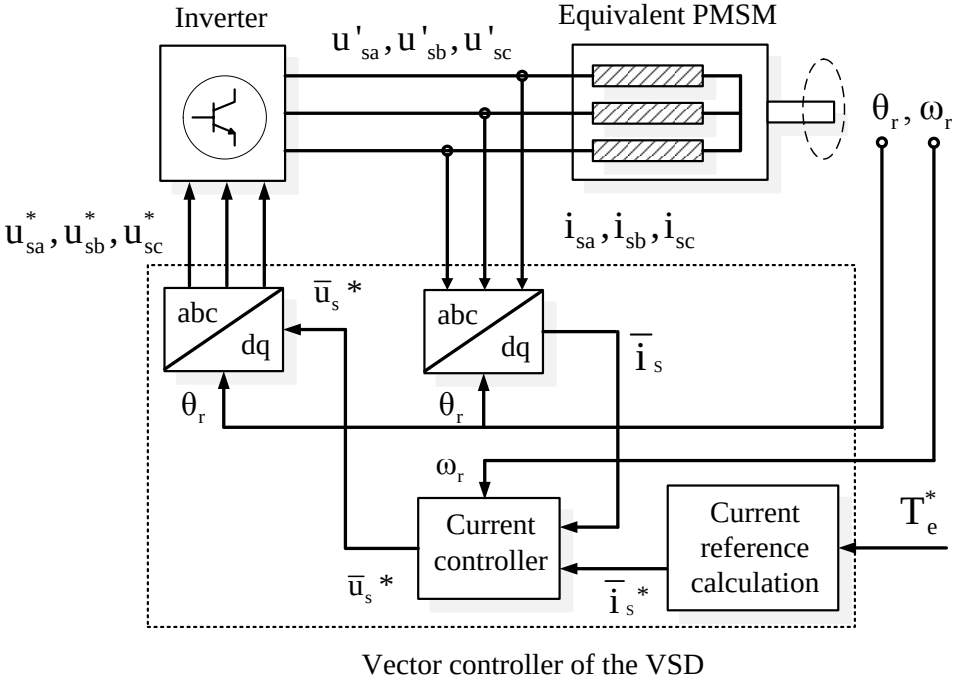

Figure 3.5: Vector control topology, including mechanical sensors.

3.5.2 Need for constant torque reference

The PMSM in the studied application needs to operate under constant-torque control.

The multiphase pump accommodates fluid stream of varying composition. This stream consists of oil, gas and water, the analogy of which changes with time. Due to the varying mass density of the stream mixture, the load of the PMSM also changes with time.

By applying a constant torque reference in the vector controller, the speed of the motor-pump assembly can be regulated rapidly in response to load variations. This behaviour corresponds to the desired operation of the system.

3.5.3 Current reference calculation

As was discussed in Section 3.1.1, the only torque-producing current component in PMSMs with surface-mounted magnets is the q-axis current. The reference i_{sq}^* for this component can be calculated from (3.7) as

$$i_{sq}^* = \frac{2}{3n_p\Psi_m}T_e^* \tag{3.29}$$

where T_e^* is the electromagnetic torque reference. Regarding the reference i_{sd}^* of the d-axis stator current, it is usually selected in such a way, that the efficiency of the PMSM is maximized. In general, its optimal value can be obtained by the MTPA method [34, 36] according to

$$i_{sd}^* = \frac{\Psi_m - \sqrt{\Psi_m^2 + 8(L_{sq} - L_{sd})^2(\hat{i}_s^*)^2}}{4(L_{sq} - L_{sd})} \tag{3.30}$$

where $\hat{i}_s^*$ is the reference of the stator current amplitude. In PMSMs with surface-mounted magnets, the d-axis current does not contribute to any torque production and the maximum torque-to-current ratio is obtained by simply setting $i_{sd}^* = 0$ [30, 39].

Since no dq saliency is considered for the PMSM in this thesis, the d-axis current reference is set to zero for speeds lower than the rated speed $\omega_{r,rated}$. However, when operation above $\omega_{r,rated}$ is desired, the reference i_{sd}^* needs to be modified by applying a proper field-weakening strategy. Such a strategy is discussed in the section of the position-sensorless vector controller.

3.5.4 Transfer function of the controlled system

Before the vector controller can be designed, the transfer function of the controlled system must be derived. This system includes the PMSM and the transmission components, namely the cable and the two transformers.

For PMSMs with surface-mounted magnets, the d-axis and q-axis inductances are approximately equal. Considering equivalent motor quantities, the flux-linkage equation (3.2) can then be written as

$$\bar{\psi}'_s = L'_s \bar{i}_s + \Psi_m \tag{3.31}$$

By substituting (3.31) into (3.1), the equivalent stator voltage $\bar{u}'_s$ is given by

$$\bar{u}'_s = R'_s \bar{i}_s + L'_s \frac{d\bar{i}_s}{dt} + j\omega_r L'_s \bar{i}_s + j\omega_r \Psi_m \tag{3.32}$$

where the term $j\omega_r \Psi_m$ is the back-EMF $\bar{e}$ of the PMSM (according to (3.3)) and $j\omega_r L'_s \bar{i}_s$ is the cross-coupling term.

The cross-coupling effect, thus the inherent interaction between the d-axis and q-axis quantities of the PMSM, prevents the independent control of i_{sd} and i_{sq}, as can be demonstrated through the d-axis and q-axis voltage equations of the motor.

According to (3.4), a variation in u_{sd} results in a desirable change in i_{sd}. However, due to the d-axis component of the cross-coupling term in (3.5), the voltage u_{sq} is also forced to change, which in turn causes an undesirable variation in i_{sq}. In effect, a change in i_{sd} is inevitably accompanied by a change in i_{sq} and vice versa.

By applying the Laplace transform and rearranging terms, (3.32) becomes

$$\bar{i}_s = \frac{1}{sL'_s + R'_s + j\omega_r L'_s} (\bar{u}'_s - \bar{e}) \tag{3.33}$$

Equation (3.33) represents the transfer function of the physical system that consists of the PMSM and the transmission components.

3.5.5 Inclusion of compensating terms

In order to improve the performance of the current regulation, it is necessary to modify the transfer function of the physical system (obtained from (3.33)) by including certain

compensating terms in the vector controller [35].

As was demonstrated in Section 3.5.4, the inherent cross-coupling in the PMSM prevents the independent regulation of the d-axis and q-axis currents, thus the separate control of the flux and the torque of the motor.

The negative impact of the cross-coupling effect on the performance of the controller can be mitigated by compensating for the term $j\omega_r L'_s \bar{i}_s$ in (3.32). Clearly, the compensation demands the knowledge of the stator current and the motor speed and its precision depends on the accuracy of the estimation of the equivalent stator inductance L'_s.

The control performance can be further improved by cancelling out the effect of the back-EMF of the PMSM, thus by compensating for the term $j\omega_r \Psi_m$ in (3.32). By feeding-forward this term in the vector controller, the interaction between the electrical and the mechanical dynamics of the motor is eliminated.

Finally, the term $R_a \bar{i}_s$ can be added on the right-hand side of (3.32). The value R_a is called active-damping resistance and is used to effectively increase the resistance R'_s of the system. Its presence in the controller increases the damping of the system and therefore improves its response to disturbances. Of course, since R_a is a control parameter and not a physical resistance, it does not contribute to any losses.

The block diagram of the physical system with the added compensating terms is shown in Fig. 3.6.

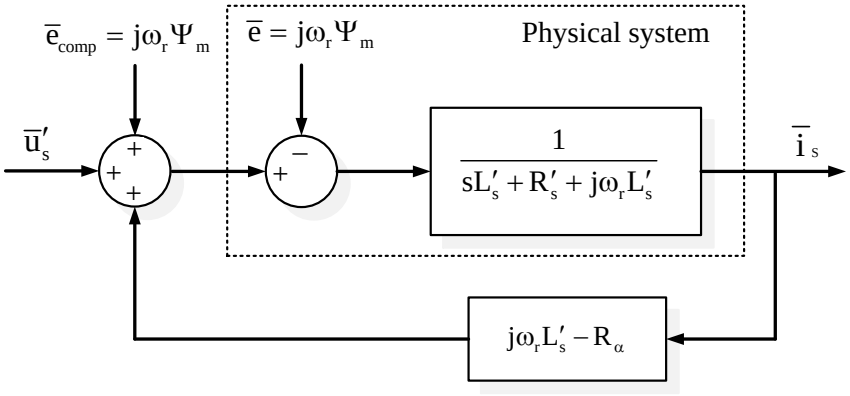

Figure 3.6: Block diagram of the physical system with the added compensating terms.

After cancelling out the back-EMF and the cross-coupling term of the PMSM and after

introducing the active-damping resistance in the vector controller, (3.33) becomes

$$\bar{i}_s = \frac{\bar{u'}_s}{sL'_s + R'_s + R_a} \tag{3.34}$$

Equation (3.34) represents the modified transfer function of the system, thus the transfer function that is considered for the design of the controller.

3.5.6 Design of the PI regulator

The use of the dq reference frame, which results in the transformation of steady-state AC quantities into DC values, makes it possible to use PI regulators for current control. The reason is that integrators are well-suited for the control of DC quantities, because they provide infinite gain at zero frequency and can therefore ensure the absence of steady-state errors.

The relation between the input $(\bar{i}^*_s - \bar{i}_s)$ and the output $\bar{u}^*_s$ of the PI current regulator is given by

$$\bar{u}^*_s = (k_p + \frac{k_i}{s})(\bar{i}^*_s - \bar{i}_s) \tag{3.35}$$

where k_p is the proportional gain, k_i is the integral gain and $\bar{i}^*_s$ is the space vector of the stator current reference. The mission of the PI regulator is to provide current control to the modified system, which was shown in Fig. 3.6. The current-controlled system is presented in Fig. 3.7.

The PI regulator is designed according to the IMC method [35]. The closed-loop system, which consists of the modified transfer function of the controlled system (given by (3.34)), the transfer function of the PI regulator (given by (3.35)) and unit feedback, is designed to be a first-order system with bandwidth a_c. The gains of the PI regulator can then be readily obtained as

$$k_p = a_c L'_s \tag{3.36}$$

$$k_i = a_c(R'_s + R_a) \tag{3.37}$$

where the active-damping resistance R_a can be calculated from

$$R_a = a_c L'_s - R'_s \tag{3.38}$$

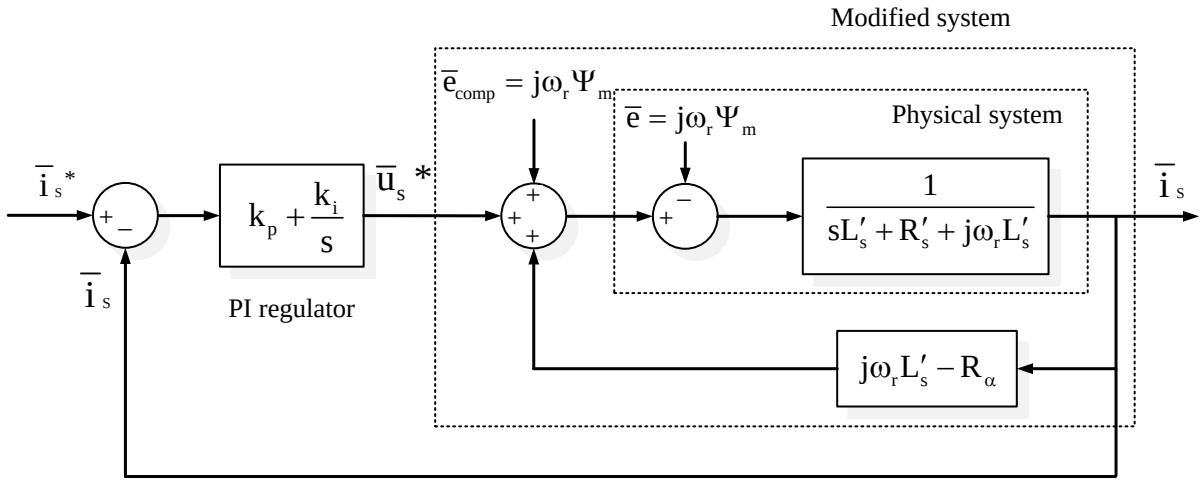

Figure 3.7: Block diagram of the current-controlled system, consisting of the physical system, the compensating terms and the PI regulator.

The bandwidth a_c of the current regulator corresponds to a frequency which is selected to be several times lower than the switching frequency of the VSD. The value of a_c determines the response speed of the controller according to

$$t_r = \frac{ln9}{a_c} \tag{3.39}$$

where t_r is the rise time, thus the time needed by the controlled currents to change from 10% to 90% of their final value.

3.5.7 Implementation of voltage and current limiters

The design of the vector controller must ensure that the electrical limits of the PMSM and the VSD are not exceeded [31]. The value of the stator current reference must not be greater than the rated current of the PMSM, while the the commanded voltage must not exceed the maximum voltage capability of the VSD.

The limits of the current references i^*_{sd} and i^*_{sq} can be expessed as

$$i^*_{sd} \leq i_{s,max} \tag{3.40}$$

$$i^*_{sq} \leq \sqrt{(i_{s,max})^2 - (i^*_{sd})^2} \tag{3.41}$$

where $i_{s,max}$ is the maximum acceptable stator current, which is equal to the peak value of the rated current of the PMSM, thus $i_{s,max} = \hat{i}_{s,rated}$. The limit of the voltage amplitude reference $\hat{u}^*_s$ can be written as

$$\hat{u}_s^* \leq u_{s,max} \tag{3.42}$$

where $u_{s,max}$ is the maximum acceptable voltage at the output of the VSD.

The purpose of the implemented voltage and current limiters is to protect the PMSM and the VSD. However, it should be noted that when the current or voltage limits are hit, the intervention of the limiters causes the system to enter a practically uncontrolled state, which includes distorted current responses and higher rise times.

One particular issue concerning the voltage limiter is integrator windup. When the voltage limit is hit, the current error $(\bar{i}_s^* - \bar{i}_s)$ becomes high, since the controller is not allowed to provide the voltage that is required to achieve $\bar{i}_s^* = \bar{i}_s$. Integrating this error would result in a large ouput for the integrator, which should be decreased later, causing a substantial current overshoot [26].

In order to prevent integrator windup, an anti-windup function is implemented in the controller. Its idea is to cancel out the current error that results from the difference between the unlimited voltage $\bar{u}_s^*$ and the limited voltage $\bar{u}_{s,lim}^*$. The output of the anti-windup function is given by

$$\bar{i}_{aw} = \frac{1}{k_p}(\bar{u}_{s,lim}^* - \bar{u}_s^*) \tag{3.43}$$

where $\bar{i}_{aw}$ represents the error term due to the action of the voltage limiter. This term is added to the current error $(\bar{i}_s^* - \bar{i}_s)$ which enters the integrator. The complete current-controlled system, with the current limiters and the anti-windup function included, is presented in Fig. 3.8.

3.6 Position-sensorless vector control

The operation of the vector control scheme which was described in Section 3.5 is based on the presence of mechanical sensors.

This section explains why mechanical sensors need to be eliminated and describes different position-estimating methods which can facilitate sensorless operation of the PMSM. Based on one of these methods, a position-estimating algorithm has been implemented and is presented.

In order to extend the speed range of the PMSM, the option of applying a field-weakening

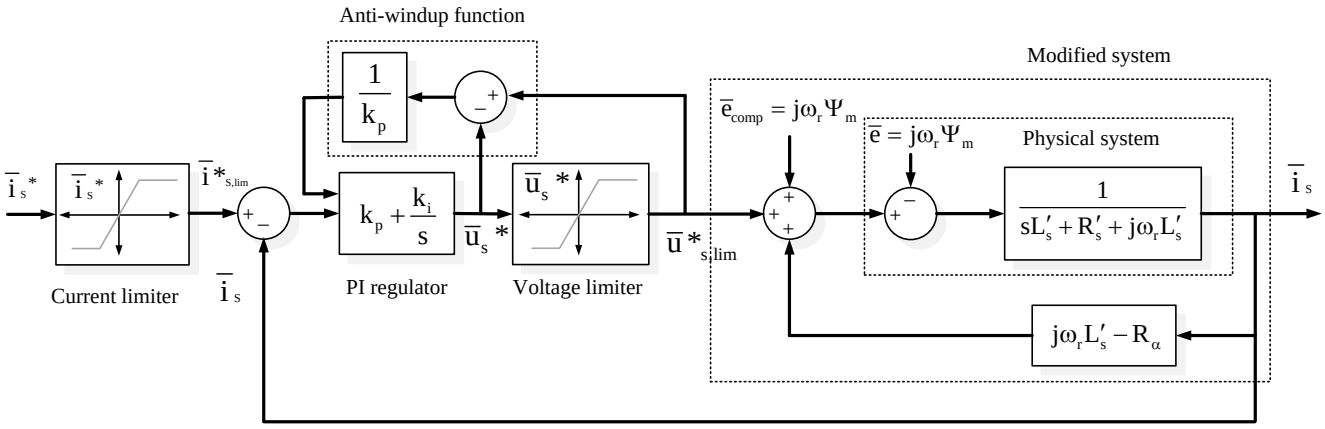

Figure 3.8: Block diagram of the current-controlled system, consisting of the modified system, the PI regulator, the current and voltage limiters and the anti-windup function.

strategy is investigated for the position-sensorless vector controller. After evaluating the suitability of the studied system for the application of such a strategy, a field-weakening algorithm is derived and is integrated into the vector controller.

Apart from the position estimator and the field-weakening algorithm, the other parts of the controller are the same as the ones presented in Section 3.5.

3.6.1 Necessity of eliminating the position sensor

The presence of position sensors in PMSMs is usually undesirable, since it increases the cost and the complexity of the system. When it comes to harsh subsea environments, it is particularly important for the system to be as simple and robust as possible. The use of position-sensorless control schemes is therefore a necessity.

The drawbacks of position sensors include an increased number of connections between the motor and the control system, increased electromagnetic interference due to the presence of connecting leads and limited measuring accuracy due to environmental factors, such as temperature, humidity and vibrations [25].

Moreover, the cost of the position-encoding device increases the overall cost of the system, while the static and dynamic friction of the sensors are added on top of the mechanical load of the motor [25, 27].

3.6.2 Review of position estimation methods

The operation of sensorless vector control schemes is facilitated by the development of techniques that estimate the rotor position θ_r. Different methods have been proposed for this purpose, some of which are shortly discussed in the section.

Back-EMF-based methods

By measuring the stator currents and voltages of the motor, the space vector of the back-EMF in the $\alpha\beta$ reference frame can be calculated. The obtained back-EMF vector can then be used to determine the rotor position.

Back-EMF-based methods cannot be used at a standstill or during low-speed operation of the PMSM, mainly because the back-EMF becomes too low in this range of speeds [27].

Furthermore, in order to calculate the back-EMF of the PMSM, the derivative of the measured stator current is used, which makes these methods prone to noise [28].

The accuracy of the estimation is also affected by errors in the values of the motor parameters [26].

Flux linkage-based methods

If the stator currents and voltages are known, the stator flux linkage in the $\alpha\beta$ reference frame can be calculated and used for the determination of the rotor position.

Due to the integration process by which the flux linkage is obtained, flux linkage-based methods often suffer from the effects of integrator drift, which are compensated by analog electronics or software techniques [28].

The accuracy of the position estimation is also affected by motor parameter variations [25].

Inductance-based methods

Inductance-based techniques can be used to estimate the rotor position in PMSM topologies in which the stator inductances vary significantly over an electrical cycle [28].

The estimation in this case can be based on look-up tables, which contain information about the relation between the stator inductances and the rotor position [26].

Problems with these methods may include the requirement of high switching frequency for the accurate calculation of the inductances, as well as sensitivity to certain parameter variations [26].

Observer-based methods

In observer-based techniques, a mathematical model of the system is created and is supplied with the same excitation as the actual system. This model produces estimated outputs, which are compared with the measured outputs of the real system. The errors between the estimated and the measured quantities are used to correct the outputs of the observer [27].

Since the PMSM model is nonlinear, the design of a state observer is generally quite complex. The used algorithms may often be robust against parameter variations and measurement noise, but they have high computational requirements [26].

Selection of estimation method

The estimation scheme which has been implemented in this thesis is flux linkage-based. It uses a thoroughly tested algorithm, which provides accurate position estimation within a wide speed range.

The issue of integrator drift, which is often considered to be the main drawback of flux linkage-based methods, is resolved by constantly correcting and updating the estimated quantities, by using the available current measurements.

Other methods could also provide adequate control performance for the studied application. Back-EMF-based methods, for instance, have proved to be quite popular and would probably be suitable for the studied system. Their inability to provide accurate position estimation at low speeds would not be a problem, since low-speed operation is handled by the V/f controller anyway.

Inductance-based methods however, would not be a sensible choice, since they are only well-suited to motors with significant inductance variations over one electrical period. As the considered motor has negligible dq saliency, the resulting variations would be too low to produce a proper position estimation.

3.6.3 Structure of the controller

The structure of the designed position-sensorless vector controller is presented in Fig. 3.9. In contrast to the layout presented in Fig. 3.5, no mechanical sensors are present in the new topology. Although this increases the robustness of the system, it also complicates the design of the vector controller.

The elimination of the mechanical sensors has been achieved by adding a position estimator in the controller. The mission of the estimator is to provide position estimates to the dq transformation blocks and speed estimates to the current controller. The inputs required by the estimator are two phase currents and a previously generated voltage reference.

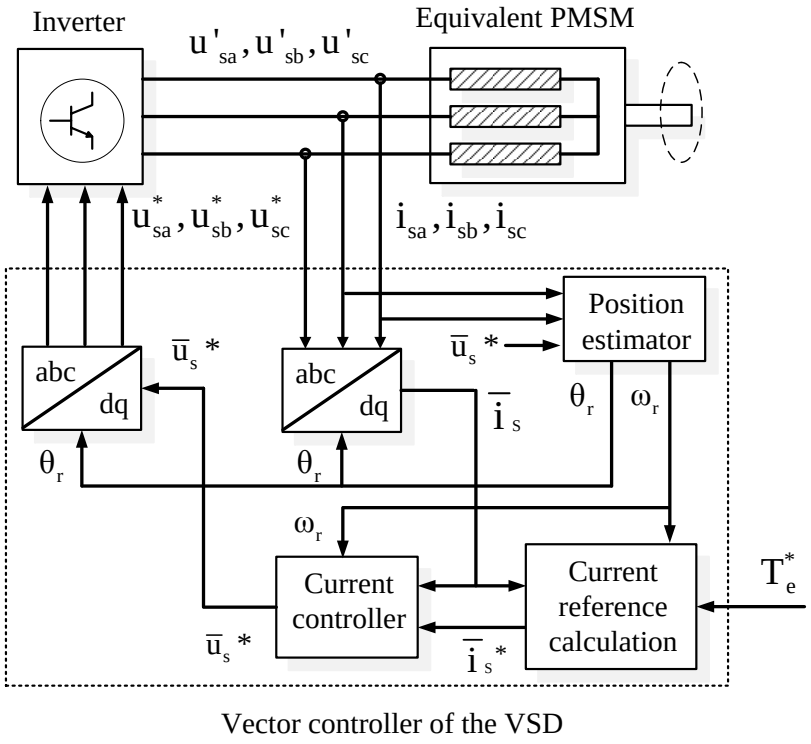

Figure 3.9: Position-sensorless vector control topology.

3.6.4 Implementation of the position estimator

The implemented estimator estimates the rotor position θ_r, by executing a multi-step discretized algorithm. Its operation is based on a method described in [26], although variations of this method have been earlier presented in [25, 28, 29].

For the design of the position estimator, it is convenient to use the $\alpha\beta$ reference frame. In

contrast to the dq frame, which is synchronized to the rotation of the PMSM rotor, the $\alpha\beta$ frame is stationary and its α axis is aligned with the a axis of the three-phase system [35].

Figure 3.10 provides an overview of the functions executed by the position estimator. The steps of the discretized estimating algorithm are discussed in more detail below.

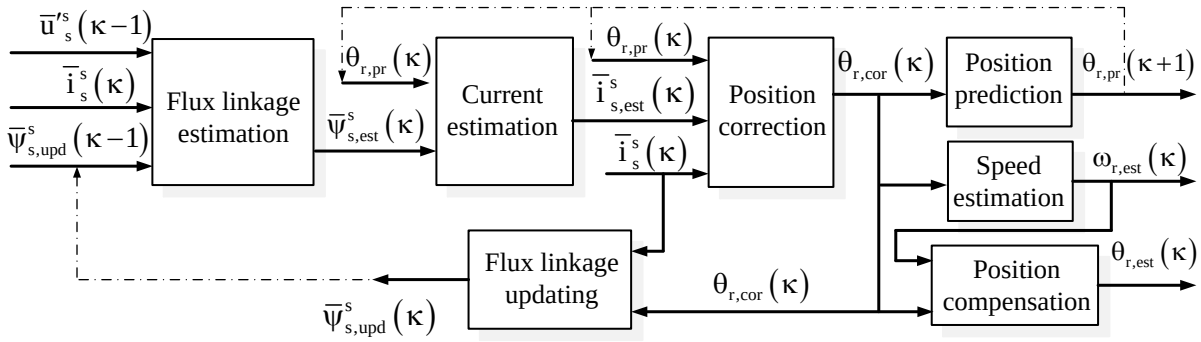

Figure 3.10: Block diagram of the position estimator.

Flux linkage estimation

The first step of the algorithm is the estimation of the equivalent stator flux linkage. By considering equivalent motor quantities, (3.1) can be represented in the $\alpha\beta$ frame as

$$\bar{u'}^{s}_{s} = R_s \bar{i}^{s}_{s} + \frac{d\bar{\psi}'^{s}_{s}}{dt} \tag{3.44}$$

The representation of the $\alpha\beta$ vectors is similar to the one of the dq vectors. The only difference is the additional superscript 's', which denotes that $\alpha\beta$ vectors are stationary. By using discretized quantities and integrating, (3.44) can be written as

$$\bar{\psi}'^{s}_{s,est}(\kappa) = T_s[\bar{u}'^{s}_{s}(\kappa-1) - R'_s \bar{i}^{s}_{s}(\kappa)] + \bar{\psi}'^{s}_{s,upd}(\kappa-1) \tag{3.45}$$

where T_s is the sampling period, κ is the sampling number and the subscripts '*est*' and '*upd*' denote estimated and updated values respectively. For the discrete integration of the difference between the stator voltage and the resistive drop, the rectangular rule has been applied.

Equation (3.45) estimates the equivalent stator flux linkage, based on the generated voltage reference and the updated flux linkage of the previous sampling period $\kappa-1$, as well as on the stator current, which is measured in the current period κ.

The flux linkage and stator voltage values of the previous sampling period are obtained

by including unit delay blocks in the controller. By storing signals for a specified amount of sampling periods, these blocks allow the controller to access previous values of its variables.

Current estimation

The second step of the algorithm is the estimation of the stator current, based on the estimated flux linkage $\bar{\psi}'^{s}_{s,est}$. Equation (3.31) can be represented in the $\alpha\beta$ frame as

$$\bar{\psi}'^{s}_{s} = L'_s \bar{i}^{s}_{s} + \Psi_m e^{j\theta_r} \tag{3.46}$$

The stator current can be estimated from

$$\bar{i}^{s}_{s,est}(\kappa) = \frac{\bar{\psi}'^{s}_{s,est}(\kappa) - \Psi_m e^{j\theta_{r,pr}(\kappa)}}{L'_s} \tag{3.47}$$

where the subscript '*pr*' denotes predicted quantities. Equation (3.47) estimates the stator currents by using the flux linkage obtained from the previous step and the position predicted for the current sampling period.

Position correction and speed estimation

The third step of the algorithm is the correction of the previously predicted rotor position. The current error, thus the difference $\Delta\bar{i}^{s}_{s}$ between the measured and the estimated currents, is calculated and is transformed into the dq reference frame by using the predicted rotor angle $\theta_{r,pr}$.

The presence of a current error indicates the need for position correction. It can be proven, as in [26], that only the q-axis component Δi_q of the dq-transformed current error $\Delta\bar{i}_s$ is needed for the calculation of the position correction term $\Delta\theta_r$ according to

$$\Delta\theta_r(\kappa) = -\frac{L'_s \Delta i_q(\kappa)}{\Psi_m} \tag{3.48}$$

The corrected position is then obtained from the predicted position $\theta_{r,pr}$ and the correction term $\Delta\theta_r$ according to

$$\theta_{r,cor}(\kappa) = \theta_{r,pr}(\kappa) + \Delta\theta_r(\kappa) \tag{3.49}$$

where the subscript '*cor*' denotes corrected values. The estimated speed $\omega_{r,est}$ of the PMSM is easily obtained from the discrete derivative of the corrected position according to

$$\omega_{r,est}(\kappa) = \frac{\theta_{r,cor}(\kappa) - \theta_{r,cor}(\kappa - 1)}{T_s} \tag{3.50}$$

The estimated speed passes through a low-pass filter, which eliminates the high-frequency ripple that might be present, and is then directed to the current regulator of the vector controller.

Flux linkage updating

The next step is to update the previously estimated flux linkage, so that the updated value $\bar{\psi}'^{s}_{s,upd}$ can be used for the flux linkage estimation in the next sampling period.

Equation (3.46) was used earlier to estimate the stator currents from the estimated flux linkage and the predicted position. By applying the same equation, this time using the measured currents and the corrected position, the updated flux linkage can be obtained as

$$\bar{\psi}'^{s}_{s,upd}(\kappa) = L'_s \bar{i}^{s}_{s}(\kappa) + \Psi_m e^{j\theta_{r,cor}(\kappa)} \tag{3.51}$$

By using the updated flux linkage $\bar{\psi}'^{s}_{s,upd}$ in the next sampling period, the negative effects of integrator drift are avoided.

Position prediction

The next step of the algorithm is the prediction of the rotor position for the next sampling period. A common assumption is that the position varies with time as a second-order polynomial [25, 28]. The predicted position $\theta_{r,pr}$ can be calculated from

$$\theta_{r,pr}(\kappa + 1) = 3\theta_{r,cor}(\kappa) - 3\theta_{r,cor}(\kappa - 1) + \theta_{r,cor}(\kappa - 2) \tag{3.52}$$

where the previously estimated positions $\theta_{r,cor}(\kappa - 1)$ and $\theta_{r,cor}(\kappa - 2)$ are obtained by using a single-period unit delay and a double-period unit delay respectively.

Position compensation

Tests on the implemented model revealed the presence of steady-state differences between the estimated currents and the real currents of the system. Furthermore, it was noticed that the magnitude of the estimation errors increased as the steady-state speed of the PMSM increased.

In order to eliminate these estimation errors, a speed-dependent position compensator

has been included in the estimator. Its mission is to generate a compensating term $\theta_{r,comp}$, which increases linearly with the estimated motor speed $\omega_{r,est}$ and which is added to the corrected position $\theta_{r,cor}$.

In order to determine the linear function $\theta_{r,comp} = f(\omega_{r,est})$ of the compensating block, the required compensation $\theta_{r,comp}$ for two different speeds is obtained by trial and error. The straight line which passes from the two position-speed pairs corresponds to the transfer function of the position compensator.

3.6.5 Basic idea of field-weakening

A field-weakening strategy has been applied in the sensorless vector controller, in order to extend the operating speed range of the PMSM. Before the implemented algorithm is presented, the fundamental principles of field-weakening are briefly discussed.

Assuming that the stator flux linkage of the PMSM is constant and that the resistive stator voltage drop is negligible, the stator voltage equation is given by (3.14). By solving for the electrical speed ω_r, this equation yields

$$\omega_r \simeq \frac{\hat{u}_s}{\hat{\psi}_s} \tag{3.53}$$

Equation (3.53) demonstrates that the speed of the motor can be increased either by increasing the supplied voltage amplitude, or by decreasing the stator flux linkage.

When the PMSM operates below its rated speed, the flux linkage should be kept around its nominal value, so that optimal efficiency is achieved, according to the discussion in Section 3.3.1. The speed in this case can be adjusted by varying the supplied voltage amplitude.

Speed control through the voltage amplitude is possible up to the rated speed of the motor. In order to increase the speed even further, without exceeding the rated voltage of the PMSM, it is necessary to decrease the amplitude of the stator flux linkage. Therefore, for high-speed operation of the motor, field-weakening is needed.

According to (3.2), a reduction of the flux linkage amplitude can be achieved by injecting a negative d-axis current into the motor. Since the d-axis current does not contribute to any torque production, field-weakening results in a decreased torque-to-current ratio.

Moreover, since the overall stator current cannot exceed its rated value, an increase of

the d-axis current restricts the maximum acceptable q-axis current and therefore the maximum torque that the PMSM can produce.

Based on the previous discussion, two control regions can be identified for the PMSM. The 'voltage control' region corresponds to constant maximum torque and power which increases with speed, while the 'flux control' region corresponds to constant power and maximum torque which decreases with speed [32, 40].

3.6.6 Overvoltage risk during field-weakening

When it comes to field-weakening, an issue that needs special attention is the risk of exceeding the voltage withstand limits of the VSD [36].

According to (3.3), the magnitude of the back-EMF is proportional to the speed of the motor. Therefore, the high speeds which are reached during the field-weakening operation result in high back-EMF values.

If the stator current is suddenly lost for some reason, the voltage drop in the transmission system and the stator impedance becomes zero and the inverter of the VSD experiences a voltage equal to the back-EMF of the PMSM.

In order to avoid damaging the inverter, it is necessary to design the VSD so that it can withstand the maximum back-EMF that can be reached during field-weakening [33].

For a VSD with a specified voltage output capability, it is necessary to limit the maximum speed during the field-weakening operation, so that the resulting back-EMF does not exceed the maximum voltage of the inverter [34].

3.6.7 Field-weakening capability of the system

Some systems provide favourable conditions for field-weakening operation, while others do not. This section evaluates the possibility of applying a field-weakening strategy in the studied system. The evaluation is based on considerations on the mechanical load and the system inductances.

In order to increase the motor speed above its rated value, a negative d-axis current is required, as was discussed in Section 3.6.5. Since the speed increase cannot be achieved without a torque increase for the considered load, the q-axis current needs to be increased as well.

Therefore, a speed increase with field-weakening requires a rise in the magnitude of both d-axis and q-axis currents and, as a result, an increase of the overall current magnitude.

Therefore, the degree to which the speed range of the PMSM can be extended by means of field-weakening depends on how soon the current limit of the motor is reached after exceeding the rated speed.

The available current margin depends on how high the load torque is. In the case of a light load, the stator current at rated speed is low and the current margin is high.

As explained in Section 3.6.5, the maximum torque that can be produced in the field-weakening region decreases as the speed increases. On the other hand, the actual produced torque increases with speed, due to the considered load characteristic.

The point at which the maximum and the actual torque become equal defines the maximum speed that can be reached with field-weakening. This is also the point at which the stator current reaches its rated value.

The field-weakening capability of the system is heavily dependent on the d-axis inductance of the PMSM. It can be observed from (3.2) that for low values of this inductance, the contribution of the d-axis current on the stator flux linkage decreases, which results in limited field-weakening capability.

In general, PMSMs with small dq saliency, such as the motor considered in this thesis, are characterized by low inductances, which makes them unsuitable for field-weakening operation [36].

Of course, it should be borne in mind that the controlled system does not include only the motor, but the transmission system as well. Therefore, the inductance of the equivalent motor includes the inductances of the cable and the transformers and, therefore, it is significantly higher than the inductance of the actual motor.

Although the transmission components may appear to have a positive effect on the field-weakening capability of the system, this effect is counterbalanced by the higher voltage that the VSD needs to provide, in order to compensate for the voltage drop in the transmission system.

During field-weakening operation, the voltage drop in the transmission components rises, due to the increased current magnitude. This means, that in order to supply the motor with its rated voltage, the VSD must increase its voltage output.

3.6.8 Derivation of the field-weakening algorithm

The implemented field-weakening algorithm is based on an open-loop method presented in [34]. Its mission is to generate a proper d-axis current reference, when the desired speed is higher than the rated speed of the PMSM.

For the derivation of the field-weakening function, it is assumed that the motor operates at steady state and that the resistive stator voltage drop is negligible. The latter assumption is stronger for motors with high voltage and low current ratings [30].

Under the aforementioned assumptions, the d-axis and q-axis stator voltages (given by (3.4) and (3.5) respectively) can be written as

$$u_{sd} = -\omega_r L_s i_{sq} \tag{3.54}$$

$$u_{sq} = \omega_r L_s i_{sd} + \omega_r \Psi_m \tag{3.55}$$

The stator voltage amplitude $\hat{u}_s$ must not exceed the rated voltage $\hat{u}_{s,rated}$, thus

$$\hat{u}_s \leq \hat{u}_{s,rated} \Rightarrow \sqrt{(u_{sd})^2 + (u_{sq})^2} \leq \hat{u}_{s,rated} \tag{3.56}$$

In the implemented field-weakening algorithm, the voltage $\hat{u}_{s,rated}$ is calculated from (3.54) - (3.56), by considering the rated speed $\omega_{r,rated}$ of the PMSM.

During field-weakening operation, the voltage amplitude $\hat{u}_s$ is equal to $\hat{u}_{s,rated}$. By substituting (3.54) and (3.55) into (3.56) and by solving for the d-axis current i_{sd}, the d-axis current reference i^*_{sd} is obtained as

$$i^*_{sd} = -\frac{\Psi_m}{L_s} + \frac{1}{L_s}\sqrt{(\frac{\hat{u}_{s,rated}}{\omega_r})^2 - (L_s i_{sq})^2} \tag{3.57}$$

Equation (3.57) is used for the calculation of the d-axis current reference when the estimated speed exceeds the rated speed $\omega_{r,rated}$ of the PMSM. For operation below this speed, i^*_{sd} is set to zero, according to the discussion in Section 3.5.3.

For the calculation of the d-axis current reference from (3.57), the field-weakening block uses the speed $\omega_{r,est}$ produced by the position estimator (according to (3.50)) and the q-axis current reference i^*_{sq} calculated from (3.29) during the previous sampling period.

The magnitude of the calculated d-axis current reference is limited by the current limiter (as discussed in Section 3.5.7) and is then supplied to the PI regulator of the current controller.

Chapter 4

Simulation results

This chapter presents the obtained simulation results for the designed control models.

Several startup tests are performed, in order to investigate the performance of the implemented V/f controllers and in order to optimize their parameters. Their ability to accelerate the PMSM for different initial rotor positions and their effectiveness in dealing with sudden load variations are verified.

Furthermore, the behaviour of the system during the transition from V/f control to vector control is investigated and the response of the designed vector controllers to load steps is tested.

The vector control scheme with the mechanical sensors is subjected to a startup test, so that the performance of the current regulator is verified, while the behaviour of the position estimator and the effectiveness of the implemented field-weakening alogrithm of the position-sensorless controller are evaluated through different simulations.

4.1 Open-loop V/f control

This section presents the simulation results for the implemented open-loop V/f controller.

In order to determine the settings that optimize the performance of the controller, simulations with different parameter values are performed. When it comes to V/f control schemes, it is common to select the settings of the controller by trial and error [21].

In order to ensure that the PMSM startup is successful for every initial rotor position, the behaviour of the system is investigated for several starting angles.

Moreover, the capability of the controlled system to maintain its stability after being subjected to load disturbances is tested, by performing load step-up and step-down tests.

4.1.1 Different critical frequency values

In Section 3.3.5 the critical frequency of the open-loop V/f controller was defined as the frequency value below which voltage boosting is applied. Since this value affects the control performance and the system design, it should be selected optimally.

Torque-speed characteristic of the load

The load model that has been used for the following tests is a downscaled version of the multiphase pump of the system. Its torque-speed characteristic is shown in Fig. 4.1.

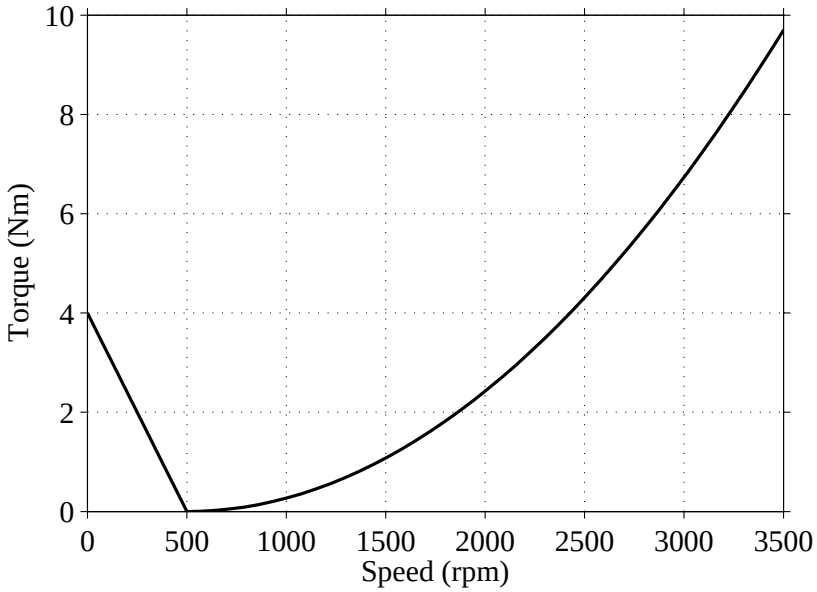

Figure 4.1: Torque-speed characteristic of the load.

The torque value that corresponds to zero speed is the breakaway torque of the load, thus the torque that the PMSM must overcome before it can start rotating. For speeds above 500 *rpm* the load torque is proportional to the square of the speed.

The characteristic of the actual pump is represented with sufficient accuracy by the torque-speed curve of the implemented load model during the startup of the motor and during operation at relatively high speeds (above 500 *rpm*).

Under other operating conditions however, this model may not be accurate. For instance, when the low-speed range is entered during deceleration, the load torque does not start

increasing, as indicated by the characteristic in Fig. 4.1.

In other words, the low-speed part of the presented load curve represents the difficulty of the system to overcome the static friction of the pump during the startup, but it cannot represent the low-speed behaviour of the pump under all operating conditions.

Effect of the critical frequency on the applied V/f ratio

The boosting factor F_b as a function of the critical frequency f_{cr} has been obtained from (3.15) and is plotted in Fig. 4.2. The equivalent stator resistance R'_s in (3.15) has been calculated by assuming that the length of the cable is such, that the voltage drop in the transmission system is approximately 10%. This requirement yields a length of around 10 km.

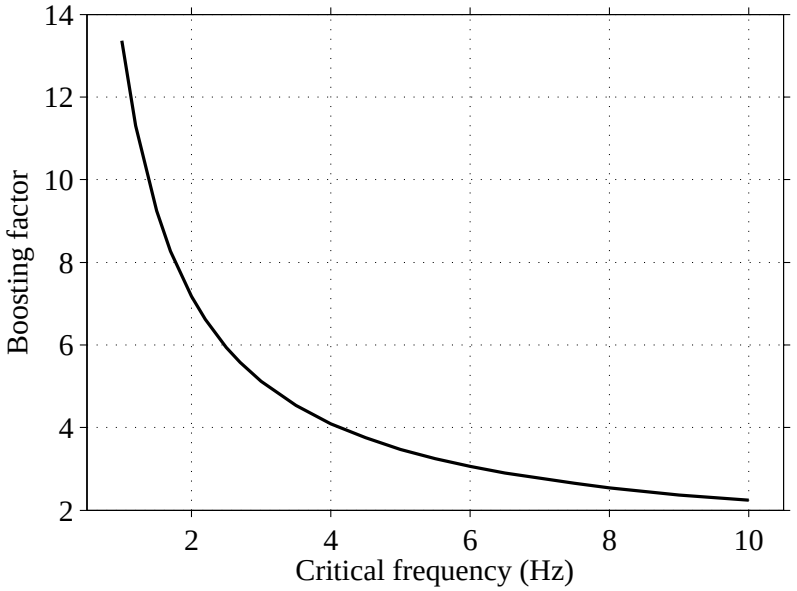

Figure 4.2: Boosting factor F_b as a function of the critical frequency f_{cr}.

Figure 4.2 demonstrates that the boosting factor increases significantly, as the critical frequency decreases. Since the applied V/f ratio is proportional to the boosting factor F_b, according to (3.16), this ratio increases for low critical frequency values.

As was discussed in Section 3.2.2, high V/f ratios result in the necessity of oversizing the topside transformer of the system. In order to minimize the size and cost of this transformer, it is necessary to minimize the applied V/f ratio, by selecting the maximum acceptable critical frequency.

The aim of the following tests is to determine the maximum critical frequency for which the PMSM can start safely.

Applied frequency reference curve

The slope of the frequency reference in the following tests is selected to be 0.83 Hz/s. Fig. 4.3 shows the applied frequency reference curve.

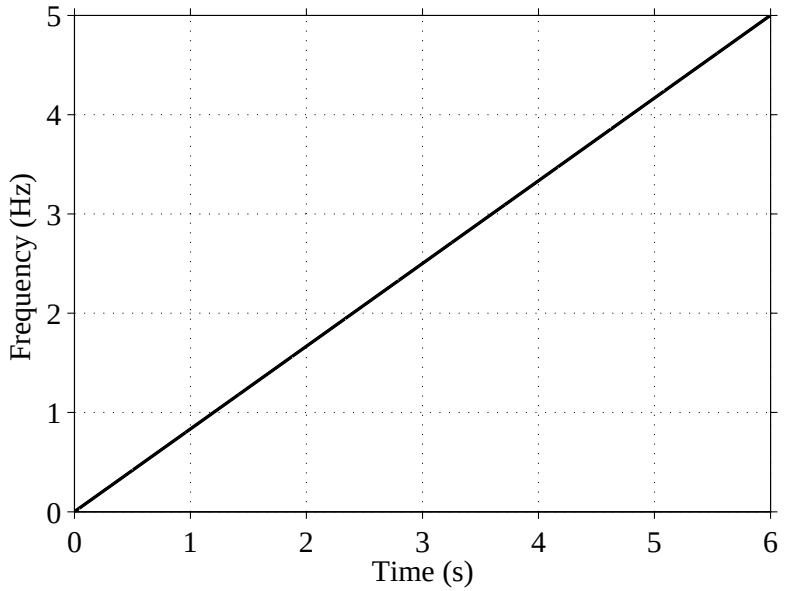

Figure 4.3: Applied frequency reference f^*.

A separate investigation on the effect of the frequency slope on the control performance is conducted in Section 4.1.2.

Startup test with low critical frequency

Initially, the behaviour of the open-loop V/f controller is investigated for $f_{cr} = 3\ Hz$. The startup performance of the PMSM in this case is shown in Fig. 4.4.

Figure 4.4 a) presents the waveform of the voltage amplitude reference $\hat{u}_s^*$. Voltage boosting is applied until $3.6s$, thus until the time instant that corresponds to the selected critical frequency of 3 Hz.

Since the applied frequency increases at a steady rate, the V/f ratio takes its maximum value during the voltage-boosting interval. This value determines the size of the topside transformer of the system.

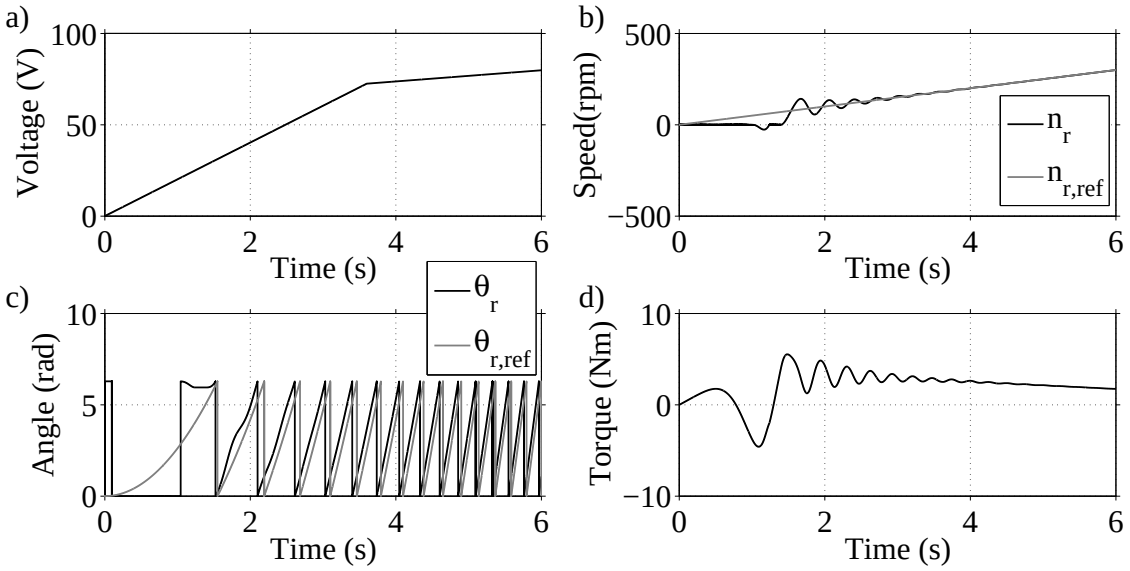

Figure 4.4: Waveforms for $f_{cr} = 3\ Hz$. a) Voltage amplitude reference $\hat{u}_s^*$. b) Actual speed n_r and speed reference n_r^*. c) Actual position θ_r and position reference θ_r^*. d) Electromagnetic torque T_e.

It can be found by combining Fig. 4.3 and 4.4 a) (or by using (3.16)) that the V/f ratio that is applied during the initial accelerating interval is approximately equal to 24.17 V/Hz. Compared to the rated ratio of the PMSM (4.90 V/Hz), this value is extremely large and increases the required size of the topside transformer significantly.

Figure 4.4 b) presents the waveforms of the mechanical rotor speed n_r and the speed reference n_r^*. It is apparent that the startup in this case is successful, since the motor manages to establish synchronism with the supplied field after a few oscillations.

It is worth noticing that the PMSM rotates in the negative direction for a short time interval, before starting to accelerate in the positive direction. The maximum negative speed that is reached in this interval is around 26.5 rpm. The issue of temporary reverse rotation is common for PMSMs [22, 23, 29] and is investigated further in Section 4.1.3.

Figure 4.4 c) shows the waveforms of the rotor position θ_r and the position reference θ_r^*. Due to the inertia of the rotor and the load, it takes some time (approximately $2s$) for the PMSM to follow the rotation of the supplied field.

In Fig. 4.4 d), the waveform of the electromagnetic torque T_e is presented. The initial lack of synchronism is accompanied by torque oscillations. For a while, the torque becomes negative, reaching a negative maximum of 4.6 Nm, which causes the reverse rotation of Fig. 4.4 b).

Figure 4.5 shows the voltages and currents at the output of the VSD.

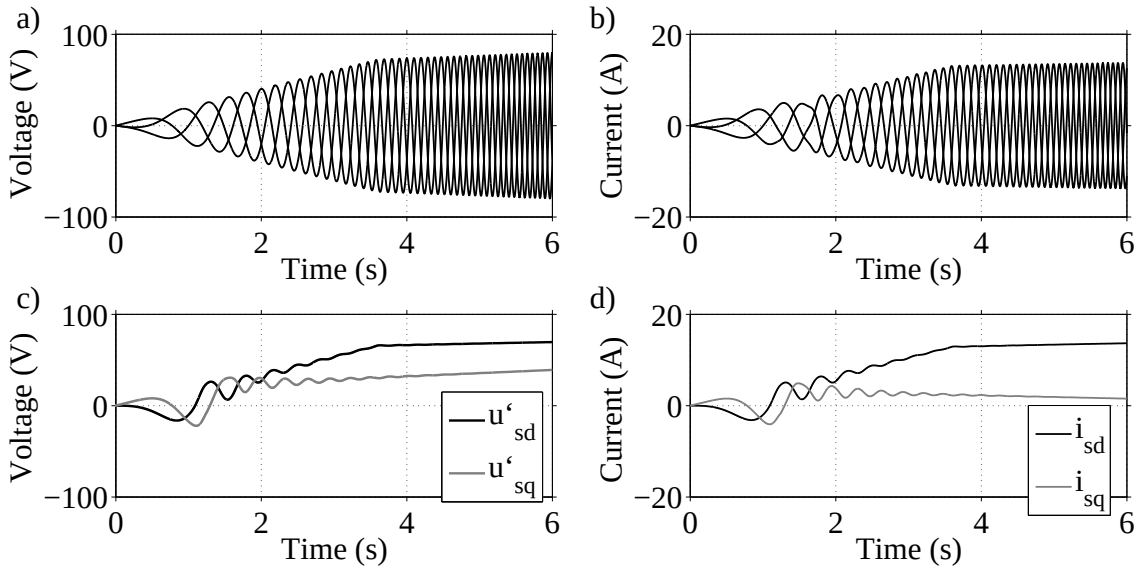

Figure 4.5: Waveforms for $f_{cr} = 3\ Hz$. a) Equivalent stator voltages u'_{sa}, u'_{sb}, u'_{sc}. b) Stator currents i_{sa}, i_{sb}, i_{sc}. c) Equivalent stator voltages u'_{sd}, u'_{sq}. d) Stator currents i_{sd}, i_{sq}.

The gradual increase of the electrical frequency and voltage magnitude is demonstrated in Fig. 4.5 a), while Fig. 4.5 b) shows that the stator current amplitude is high during the startup (reaching an rms value of over 9.9 A), temporarily exceeding the rated current of the PMSM.

High startup currents are a common problem in open-loop V/f control schemes. For instance, such a scheme was tested in [21] and its starting performance was evaluated as poor, due to the initial overcurrents experienced by the PMSM.

Figure 4.5 d) reveals that the high stator current can be mainly attributed to the high magnetizing current i_{sd}, which indicates that the PMSM experiences overexcitation during its startup. A similar case was presented in [20]. Since V/f control does not allow direct current control, it cannot provide optimal efficiency during the startup process.

The torque-producing current component i_{sq} on the other hand, is rather low. It reaches a maximum value quite early, but then gradually falls, after the breakaway torque of the system is overcome.

Figure 4.6 presents the voltages of the PMSM.

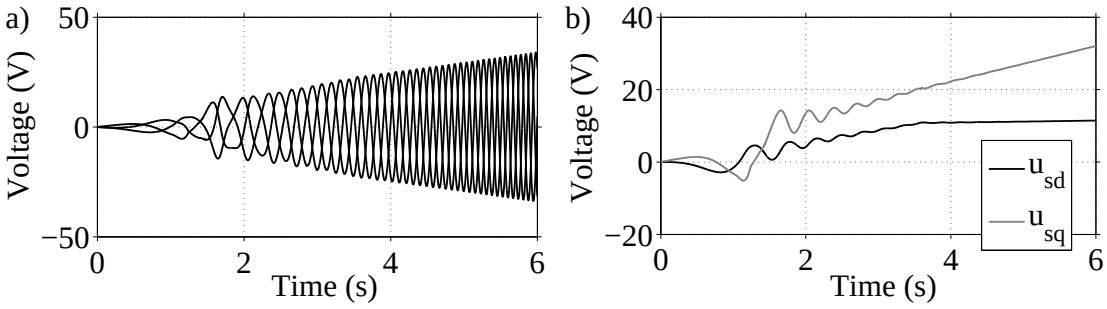

Figure 4.6: Waveforms for $f_{cr} = 3\ Hz$. a) Stator voltages u_{sa}, u_{sb}, u_{sc}. b) Stator voltages u_{sd}, u_{sq}.

It can be observed by comparing Fig. 4.5 and Fig. 4.6 that the presence of the transmission system causes a temporary distortion in the waveforms of the motor voltage. More importantly, the voltage drop in the transmission components reduces the PMSM voltage significantly.

Although the cable length in the performed tests has been selected such, that the steady-state voltage drop is approximately 10% of the VSD voltage, this drop becomes almost 70% at $4s$. The reason for this extremely high value is the high startup current, which was observed in Fig. 4.5.

Startup test with medium critical frequency

For the next test, the critical frequency is increased to $f_{cr} = 6\ Hz$. The startup behaviour of the PMSM in this case is shown in Fig. 4.7.

It can be found from Fig. 4.3 and 4.7 a) that the V/f ratio that is applied during the voltage-boosting interval is approximately equal to 14.44 V/Hz. Although this value is higher than the rated V/f ratio of the PMSM, it is approximately 40% lower than in the case of $f_{cr} = 3\ Hz$.

However, it is obvious from Fig. 4.7 that the decreased V/f ratio during the voltage-boosting interval comes at the cost of worse control performance. The reduced voltage that is provided to the PMSM during the early accelerating stage makes it harder for the rotor to establish synchronism with the supplied field.

As shown in Fig. 4.7 d), the torque oscillations are more severe in this case, reaching a higher negative maximum of approximately 6.1 Nm. These oscillations result in two intervals of negative speed, as shown in Fig. 4.7 b). In this case, the PMSM reaches a maximum negative speed of around 63.2 rpm.

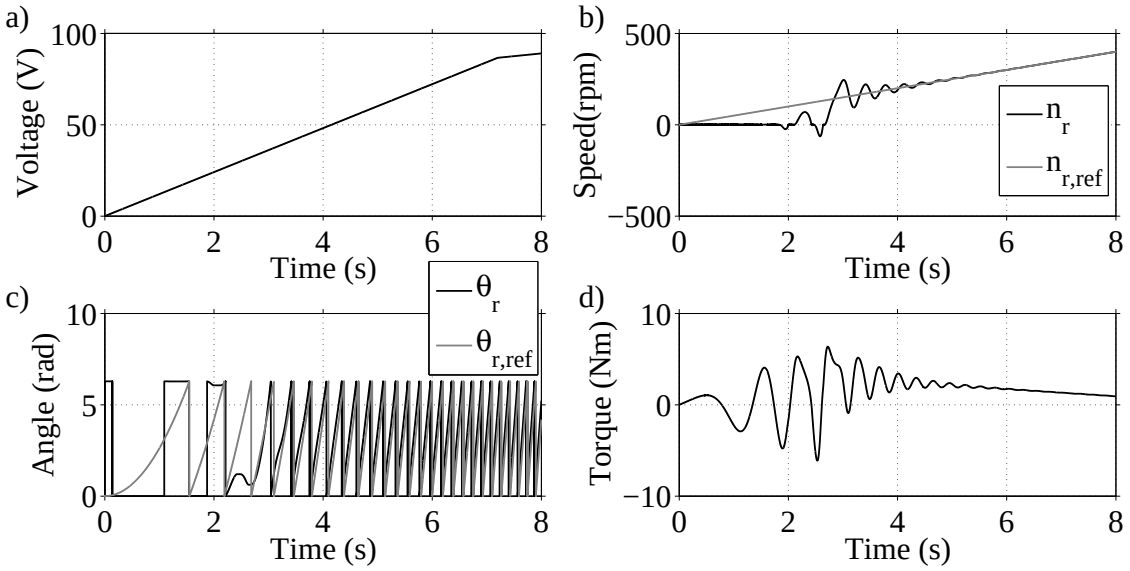

Figure 4.7: Waveforms for $f_{cr} = 6\ Hz$. a) Voltage amplitude reference $\hat{u}_s^*$. b) Actual speed n_r and speed reference n_r^*. c) Actual position θ_r and position reference θ_r^*. d) Electromagnetic torque T_e.

Figure 4.7 c) demonstrates that it takes around $2.8s$ for the rotor to establish synchronism with the field, which is 40% more than in the case of $f_{cr} = 3\ Hz$.

Figure 4.8 presents the voltages and currents at the output of the VSD.

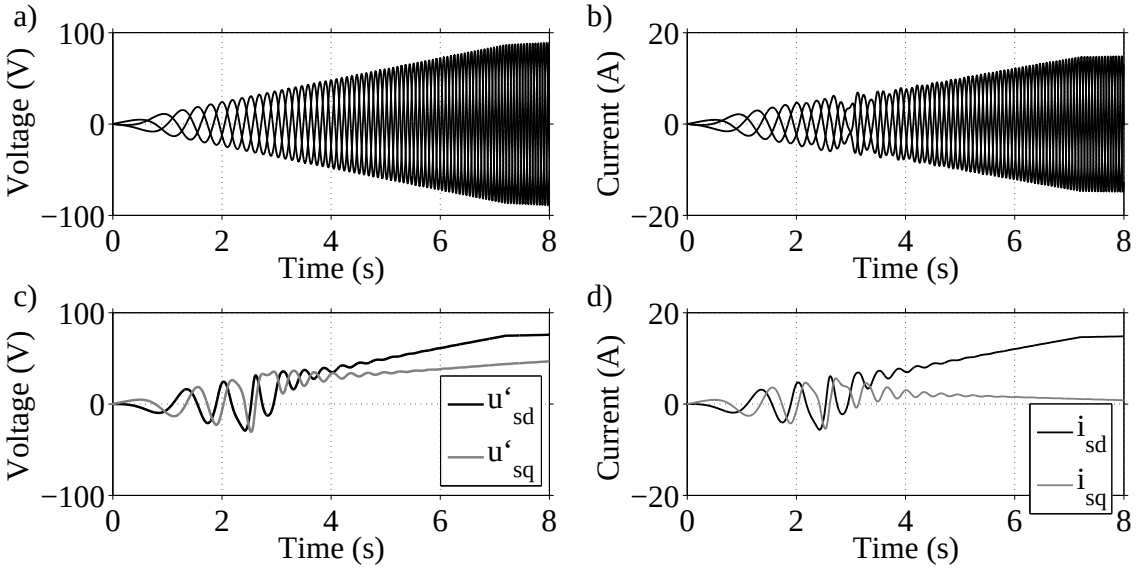

Figure 4.8: Waveforms for $f_{cr} = 6\ Hz$. a) Equivalent stator voltages u'_{sa}, u'_{sb}, u'_{sc}. b) Stator currents i_{sa}, i_{sb}, i_{sc}. c) Equivalent stator voltages u'_{sd}, u'_{sq}. d) Stator currents i_{sd}, i_{sq}.

It can be found from Fig. 4.8 b) that the stator current is even higher than in the case

of $f_{cr} = 3\ Hz$ (reaching an rms value of over 10.4 A). Compared to 4.5 b), the current waveform in this case is more distorted, as a result of the increased difficulty of the PMSM to achieve synchronism.

The voltages of the PMSM are presented in Fig. 4.9.

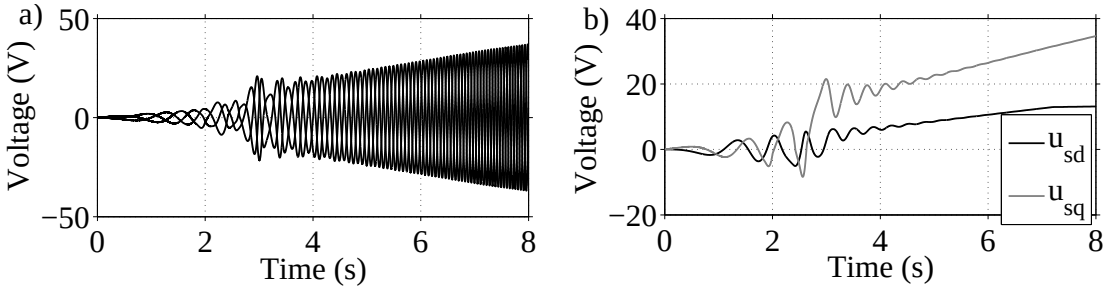

Figure 4.9: Waveforms for $f_{cr} = 6\ Hz$. a) Stator voltages u_{sa}, u_{sb}, u_{sc}. b) Stator voltages u_{sd}, u_{sq}.

Similarly to the case of $f_{cr} = 3\ Hz$, the distortion in the voltage waveforms of the motor is noticeable and the voltage drop in the transmission system becomes almost 60% at $7.5s$.

Startup test with high critical frequency

For the next test, the critical frequency is increased to $f_{cr} = 9\ Hz$. The startup behaviour of the PMSM in this case is shown in Fig. 4.10.

The applied V/f ratio has decreased to approximately 11.20 V/Hz, but the PMSM startup is unsuccessful. As shown in Fig. 4.10 d), the motor experiences torque oscillations of increasing magnitude, which cause the rotor to vibrate, as can be seen in Fig. 4.10 b). The inability of the PMSM to establish synchronism is clearly demonstrated in 4.10 c).

Figure 4.11 presents the voltages and currents at the output of the VSD.

The abnormal operation of the PMSM is reflected in the oscillations in the d-axis and q-axis voltage and current waveforms (shown in 4.11 c) and 4.11 d) respectively).

Selection of critical frequency

The performed tests clearly demonstrate that as the critical frequency of the V/f controller increases, the V/f ratio of the VSD decreases, but the control performance deteriorates.

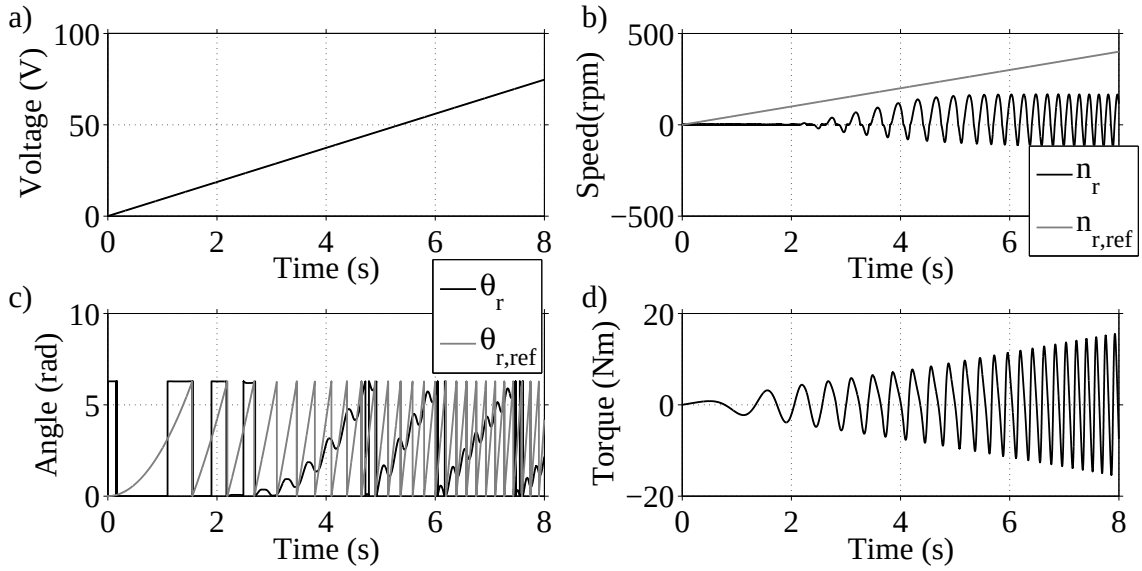

Figure 4.10: Waveforms for $f_{cr} = 9\ Hz$. a) Voltage amplitude reference $\hat{u}_s^*$. b) Actual speed n_r and speed reference n_r^*. c) Actual position θ_r and position reference θ_r^*. d) Electromagnetic torque T_e.

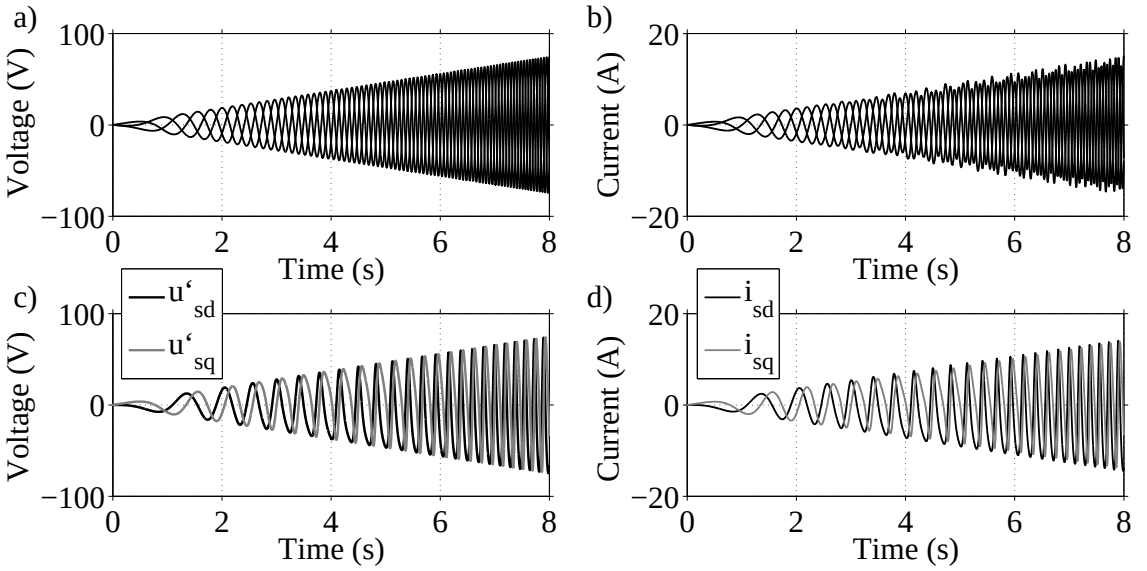

Figure 4.11: Waveforms for $f_{cr} = 9\ Hz$. a) Equivalent stator voltages u'_{sa}, u'_{sb}, u'_{sc}. b) Stator currents i_{sa}, i_{sb}, i_{sc}. c) Equivalent stator voltages u'_{sd}, u'_{sq}. d) Stator currents i_{sd}, i_{sq}.

It can be concluded that the selection of the critical frequency must be based on a compromise between the safe and smooth startup of the PMSM and the size and cost of the topside transformer of the system.

After performing simulations for different critical frequencies, it has been found that the maximum value that results in successful startup of the PMSM is $f_{cr} \simeq 7.7\ Hz$. This

value corresponds to a V/f ratio of about 12.30 V/Hz.

Since V/f control schemes are often prone to instability, due to their sensitivity to disturbances (such as sudden load changes), a safety margin should be considered during the selection of the critical frequency. Therefore, a value of $f_{cr} = 5.5\ Hz$, corresponding to a V/f ratio of about 15.33 V/Hz, can be selected.

4.1.2 Different frequency reference slopes

For the tests in Section 4.1.1, the frequency reference slope was kept constant and equal to 0.83 Hz/s. In the following tests on the other hand, the critical frequency is kept constant and equal to 5.5 Hz and the effect of the frequency slope on the control performance is investigated.

Startup test with low frequency reference slope

Initially, the behaviour of the open-loop V/f controller is investigated for a frequency slope of 0.5 Hz/s. The startup performance of the PMSM in this case is shown in Fig. 4.12.

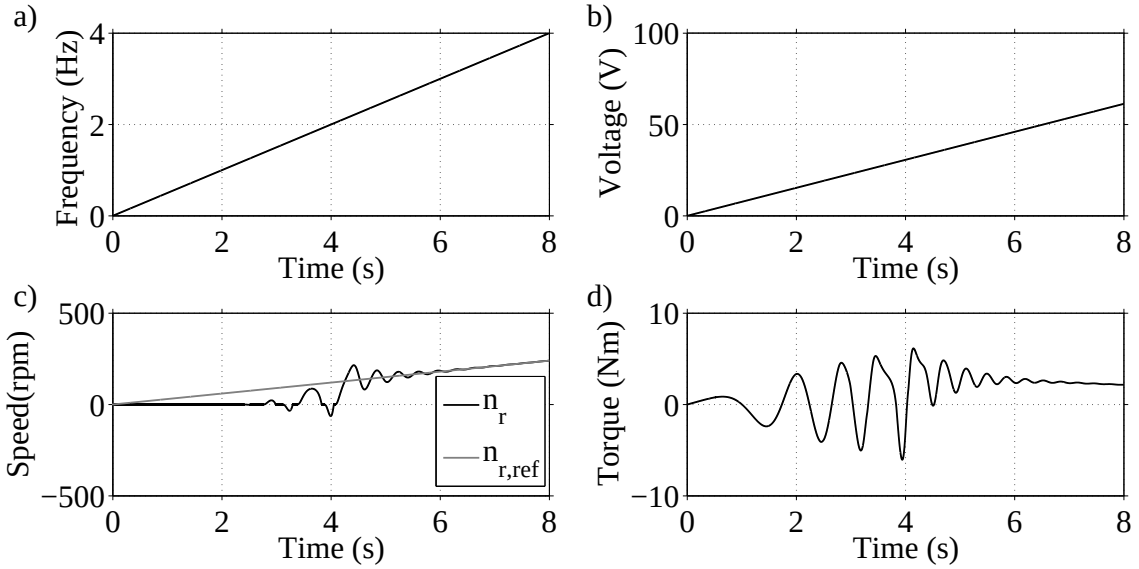

Figure 4.12: Waveforms for $df^*/dt = 0.5\ Hz/s$. a) Frequency reference f^* b) Voltage amplitude reference $\hat{u}_s^*$. c) Actual speed n_r and speed reference n_r^*. d) Electromagnetic torque T_e.

It can be seen in Fig. 4.12 d) that the motor experiences torque oscillations that last for around $6s$. The maximum negative value of these oscillations is approximately 6.1 Nm.

As a result, there are two intervals of negative speed, before synchronism is established. It can be observed in Fig. 4.12 c) that the PMSM reaches a maximum negative speed of approximately 64 *rpm*.

Figure 4.13 shows the voltages and currents at the output of the VSD.

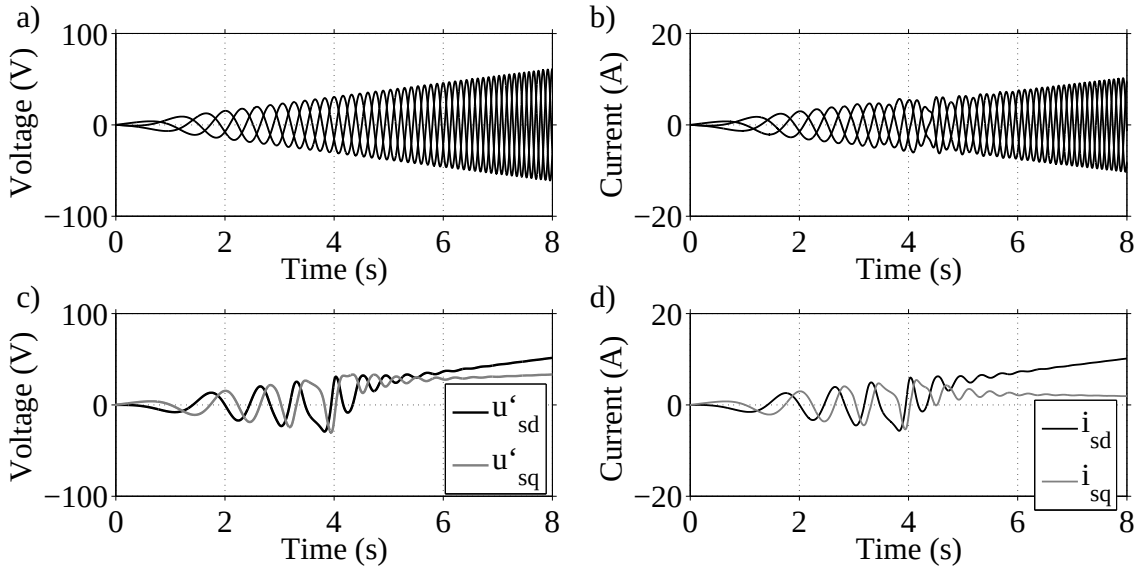

Figure 4.13: Waveforms for $df^*/dt = 0.5\ Hz/s$. a) Equivalent stator voltages u'_{sa}, u'_{sb}, u'_{sc}. b) Stator currents i_{sa}, i_{sb}, i_{sc}. c) Equivalent stator voltages u'_{sd}, u'_{sq}. d) Stator currents i_{sd}, i_{sq}.

The long duration of the oscillations in Fig. 4.13 c) and Fig. 4.13 d) reflects the difficulty of the PMSM to establish synchronism. Moreover, the positive d-axis current in Fig. 4.13 d) indicates that the motor experiences overexcitation during its startup.

The current magnitude during the startup process exceeds the rated current of the PMSM (reaching a maximum *rms* value of approximately 10.2 *A* at around 11.1*s*).

The voltages of the PMSM are presented in Fig. 4.14.

From Fig. 4.13 a) and Fig. 4.14 a), it can be found that the voltage drop in the transmission system at 5.9*s* is approximately 61% of the VSD voltage.

Startup test with medium frequency reference slope

For the next test, the frequency slope is increased to 8 Hz/s. The startup behaviour of the PMSM in this case is shown in Fig. 4.15.

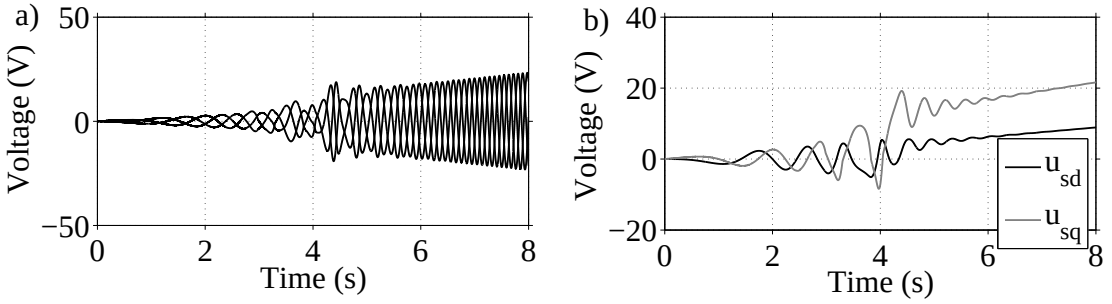

Figure 4.14: Waveforms for $df^*/dt = 0.5\ Hz/s$. a) Stator voltages u_{sa}, u_{sb}, u_{sc}. b) Stator voltages u_{sd}, u_{sq}.

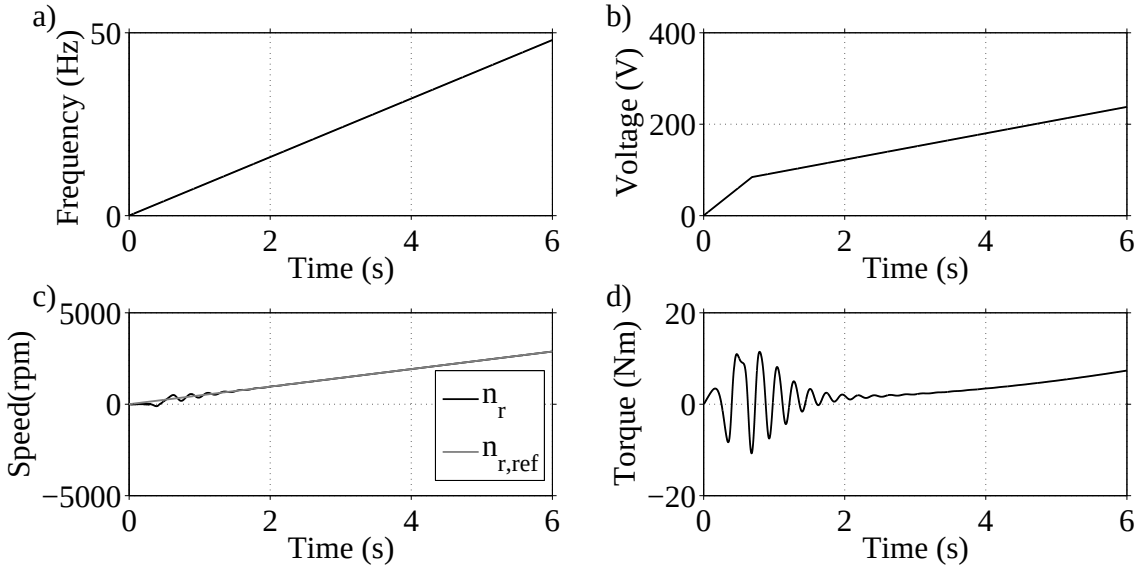

Figure 4.15: Waveforms for $df^*/dt = 8\ Hz/s$. a) Frequency reference f^* b) Voltage amplitude reference $\hat{u}_s^*$. c) Actual speed n_r and speed reference n_r^*. d) Electromagnetic torque T_e.

Figure 4.15 d) demonstrates that the torque oscillations reach a higher negative maximum (approximately 10.8 Nm), but their duration is significantly shorter (around $2s$).

As shown in Fig. 4.15 c), the startup in this case is 16 times faster than in the previous case. The PMSM experiences a single interval of reverse rotation, in which a maximum negative speed of 110 rpm is reached.

Figure 4.16 shows the voltages and currents at the output of the VSD. For the sake of clarity, the three-phase quantities have been plotted for a limited time interval (since the frequency of these quantities becomes high quite early in this case).

It can be seen in Fig. 4.16 b) that the current magnitude during the initial stage of the startup is high (reaching a maximum rms value of over 12.3 A, which clearly exceeds the rated current of the PMSM.)

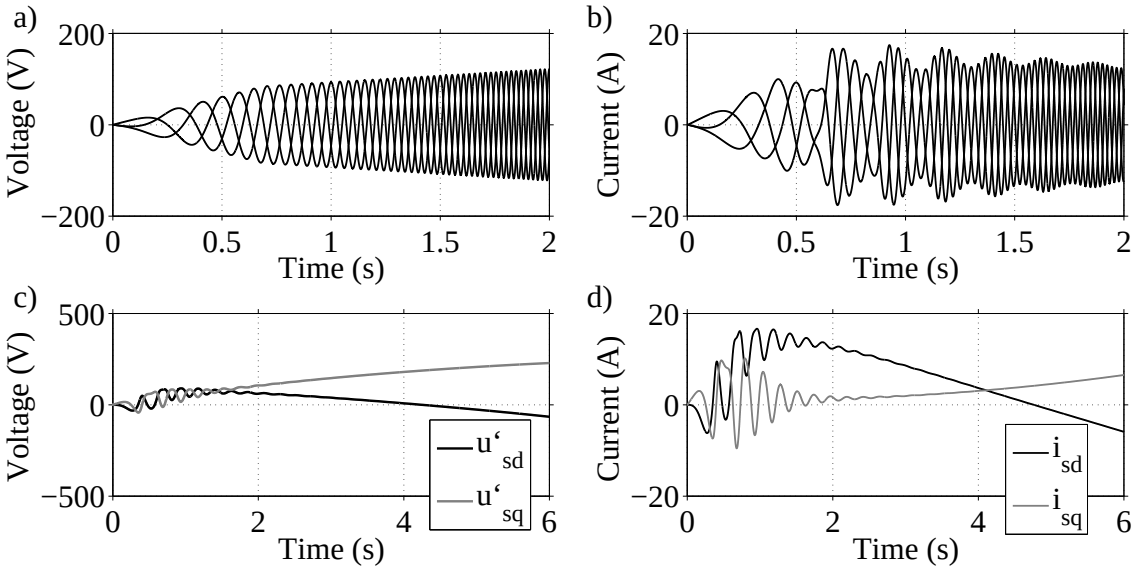

Figure 4.16: Waveforms for $df^*/dt = 8\ Hz/s$. a) Equivalent stator voltages u'_{sa}, u'_{sb}, u'_{sc}. b) Stator currents i_{sa}, i_{sb}, i_{sc}. c) Equivalent stator voltages u'_{sd}, u'_{sq}. d) Stator currents i_{sd}, i_{sq}.

Figure 4.16 d) shows that despite the initial overexcitation, the d-axis current becomes negative after approximately $4.9s$. As explained below, this result is related to the cross-coupling effect in the PMSM.

As the load torque increases with speed, the q-axis current rises. This causes an increase in the q-axis voltage according to (3.5) and a decrease in the d-axis voltage according to (3.4). These considerations are in agreement with the results in Fig. 4.16 c).

The decrease in the d-axis voltage results in a decrease in the d-axis current according to (3.4). Eventually, this current becomes negative, causing the PMSM to become under-excited.

The voltages of the PMSM are presented in Fig. 4.17.

From Fig. 4.16 a) and Fig. 4.17 a) it can be found that the voltage drop in the transmission system at the instant when the current magnitude is maximum (around $0.9s$) is approximately 60% of the VSD voltage.

Startup test with high frequency reference slope

For the next test, the frequency slope is increased to 17 Hz/s. The startup behaviour of the PMSM in this case is shown in Fig. 4.18.

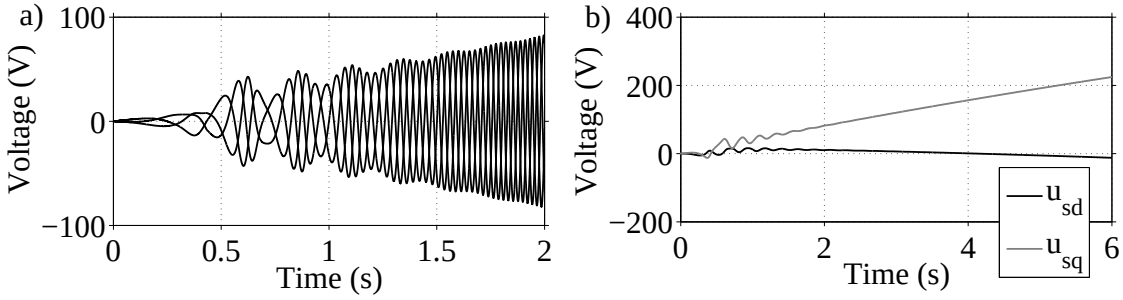

Figure 4.17: Waveforms for $df^*/dt = 8\ Hz/s$. a) Stator voltages u_{sa}, u_{sb}, u_{sc}. b) Stator voltages u_{sd}, u_{sq}.

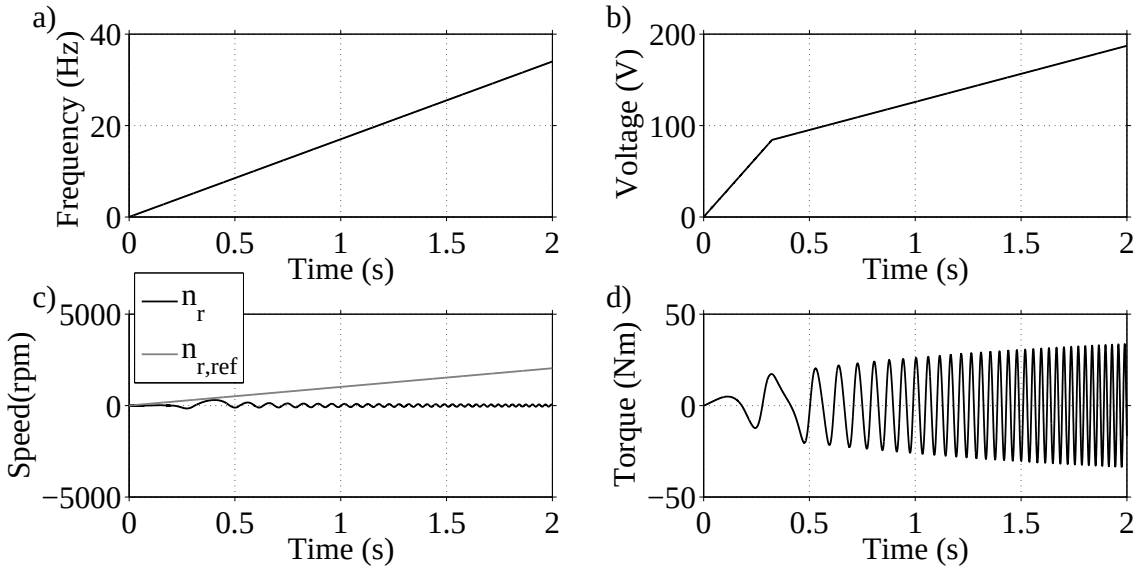

Figure 4.18: Waveforms for $df^*/dt = 17\ Hz/s$. a) Frequency reference f^* b) Voltage amplitude reference $\hat{u}_s^*$. c) Actual speed n_r and speed reference n_r^*. d) Electromagnetic torque T_e.

Apparently, the startup in this case is unsuccessful. As shown in Fig. 4.18 d), the motor experiences torque oscillations of increasing magnitude, which result in mechanical vibrations, as can be seen in Fig. 4.18 c).

As was discussed in Section 3.3.2, the rate at which the supplied frequency increases should be kept adequately low. High values of the frequency slope (such as the one selected in this test) may result in the inability of the rotor to follow the supplied field.

Selection of frequency reference slope

The performed tests demonstrate that for lower values of the frequency slope, it takes more time for the PMSM to establish synchronism with the supplied field and to reach its target speed.

Higher slopes on the other hand, result in faster accelerations and make it possible for the PMSM to get synchronized with the field earlier. However, the magnitude of the occuring torque oscillations becomes higher and results in higher speeds in the negative direction.

When a certain slope value is exceeded, the PMSM can no longer cope with the rapid frequency increase and ends up vibrating. After performing simulations for different frequency reference slopes, this value has been found to be approximately 15.1 Hz/s.

In order to avoid high torque oscillations and high negative speeds, a relatively low frequency slope of 1.5 Hz/s is selected for the open-loop V/f controller.

4.1.3 Different initial rotor positions

For the startup tests that have been performed up to this point, it has been assumed that the initial rotor angle is zero. In practice however, the initial position is not known. Therefore, it is necessary to ensure that the V/f controller can accelerate the motor successfully for every possible angle.

For the following simulations, the critical frequency of the controller is set equal to 5.5 Hz and the frequency reference slope is selected to be 1.5 Hz/s.

Loaded startup test

Initially, the startup performance of the PMSM is investigated for several starting angles, when the motor is coupled to the load which was introduced in Section 4.1.1.

The actual speed and the speed reference of the PMSM for different initial rotor positions are shown in Fig. 4.19.

Figure 4.19 demonstrates that the startup performance of the system is affected by the initial position of the rotor. Different angles result in different speeds during the reverse rotation of the PMSM.

By performing startup tests for several starting positions, the maximum speed magnitude during the reverse rotation has been obtained as a function of the initial rotor angle and is shown in Fig. 4.20.

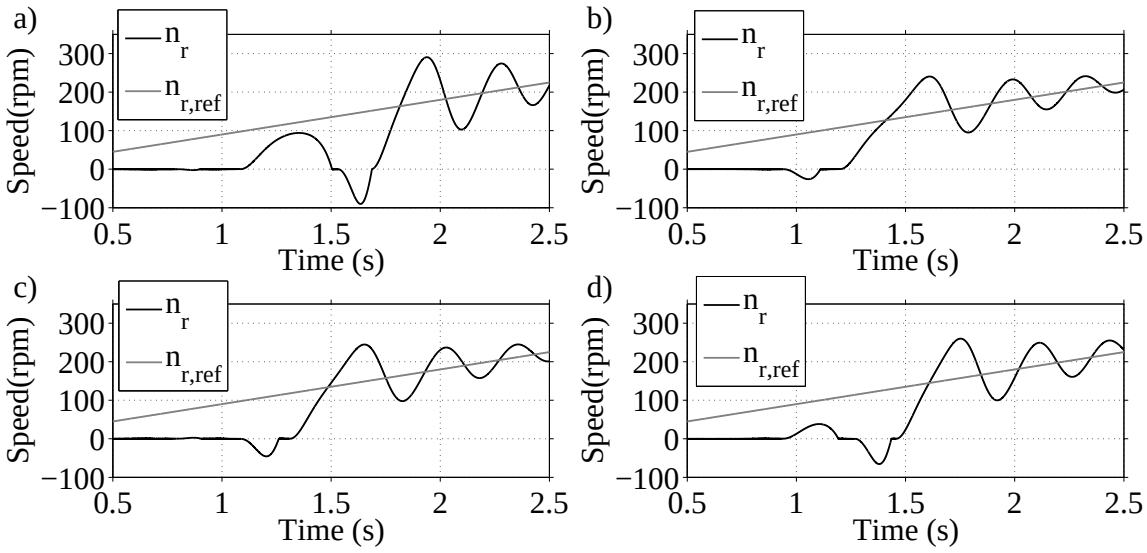

Figure 4.19: Actual speed n_r and speed reference n_r^* for loaded operation. a) $\phi_0 = 0^o$. b) $\phi_0 = 90^o$. c) $\phi_0 = 180^o$. d) $\phi_0 = 270^o$.

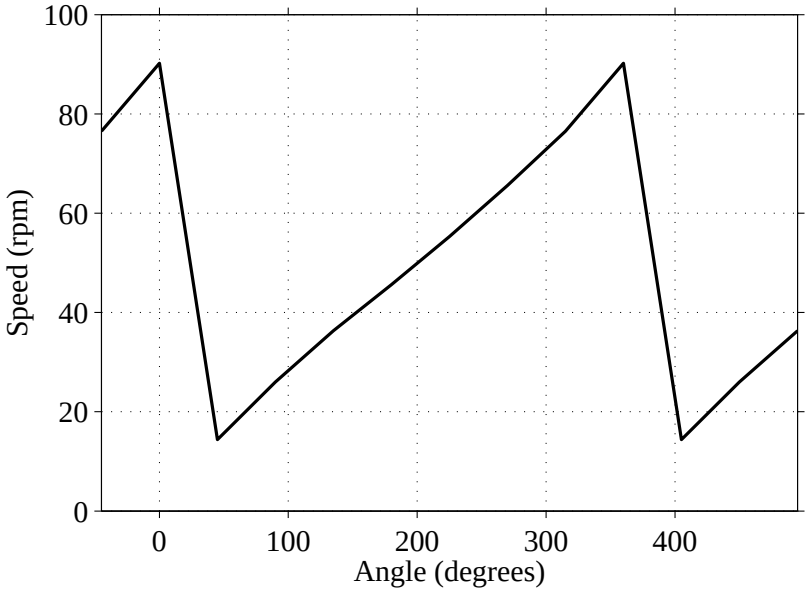

Figure 4.20: Maximum speed magnitude $|n_r|_{max}$ during reverse rotation as a function of the initial rotor angle ϕ_0 for loaded operation.

The maximum speed magnitude that the PMSM experiences during a reverse-rotation interval is approximately 90.2 *rpm* and occurs for $\phi_0 \simeq 0^o$. On the other hand, the smoothest startup occurs for $\phi_0 \simeq 45^o$. The maximum magnitude of the negative speed in this case is approximately 14.4 *rpm*.

Although the smoothness of the startup varies depending on the initial rotor position, the open-loop V/f controller has managed to accelerate the motor successfully for all tested angles.

Knowing the initial angles that result in the smoothest startup, it would be useful to bring the rotor to a favourable position, before accelerating the PMSM. In a common drive system, this could be achieved by supplying the motor with a proper DC current for a short time interval before the startup.

In the investigated system however, this is not possible, since the injection of a DC current would saturate the core of the transformers.

No-load startup test

In general, the performance of V/f control schemes depends on the load conditions of the motor [5]. For the following test, the starting behaviour of the system is investigated for several initial positions, when the PMSM is not loaded.

The actual speed and the speed reference for different starting angles are shown in Fig. 4.21.

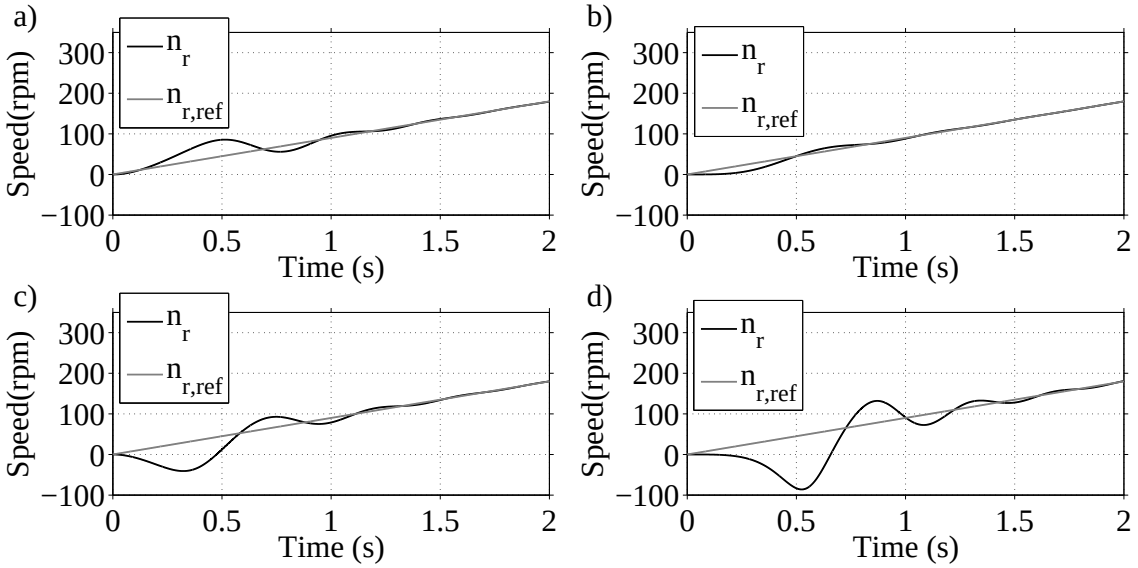

Figure 4.21: Actual speed n_r and speed reference n_r^* for no-load operation. a) $\phi_0 = 0^o$. b) $\phi_0 = 90^o$. c) $\phi_0 = 180^o$. d) $\phi_0 = 270^o$.

Figure 4.21 demonstrates that reverse rotation during the no-load startup occurs only for some initial positions (such as $\phi_0 = 180^o$ and $\phi_0 = 270^o$), while for others, no negative speeds appear (for instance $\phi_0 = 0^o$ and $\phi_0 = 90^o$).

The dependence of the startup performance on the load conditions becomes apparent,

when Fig. 4.19 and Fig. 4.21 are compared. The startup in the latter case is smoother for all tested angles, thus the rotor of the PMSM manages to follow the rotation of the supplied field with less difficulty.

4.1.4 Response to load steps

The aim of the following tests is to evaluate the capability of the system to maintain its stability after being subjected to load disturbances, while operating under open-loop V/f control.

Load step-up test

For this test, the open-loop V/f controller accelerates the PMSM up to a relatively high speed. At some point of the simulation, a load step-up is applied and the response of the system is shown in Fig. 4.22.

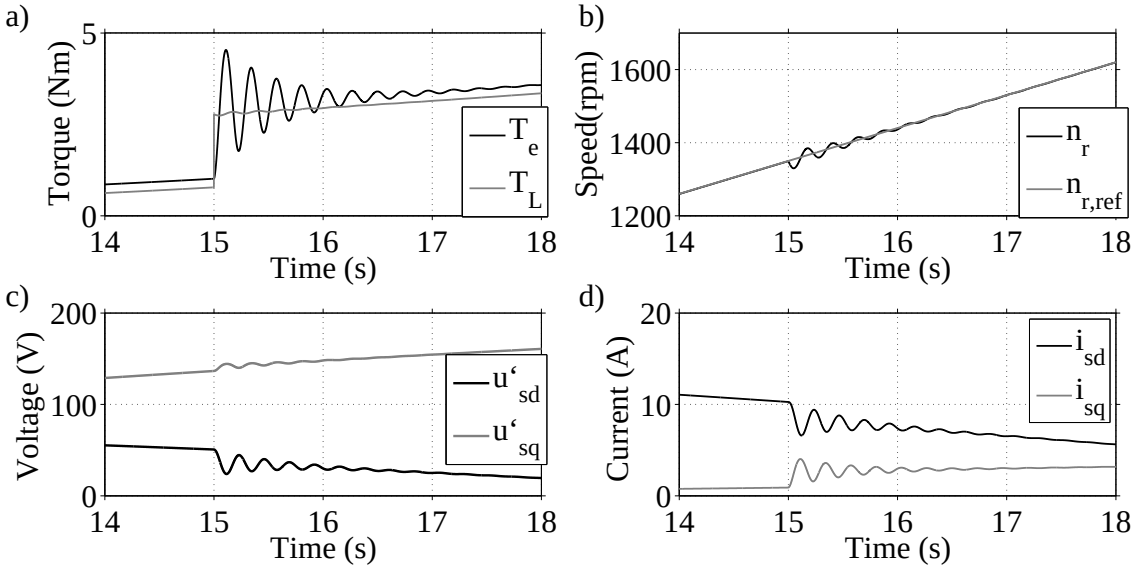

Figure 4.22: Response of the system to the load step-up. a) Electromagnetic torque T_e and load torque T_L. b) Actual speed n_r and speed reference n_r^*. c) Equivalent stator voltages u'_{sd}, u'_{sq}. d) Stator currents i_{sd}, i_{sq}.

As shown in Fig. 4.22 a), the load torque is suddenly increased by 2 Nm at 15s. The PMSM experiences electromagnetic torque oscillations of decreasing magnitude, which result in temporary speed pulsations, as shown in Fig. 4.22 b).

In response to the increased load torque, the q-axis stator current increases, while the d-axis current decreases due to the cross-coupling effect. This is shown in Fig. 4.22 d).

The system seems to respond quite well to the sudden load increase. The torque and speed oscillations are successfully damped and the rotor of the PMSM stays synchronized with the supplied field.

Load step-down test

For this test, the mechanical load is stepped down and the response of the system is shown in Fig. 4.23.

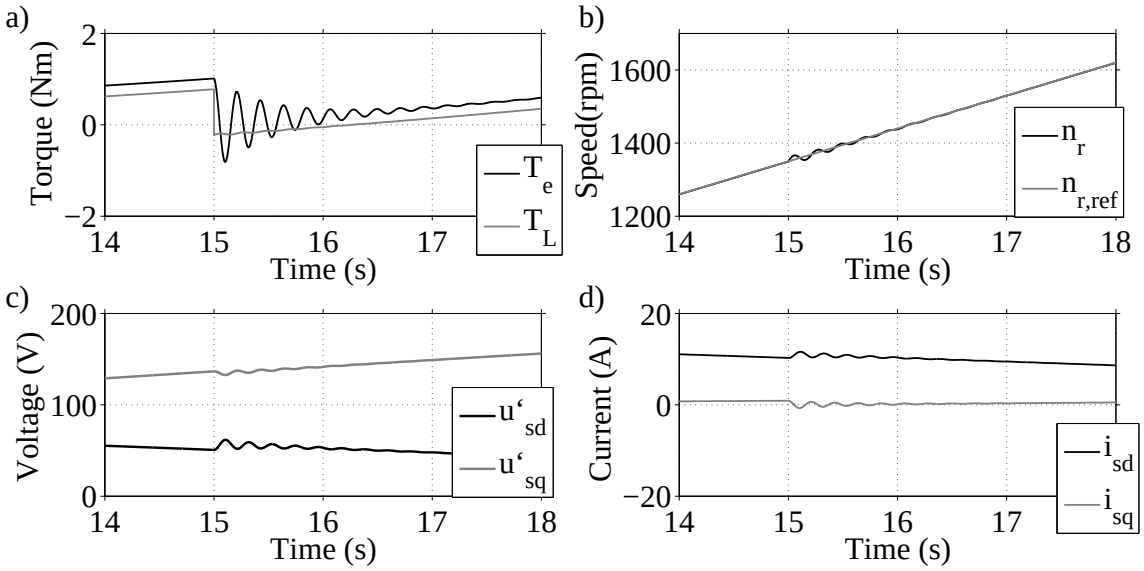

Figure 4.23: Response of the system to the load step-down. a) Electromagnetic torque T_e and load torque T_L. b) Actual speed n_r and speed reference n_r^*. c) Equivalent stator voltages u'_{sd}, u'_{sq}. d) Stator currents i_{sd}, i_{sq}.

As shown in Fig. 4.23 a), the load torque is decreased by 1 Nm at 15s. The resulting torque oscillations and speed pulsations are successfully damped and synchronism is maintained.

The decrease of the load torque causes the q-axis current to fall and the d-axis current to rise. This results in an increase in the d-axis voltage and a decrease in the q-axis voltage in accordance with (3.4) and (3.5) respectively.

4.2 Closed-loop V/f control

This section presents the simulation results for the implemented closed-loop V/f controller.

The startup performance of the controller is tested for different values of the frequency reference slope and various initial rotor positions. Moreover, the response of the controlled system to load disturbances is evaluated, by performing load step-up and step-down tests.

4.2.1 Different frequency reference slopes

In the following tests, the startup behaviour of the closed-loop V/f controller is examined for different slopes of the supplied frequency. Based on the results of these tests, a proper value for the frequency reference slope is selected.

Startup test with low frequency reference slope

The startup behaviour of the closed-loop V/f controller for a frequency slope of 0.5 Hz/s is shown in Fig. 4.24.

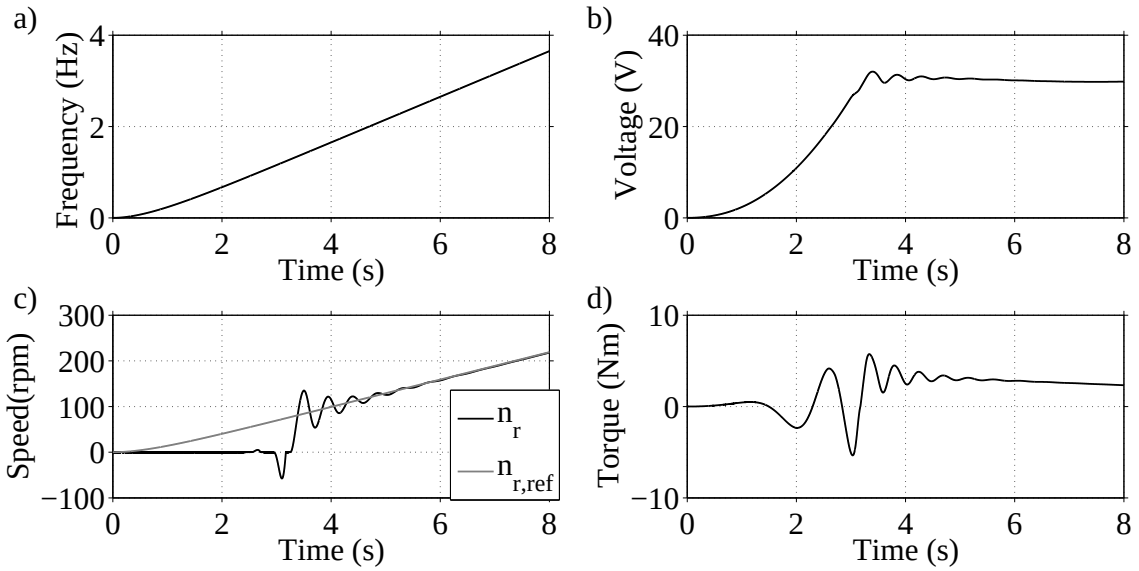

Figure 4.24: Waveforms for $df^*/dt = 0.5\ Hz/s$. a) Frequency reference f^* b) Voltage amplitude reference $\hat{u}_s^*$. c) Actual speed n_r and speed reference n_r^*. d) Electromagnetic torque T_e.

Figure 4.24 d) shows that the PMSM experiences torque oscillations, which reach a negative maximum of approximately 5.4 Nm. As in the case of open-loop V/f control, this results in temporary negative speeds, which reach a maximum magnitude of approximately 58 rpm, as shown in Fig. 4.24 c).

In contrast to the open-loop controller, where there are only two voltage magnitude slopes (one during voltage boosting and one afterwards), the slope in the closed-loop controller is constantly adjusted to the instantaneous values of the measured currents. Figure 4.24

b) demonstrates that the slope can even take negative values.

Figure 4.25 presents the applied V/f ratio as a function of time. It can be observed that a maximum ratio of approximately 24 V/Hz is reached at around 3.3s.

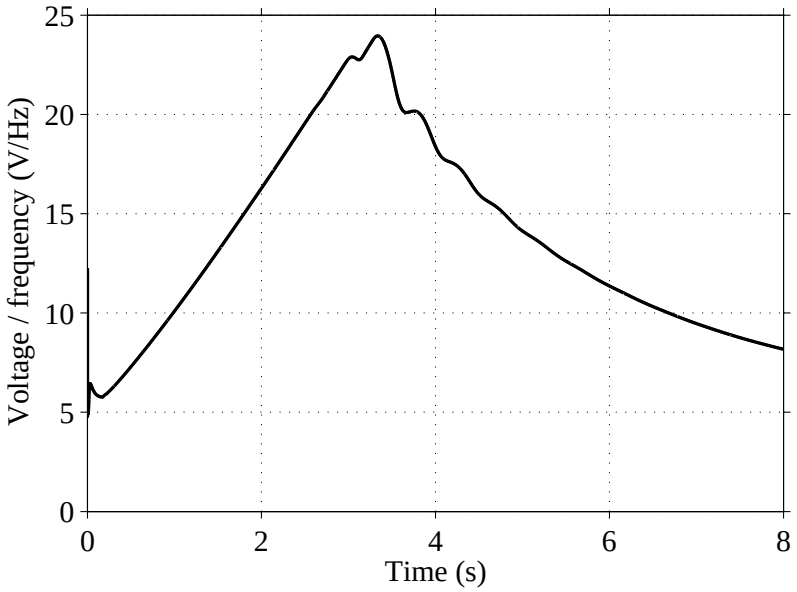

Figure 4.25: Applied V/f ratio as a function of time for $df^*/dt = 0.5\ Hz/s$.

Figure 4.26 presents the voltages and currents at the output of the VSD.

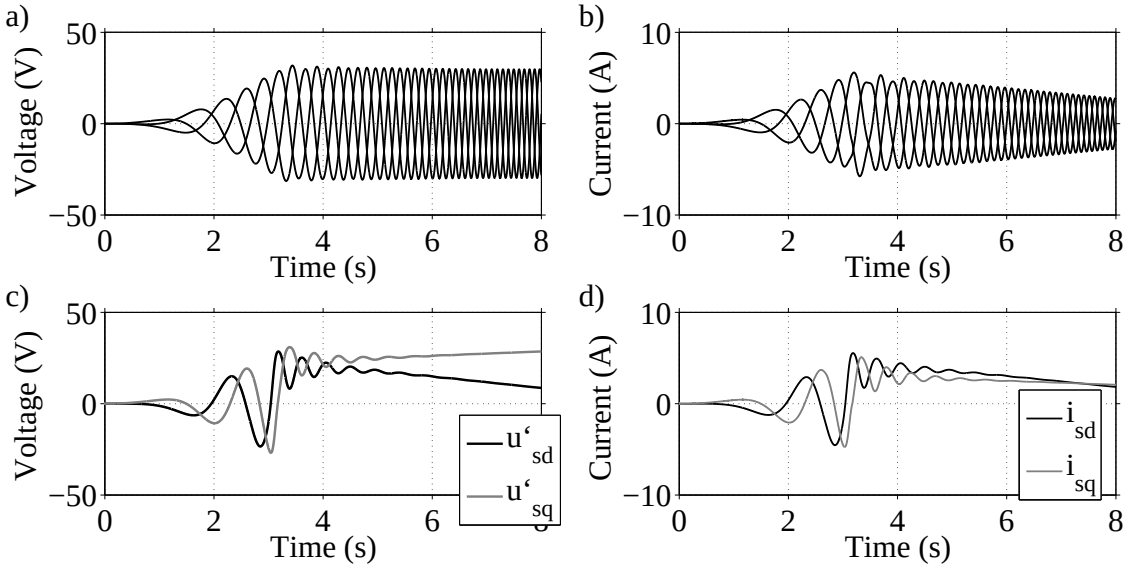

Figure 4.26: Waveforms for $df^*/dt = 0.5\ Hz/s$. a) Equivalent stator voltages u'_{sa}, u'_{sb}, u'_{sc}. b) Stator currents i_{sa}, i_{sb}, i_{sc}. c) Equivalent stator voltages u'_{sd}, u'_{sq}. d) Stator currents i_{sd}, i_{sq}.

By comparing Fig. 4.13 a) and Fig. 4.26 a), thus the three-phase voltage waveforms of the two V/f controllers for the same frequency slope of 0.5 Hz/s, it can be found that

the open-loop controller produces a significantly higher voltage, despite the fact that the speed and acceleration levels are almost the same in both cases.

For instance, at $8s$ the speed of the open-loop controller (240 rpm) is only slightly higher than the speed of the closed-loop controller (218 rpm). However, the commanded voltage in the former case (61.3 V) is significantly higher than in the latter one (29.8 V).

By comparing Fig. 4.13 c) and Fig. 4.26 c), it can be observed that the lower commanded voltage in the closed-loop controller can be attributed to the lower d-axis voltage component.

What is also interesting to observe in Fig. 4.26 b) is that the startup currents in the closed-loop controller are very low (reaching a maximum rms value of around 4 A, which is far below the rated current of the PMSM). This is a significant improvement compared to the open-loop V/f control scheme, which suffers from overcurrents during the startup of the system.

Figure 4.26 d) demonstrates that the reason for the decreased current values in the closed-loop V/f controller is the decreased d-axis current component (reaching a maximum value of around 5.5 A). The decreased magnetizing current implies that the overexcitation experienced by the PMSM in this case is slighter.

It can be concluded that the voltage magnitude commanded by the open-loop controller is much higher, due to the increased d-axis voltage component. This component does not contribute much to the mechanical performance of the motor, but, instead, causes a high magnetizing current, which leads to increased losses.

On the other hand, the closed-loop controller provides a much more efficient startup performance, by keeping the d-axis voltage and current components low. This superior behaviour is facilitated by the higher accuracy of the closed-loop controller in the calculation of the voltage reference.

The voltages of the PMSM are presented in Fig. 4.27.

From Fig. 4.26 a) and Fig. 4.27 a), it can be found that the voltage drop in the transmission system at $5.9s$ is approximately 51% of the VSD voltage. Compared to the corresponding value for the open-loop controller (61%), the voltage drop in this case is lower, thanks to the lower startup current.

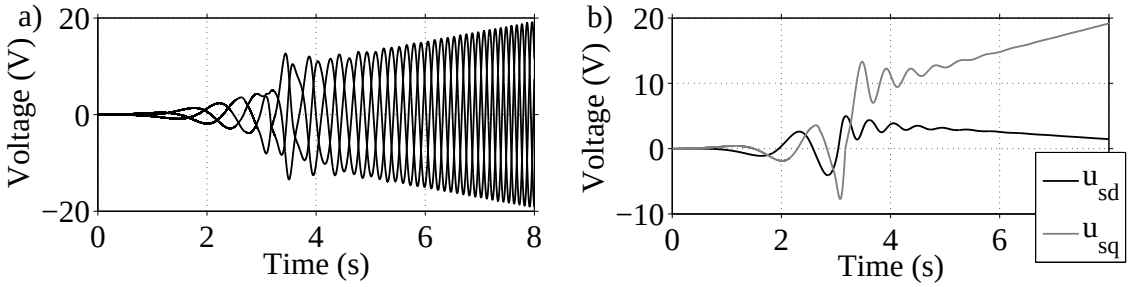

Figure 4.27: Waveforms for $df^*/dt = 0.5\ Hz/s$. a) Stator voltages u_{sa}, u_{sb}, u_{sc}. b) Stator voltages u_{sd}, u_{sq}.

Startup test with high frequency reference slope

For the next test, the frequency slope is increased to 5 Hz/s. The startup behaviour of the PMSM in this case is shown in Fig. 4.28.

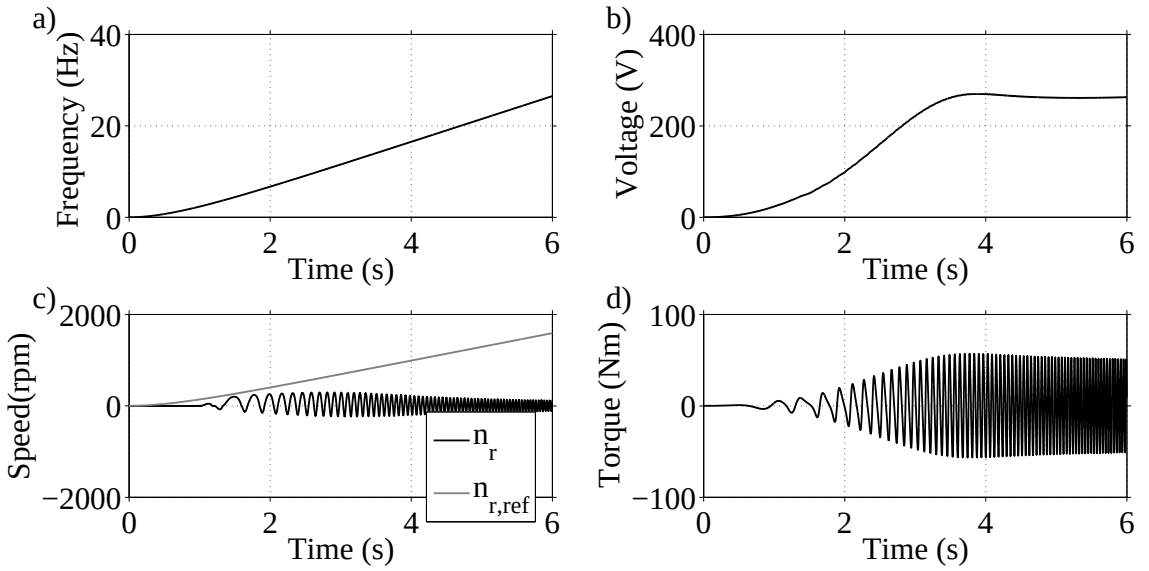

Figure 4.28: Waveforms for $df^*/dt = 5\ Hz/s$. a) Frequency reference f^* b) Voltage amplitude reference $\hat{u}_s^*$. c) Actual speed n_r and speed reference n_r^*. d) Electromagnetic torque T_e.

Figure 4.28 c) demonstrates that in this case the motor fails to accelerate and ends up vibrating, due to the occuring torque oscillations, which are shown in Fig. 4.28 d).

Similarly to the case of the open-loop V/f controller, too high frequency slopes, such as the one selected for this test, result in the inability of the PMSM to establish synchronism.

Selection of frequency reference slope

After performing startup simulations for several values of the frequency reference slope, it was found that the maximum value that results in successful acceleration of the PMSM

is approximately 4.3 Hz/s.

The maximum V/f ratio that corresponds to this slope has been found to be 12.34 V/Hz, which is almost equal to the corresponding ratio of the open-loop V/f controller (12.30 V/Hz). This means that the minimum size that can be achieved for the topside transformer is almost the same for both control schemes.

For the following tests, the value of the frequency slope has been set equal to 1.5 Hz/s, which is the same as the one selected for the open-loop controller in Section 4.1.1).

The maximum V/f ratio that corresponds to this slope has been found to be 16.50 V/Hz, which is slightly higher than the corresponding ratio of the open-loop controller (15.33 V/Hz).

The relatively large margin between the selected slope and the critical value of 4.3 Hz/s ensures that the rotor of the PMSM can follow the rotation of the supplied field without difficulty.

Moreover, the fact that the selected frequency slope is the same for both V/f control schemes is quite convenient, since it makes it possible to easily compare their performance.

4.2.2 Different initial rotor positions

For the selected frequency reference slope of 1.5 Hz/s, the startup performance of the PMSM is tested for several initial rotor positions. As in the case of the open-loop V/f controller, these tests are performed both for loaded and no-load operation of the PMSM.

Loaded startup test

Initially, the startup performance of the PMSM is investigated for several starting angles, when the motor is connected to the load which was introduced in Section 4.1.1.

The actual speed and the speed reference of the PMSM for different initial rotor positions are shown in Fig. 4.29. As in the case of the open-loop controller, different angles result in different speeds during the reverse rotation of the PMSM.

By performing startup tests for several starting positions, the maximum speed magnitude during the reverse rotation has been obtained as a function of the initial rotor angle and is shown in Fig. 4.30.

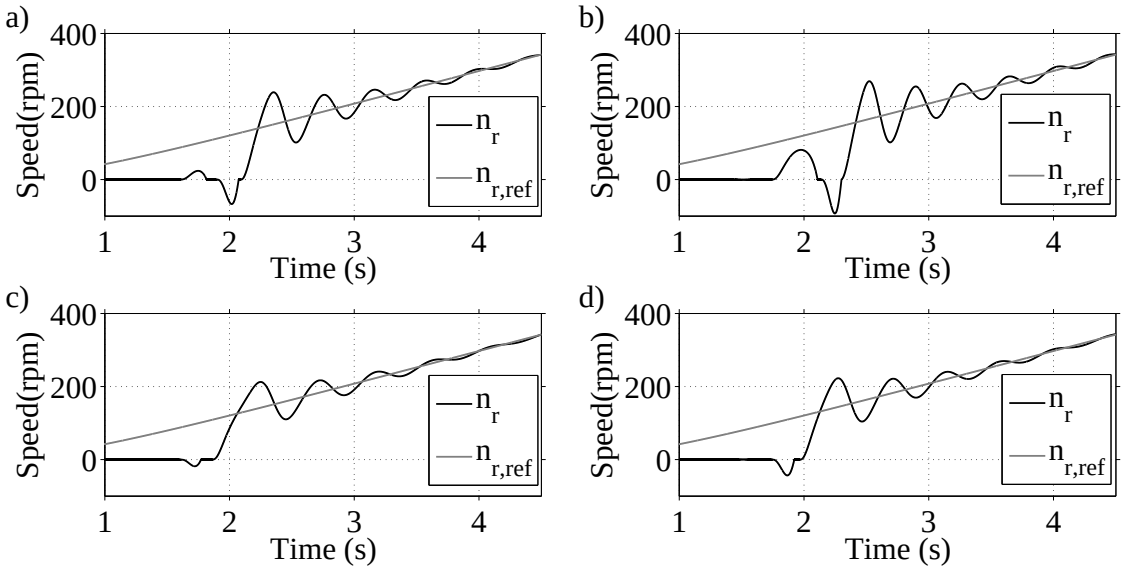

Figure 4.29: Actual speed n_r and speed reference n_r^* for loaded operation. a) $\phi_0 = 0^o$. b) $\phi_0 = 90^o$. c) $\phi_0 = 180^o$. d) $\phi_0 = 270^o$.

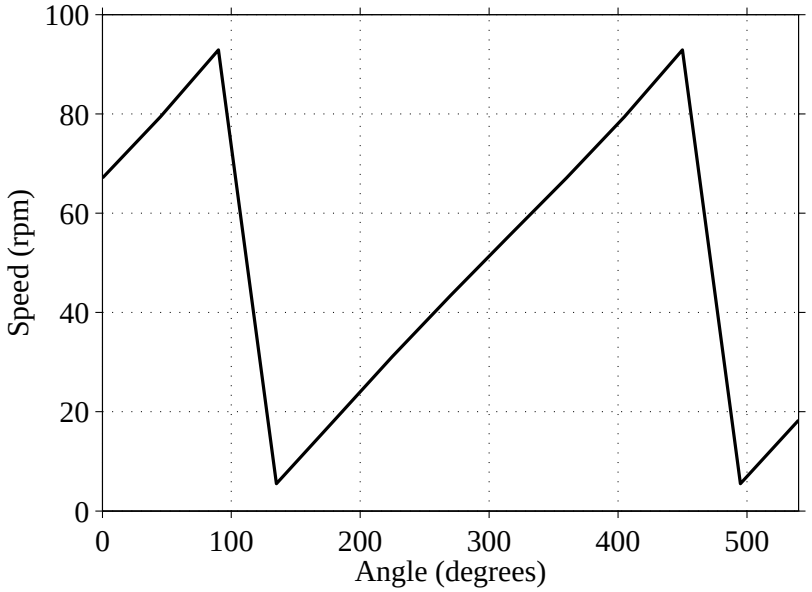

Figure 4.30: Maximum speed magnitude $|n_r|_{max}$ during reverse rotation as a function of the initial rotor angle ϕ_0 for loaded operation.

The maximum speed magnitude that the PMSM experiences during a reverse-rotation interval is approximately 92.9 rpm and occurs for $\phi_0 \simeq 90^o$. On the other hand, the smoothest startup occurs for $\phi_0 \simeq 135^o$. The maximum magnitude of the negative speed in this case is approximately 5.5 rpm.

By comparing these results with the results obtained for the open-loop V/f controller in

Section 4.1.3, it can be observed that the speed levels that are reached during reverse-rotation intervals are similar for the two controllers. However, the initial angles that correspond to the best and worst cases, in terms of startup smoothness, are different.

It has also been found that the best and worst angles, as well as the maximum and minimum negative speeds, vary for different frequency slopes of the closed-loop V/f controller.

To demonstrate this, the same test has been performed for a lower frequency slope value of 0.5 Hz/s. The highest negative speed in this case is almost 79.5 rpm and occurs for $\phi_0 \simeq 70^o$. Moreover, there is no reverse rotation for a range of initial angles (from 90^o to 160^o). This indicates that lower frequency slopes may result in smoother startups.

No-load startup test

For the following test, the starting behaviour of the system is investigated for several initial positions, when the PMSM is not loaded.

The actual speed and the speed reference for different starting angles are shown in Fig. 4.31.

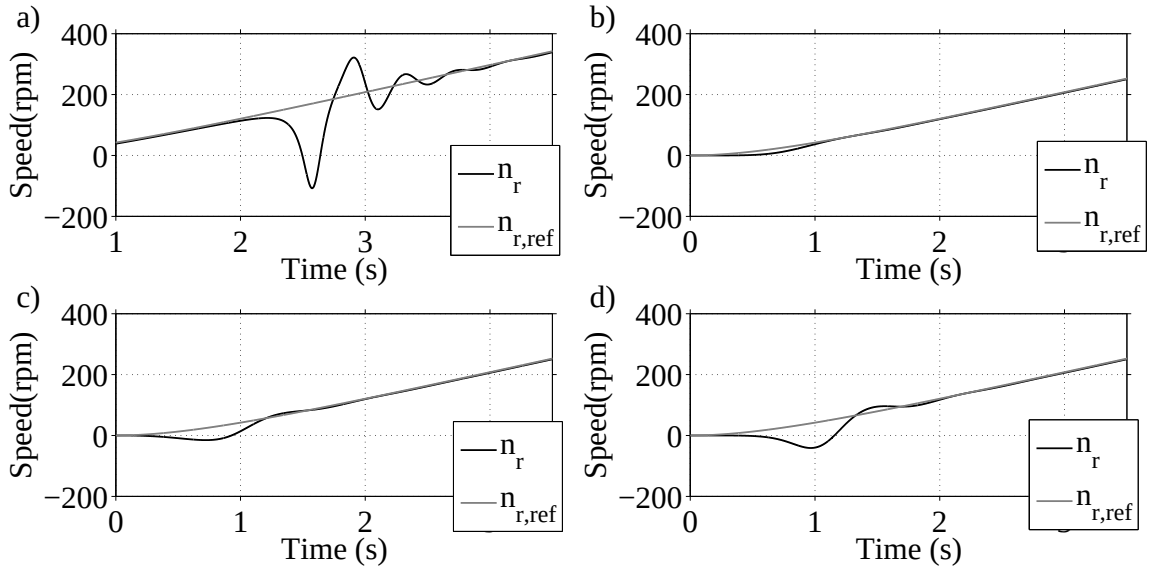

Figure 4.31: Actual speed n_r and speed reference n_r^* for no-load operation. a) $\phi_0 = 0^o$. b) $\phi_0 = 90^o$. c) $\phi_0 = 180^o$. d) $\phi_0 = 270^o$.

As in the case of the open-loop V/f controller, some initial rotor positions result in no negative speeds during no-load operation, which indicates that the startup process can be smoother for lighter loads.

It can also be observed that the starting angles that provide the smoothest acceleration during no-load operation may result in the least smooth startup during loaded operation. For instance, by comparing Fig. 4.29 b) and 4.31 b), it can be seen that $\phi_0 = 90^o$ yields no reverse rotation in the former case, but the highest negative speed in the latter case.

The obtained results demonstrate that the startup performance of the closed-loop V/f controller is heavily dependent on the load conditions of the system.

4.2.3 Response to load steps

The aim of the following tests is to evaluate the capability of the system to maintain its stability after being subjected to load disturbances, while operating under closed-loop V/f control.

Load step-up test

For this test, the closed-loop V/f controller accelerates the PMSM up to a relatively high speed. At some point of the simulation, a load step-up of 2 Nm is applied and the response of the system is shown in Fig. 4.32.

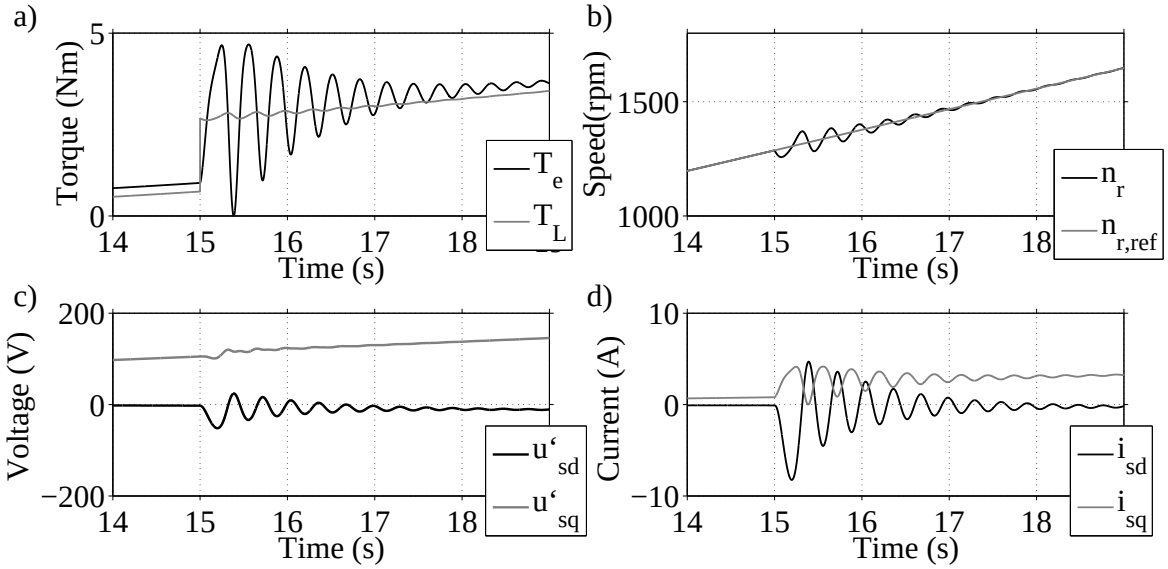

Figure 4.32: Response of the system to the load step-up. a) Electromagnetic torque T_e and load torque T_L. b) Actual speed n_r and speed reference n_r^*. c) Equivalent stator voltages u'_{sd}, u'_{sq}. d) Stator currents i_{sd}, i_{sq}.

The response of the system to the load increase is similar to the case of the open-loop controller. The electrical and mechanical oscillations that result from the load torque

increase are gradually damped and synchronism is maintained.

However, by comparing Fig. 4.22 and Fig. 4.32, it can observed that the response of the closed-loop controller to the load step-up is inferior compared to the response of the open-loop controller.

More specifically, the maximum peak-to-peak values of the speed and torque oscillations in the former case are approximately 113 rpm and 4.67 Nm respectively, while the corresponding values in the latter case are 55 rpm and 3.53 Nm respectively.

Moreover, the oscillations in the case of the open-loop controller are damped in less than $2s$, while the corresponding time for the closed-loop controller is around $3s$.

A basic difference between the closed-loop and the open-loop V/f controller is that the calculation of the voltage reference in the former one is affected by the stator currents, while in the latter one it is not.

The inferior response of the closed-loop controller to the sudden load increase indicates that the effect of the current oscillations on the calculated voltage reference increases the time needed to damp these oscillations.

Therefore, although the inclusion of the currents in the calculation of the voltage reference results in higher efficiency under normal conditions, it may have a negative effect on the response of the system to disturbances.

Moreover, as was noted in Section 3.4.6, the voltage reference calculation in the closed-loop V/f controller is based on equation (3.22), which has been derived for steady-state operation. This implies that the accuracy of the calculated voltage reference may be limited under transient conditions.

As was discussed in Section 3.4.3, the stabilizer which has been included in the closed-loop V/f controller has the mission of contributing to the damping of the electrical and mechanical oscillations that are caused by disturbances.

In order to verify that this function is performed successfully, the step-up test is repeated with the stabilizer deactivated. The response of the system in this case is shown in Fig. 4.33.

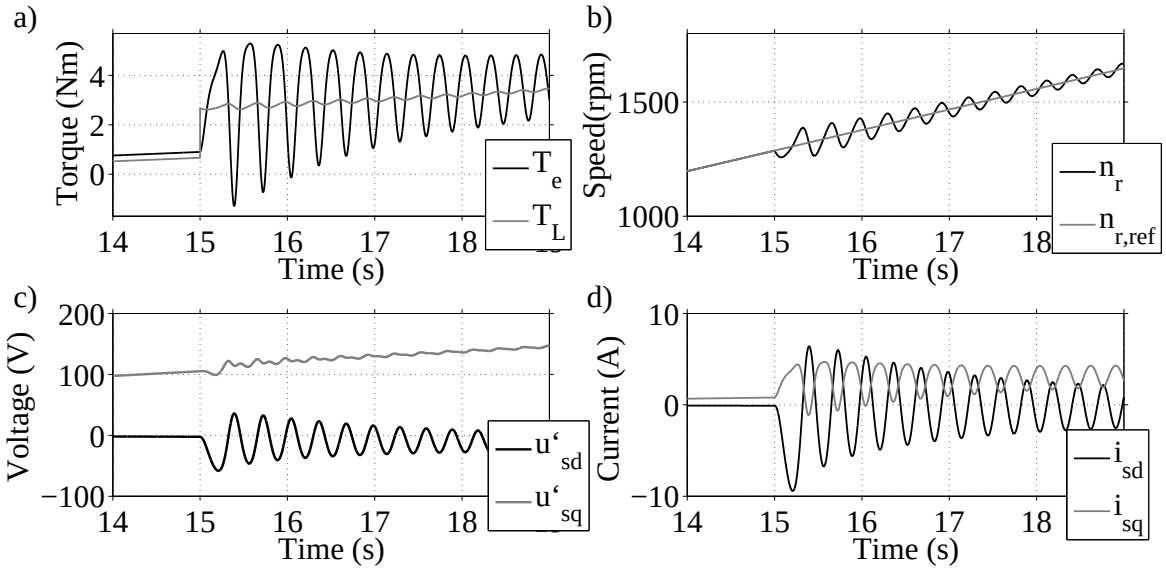

Figure 4.33: Response of the system to the load step-up with the stabilizer deactivated. a) Electromagnetic torque T_e and load torque T_L. b) Actual speed n_r and speed reference n_r^*. c) Equivalent stator voltages u'_{sd}, u'_{sq}. d) Stator currents i_{sd}, i_{sq}.

It can be observed that the maximum peak-to-peak values of the speed and torque oscillations in this case are higher than in the previous one (129 rpm and 6.57 Nm respectively) and that the time needed for the oscillations to fade out is significantly longer.

Therefore, it can be concluded that the presence of the stabilizer improves the response of the system to the load step-up, by contributing to the damping of the occuring oscillations.

Load step-down test

For this test, the mechanical load is stepped down by 1 Nm and the response of the system is shown in Fig. 4.34.

The maximum peak-to-peak values of the speed and torque oscillations are 19.5 rpm and 1.86 Nm respectively. As in the case of the load step-up test, these values are higher than those of the open-loop V/f controller (13.1 rpm and 1.83 Nm respectively).

By repeating the load step-down test with the stabilizer deactivated, the obtained results for the peak-to-peak torque and speed oscillations are 21.6 rpm and 1.91 Nm respectively, which are slightly higher than in the case where the stabilizer is activated.

Although the performance differences in the case of the load step-down test are small, the obtained results seem to be in agreement with those of the load step-up test.

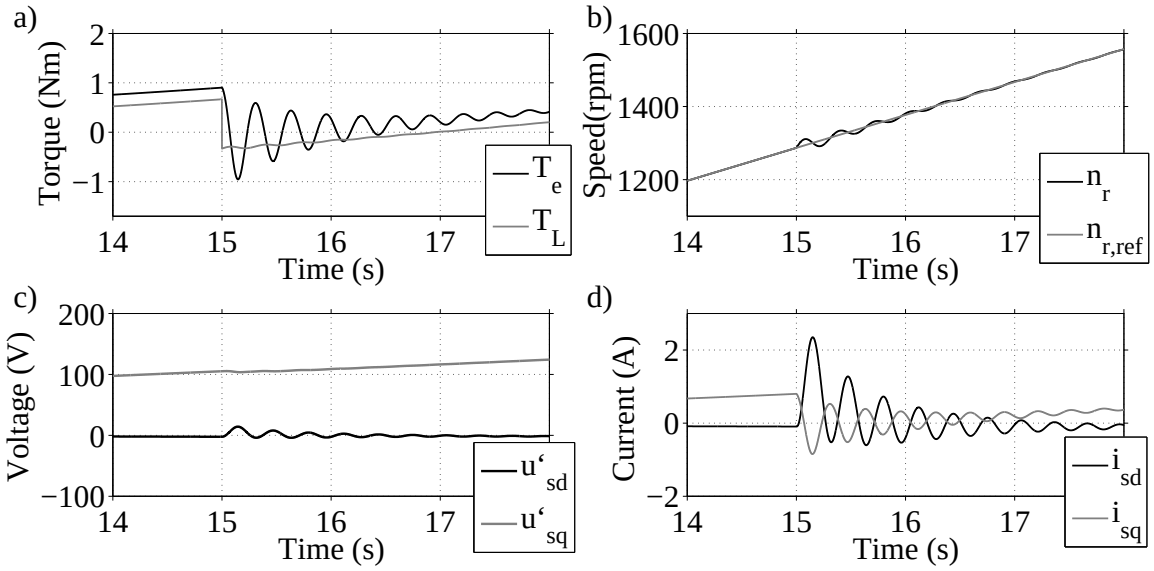

Figure 4.34: Response of the system to the load step-down. a) Electromagnetic torque T_e and load torque T_L. b) Actual speed n_r and speed reference n_r^*. c) Equivalent stator voltages u'_{sd}, u'_{sq}. d) Stator currents i_{sd}, i_{sq}.

These results indicate that the presence of the stabilizer in the closed-loop controller improves the response of the system to sudden load changes. Even with the stabilizer activated however, the response in the case of the closed-loop controller is inferior compared to that of the open-loop controller.

4.3 Vector control with position sensor

This section presents the simulation results for the implemented vector controller with the position sensor.

The behaviour of the system during and after the transition from V/f control to vector control is investigated. In order to find out how the system deals with load disturbances, the motor is subjected to load torque steps and the response of the system is examined.

Furthermore, it is demonstrated that smooth startup is possible, when the vector controller with the position sensor is used. By studying the startup behaviour of the system, it is verified that the rise time of the controlled currents is in agreement with the selected bandwidth of the current regulator.

4.3.1 Control transition

For this test, the closed-loop V/f controller is used for the startup of the PMSM. At $6s$ the control transition takes place, thus the V/f controller is dismissed and the vector controller takes over. The waveforms of the dq stator currents after the transition are shown in Fig. 4.35.

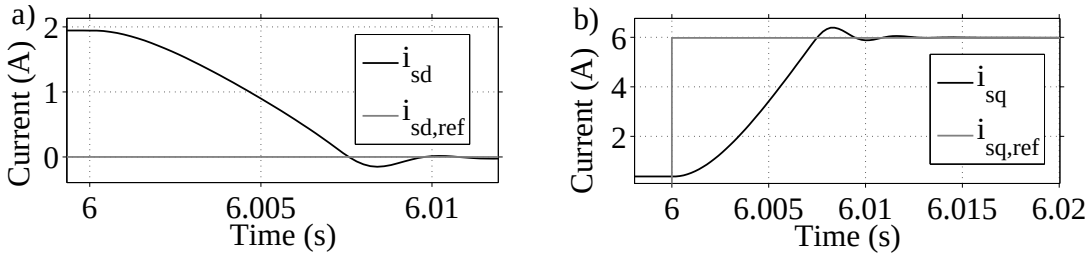

Figure 4.35: Stator currents and current references after the control transition. a) i_{sd} and i^*_{sd}. b) i_{sq} and i^*_{sq}.

It can be observed that the time needed by the dq currents to reach their reference values is slightly longer than 10 ms.

The d-axis current becomes zero, which allows the system to operate at its optimal efficiency. The q-axis current needed to produce the specified reference torque is approximately 5.98 A.

The amplitude of the overall current is equal to the magnitude of the q-axis current. This yields an rms value of 4.23 A, which is significantly lower than the rated current of the PMSM.

The mechanical response of the PMSM after the transition is shown in Fig. 4.36.

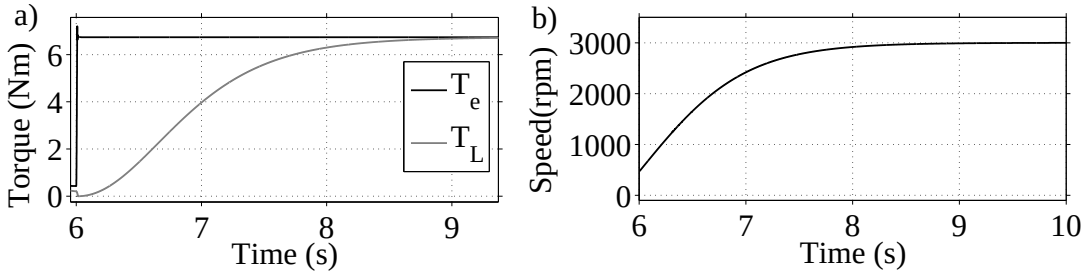

Figure 4.36: Mechanical response after the control transition. a) Electromagnetic torque T_e and load torque T_L. b) Rotor speed n_r.

The electromagnetic torque, being proportional to the q-axis stator current, reaches its target value (approximately 6.73 Nm) in slightly more than 10 ms. The torque reference

has been set equal to the value of the load torque that corresponds to the nominal speed of the PMSM (3000 rpm).

As can be seen in Fig. 4.36 a), since the load torque is speed-dependent, it changes much slower than the electromagnetic torque. The accelerating torque, thus the difference between the electromagnetic and the load torque, causes the motor speed to increase, as shown in Fig. 4.36 b).

The acceleration provided by the vector controller is considerably higher than the one of the V/f controller. It takes the latter one $6s$ to accelerate the motor from standstill up to 469 rpm, while the former one needs only $3s$ to bring the PMSM from this value up to its target speed (3000 rpm).

The effect of the control transition on the three-phase voltage and current waveforms of the VSD is shown in Fig. 4.37. It can be observed that the duration of the oscillations that result from the transition is slightly longer than 10 ms.

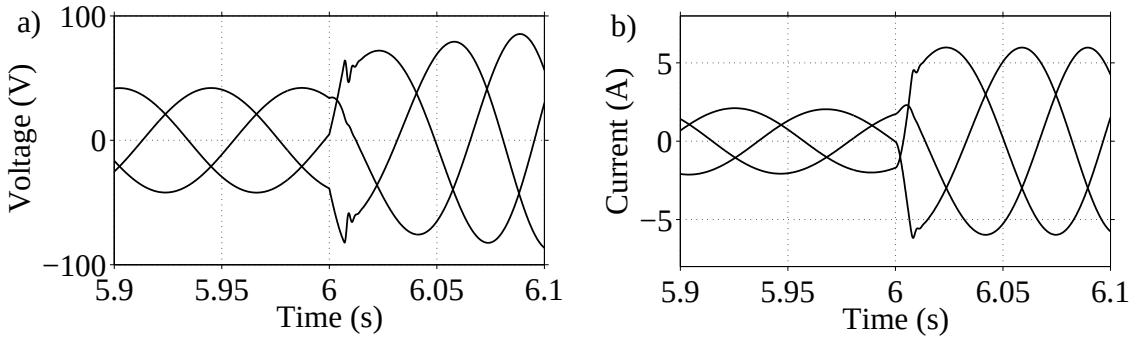

Figure 4.37: Voltage and current waveforms during the control transition. a) Equivalent stator voltages u'_{sa}, u'_{sb}, u'_{sc}. b) Stator currents i_{sa}, i_{sb}, i_{sc}.

The waveforms of the VSD and motor voltages both before and after the transition are shown in Fig. 4.38. The interval that corresponds to the V/f control is included for the sake of comparison.

The acceleration of the PMSM is achieved though an increase in the voltage provided by the VSD. As shown in Fig. 4.38 a), the main increase occurs in the magnitude of the q-axis voltage, thus the component that is primarily associated with the mechanical performance of the PMSM.

It can be found that the amplitude of the VSD voltage at steady state is approximately 268.8 V, which corresponds to a line-to-line rms value of around 329.2 V.

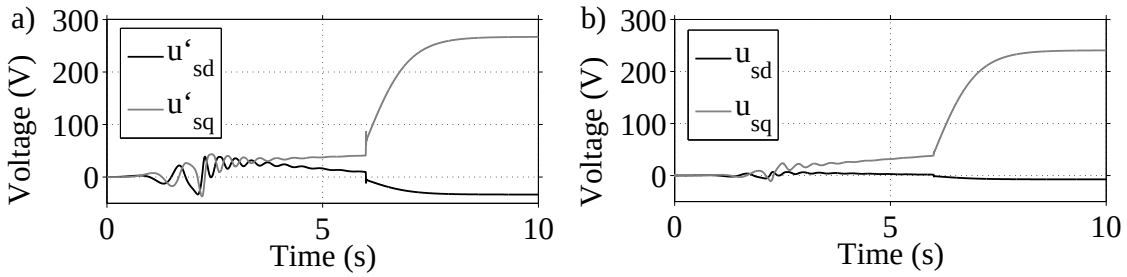

Figure 4.38: Voltage waveforms before and after the control transition. a) Equivalent stator voltages u'_{sd}, u'_{sq}. b) Stator voltages u_{sd}, u_{sq}.

Similarly, the amplitude of the motor voltage at steady state is approximately 240.5 V, (corresponding to a line-to-line rms value of around 294.6 V), which is roughly equal to the rated voltage of the PMSM (300 V).

The steady-state voltage drop in the transmission system is around 10.5% of the VSD voltage, which is close to the target value of 10%.

4.3.2 Response to load steps

This section investigates the response of the vector-controlled system to load variations. As in the case of the V/f controllers, a step-up and a step-down test are performed for this purpose.

Load step-up test

For this test, the closed-loop V/f controller is used for the startup of the PMSM. At $6s$ the control transition takes place and at $10s$ the load torque is stepped up by 4 Nm. The response of the system is shown in Fig. 4.39.

The d-axis and q-axis currents remain virtually unaffected by the load disturbance, thus they do not deviate from their target values. Since the electromagnetic torque is proportional to the q-axis current, it remains equal to its reference value as well.

The load torque on the other hand, consisting of the speed-dependent pump torque and the constant torque of 4 Nm, changes until a new torque balance is established.

After the load step is applied, the load torque becomes higher than the electromagnetic torque and the motor decelerates. As shown in Fig. 4.40, as the speed of the system decreases, the mechanical torque of the pump load decreases too.

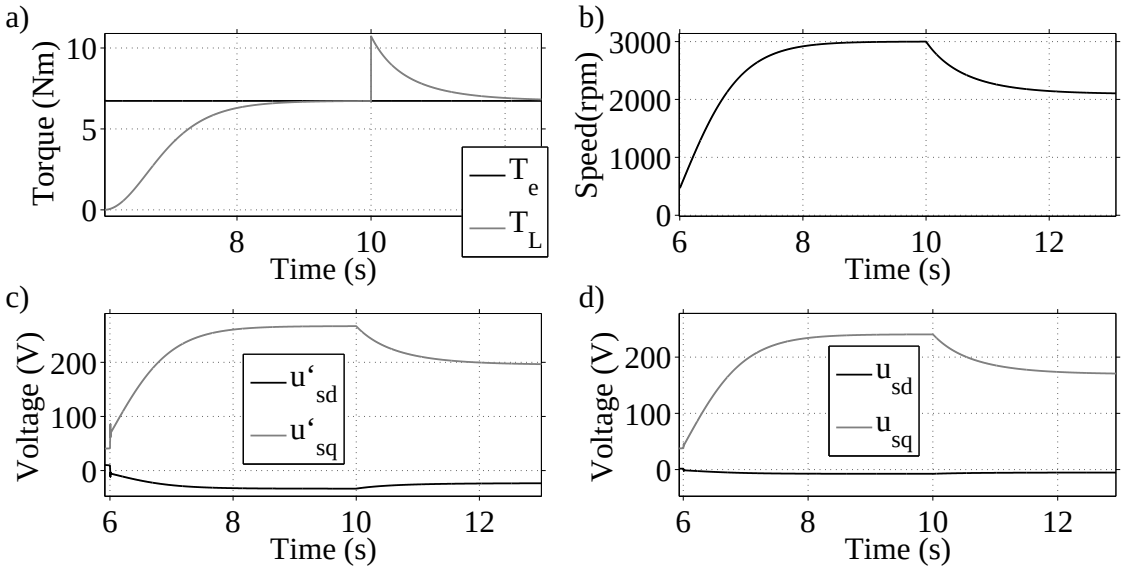

Figure 4.39: Response of the system to the load step-up. a) Electromagnetic torque T_e and load torque T_L. b) Rotor speed n_r. c) Equivalent stator voltages u'_{sd}, u'_{sq}. d) Stator voltages u_{sd}, u_{sq}.

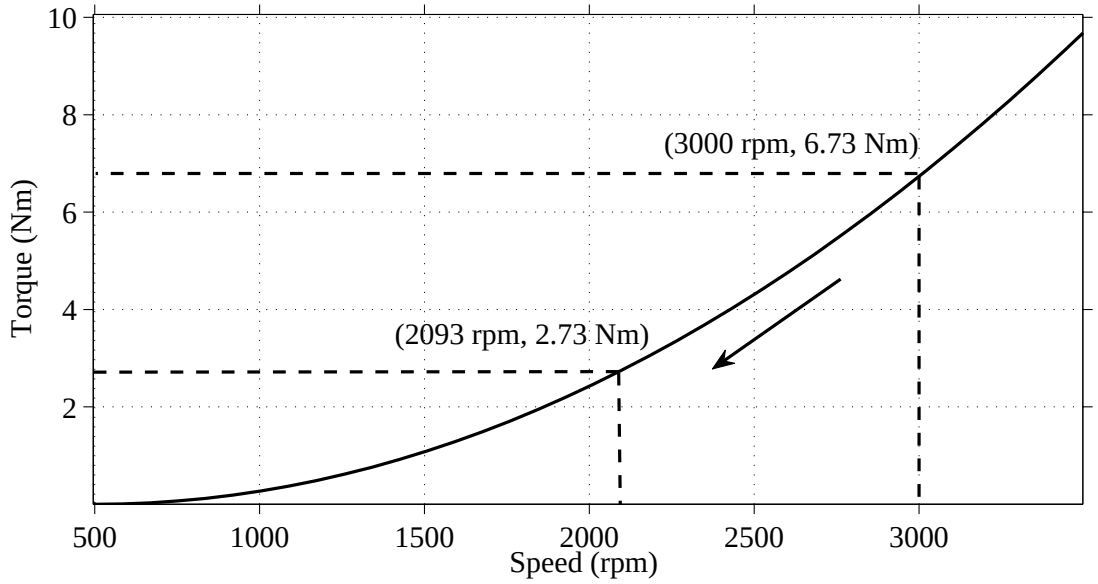

Figure 4.40: Operating points on the load characteristic before and after the load step-up.

A new steady-state point is reached when the total load torque becomes equal to the applied torque reference of 6.73 Nm. This occurs when the mechanical torque of the pump falls to 2.73 Nm, which corresponds to a speed of approximately 2093 rpm.

The speed decrease after the load step-up can be observed in Fig. 4.39 b). The deceleration of the PMSM is accompanied by a decrease in the VSD and motor voltages, as can

be seen in Fig. 4.39 c) and Fig. 4.39 d) respectively.

The obtained results demonstrate that the vector-controlled system responds well to the applied load increase. The electromagnetic torque and the currents of the motor are not affected and a new torque balance is achieved through a decrease in the operating speed.

The response of the vector controller to the applied load step-up is clearly better than the response of both V/f controllers. The presence of relatively large torque and speed oscillations in the latter cases demonstrates that the performance of V/f control schemes is more sensitive to load variations.

Load step-down test

In this case, the load torque is stepped down by 4 Nm at 10s and the response of the system is shown in Fig. 4.41.

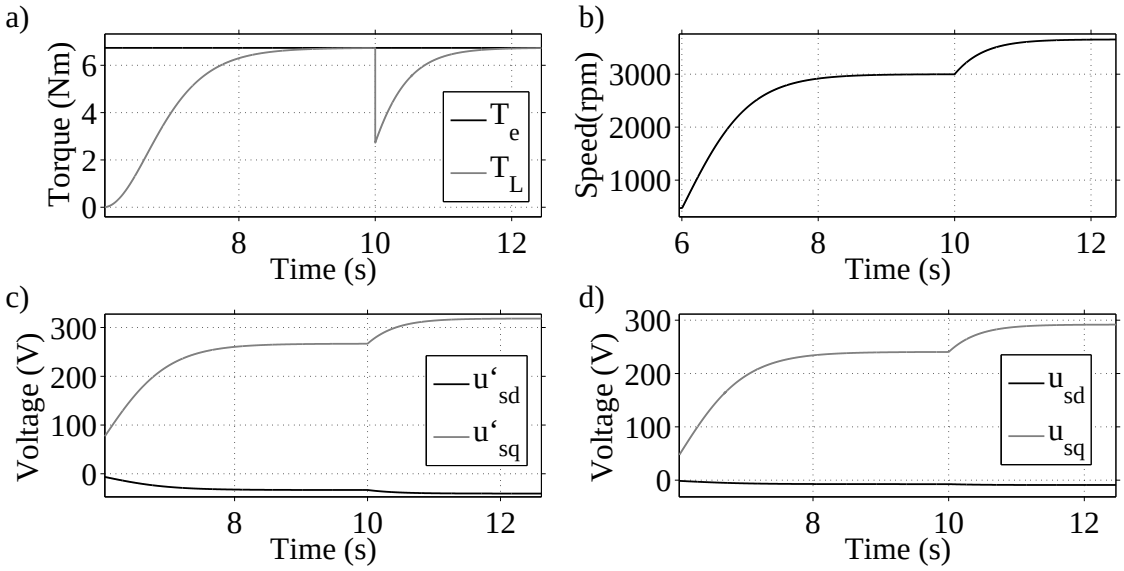

Figure 4.41: Response of the system to the load step-down. a) Electromagnetic torque T_e and load torque T_L. b) Rotor speed n_r. c) Equivalent stator voltages u'_{sd}, u'_{sq}. d) Stator voltages u_{sd}, u_{sq}.

As in the previous case, the load variation has no observable effect on the currents and the electromagnetic torque of the motor. The operating point on the load characteristic changes, according to Fig. 4.42 and a new steady state is reached. The speed of the PMSM at the new operating point is approximately 3655 rpm.

As can be seen in Fig. 4.41 c) and Fig. 4.41 d), the acceleration of the PMSM results in an increase in the VSD voltage and the motor voltage respectively. The amplitude of the

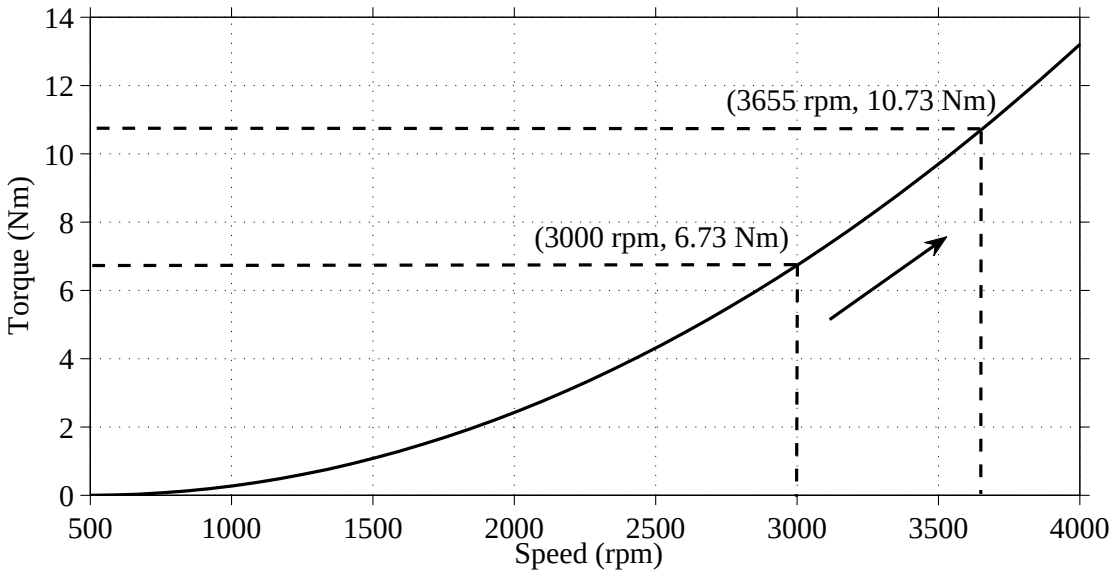

Figure 4.42: Operating points on the load characteristic before and after the load step-down.

new steady-state motor voltage is approximately 291.8 V (corresponding to a line-to-line rms value of 357.4 V, which exceeds the rated voltage of the PMSM).

Since no field-weakening algorithm has been included in this control scheme, it is not surprising that the motor experiences an overvoltage, when the rotor speed exceeds its rated value.

4.3.3 Startup performance

The following test demonstrates that the startup of the PMSM is possible, when a vector controller with a position sensor is used. Moreover, the proper operation of the controller is verified from the response of the controlled quantities during the startup process.

The mechanical response of the system is presented in Fig. 4.43.

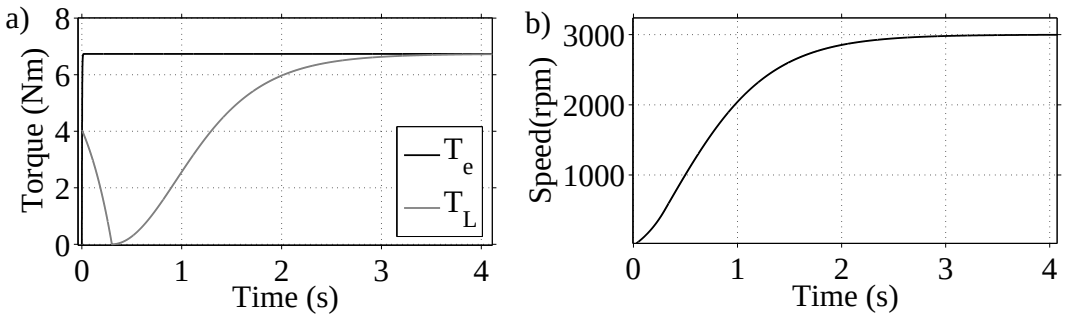

Figure 4.43: Mechanical performance during the startup test. a) Electromagnetic torque T_e and load torque T_L. b) Rotor speed n_r.

It can be seen from Fig. 4.43 b) that the vector controller manages to accelerate the PMSM from standstill up to its nominal speed of 3000 rpm within approximately $3s$.

The electromagnetic torque reaches its reference value of 6.73 Nm almost instantly, while the load torque, which is speed-dependent, needs almost $3s$ to reach this level, as shown in Fig. 4.43 a).

Figure 4.44 shows the voltages and currents at the output of the VSD.

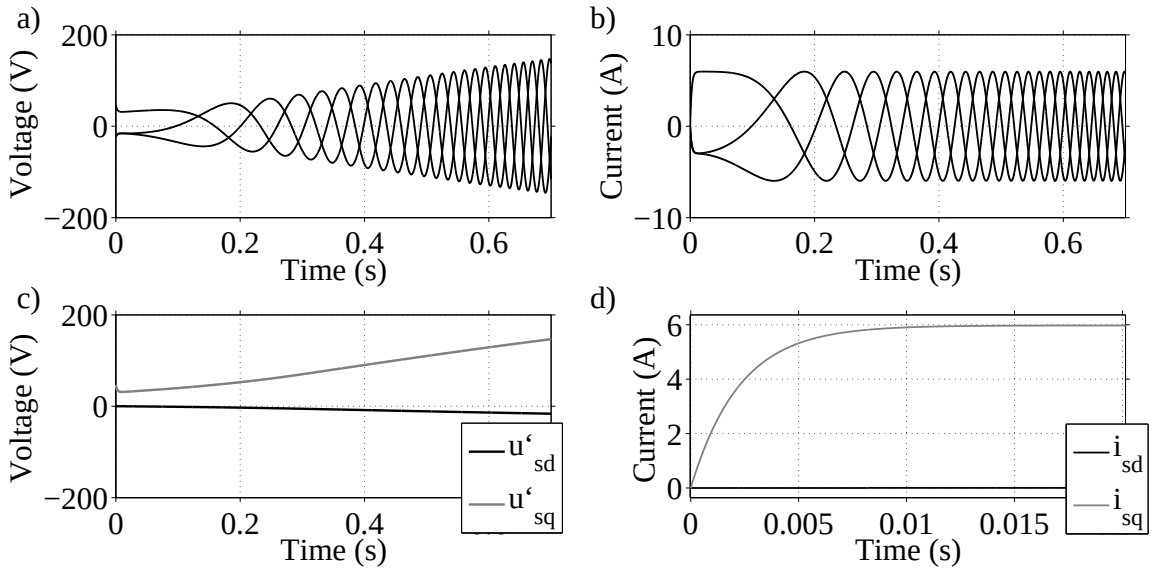

Figure 4.44: VSD voltage and current waveforms during the startup test. a) Equivalent stator voltages u'_{sa}, u'_{sb}, u'_{sc}. b) Stator currents i_{sa}, i_{sb}, i_{sc}. c) Equivalent stator voltages u'_{sd}, u'_{sq}. d) Stator currents i_{sd}, i_{sq}.

The rapid acceleration of the PMSM is reflected in the fast increase of the VSD voltage, as shown in Fig. 4.44 a). It can be observed in Fig. 4.44 c) that the dominant component of the supplied voltage is the q-axis component, which indicates high efficiency during the startup process.

Figure 4.44 b) demonstrates that no overcurrents appear during the startup procedure. This is expectable, since the d-axis and q-axis currents of the system are directly and accurately controlled by the implemented PI regulator.

The speed of the current regulation depends on the selected bandwidth of the current controller. This bandwidth corresponds to a frequency which is selected to be several times lower than the switching frequency of the VSD.

By considering a switching frequency of 7 kHz and by selecting the current controller to be 10 times slower than the VSD, a bandwidth of approximately 4398 rad/s is obtained.

Although this is the value normally used in this thesis, a lower bandwidth value of 439.8 rad/s has been selected for this test. The lower control speed in this case results in a higher rise time, which is easier to measure.

According to (3.39), the expected rise time of the controlled currents for the selected bandwidth is $4.99ms$. By measuring the rise time from Fig. 4.44 d), thus by measuring the time needed by the q-axis current to change from 10% to 90% of its final value, a time of $5.21ms$ is obtained. The proximity of the two values indicates that the current regulator operates properly.

The voltages of the PMSM are presented in Fig. 4.45.

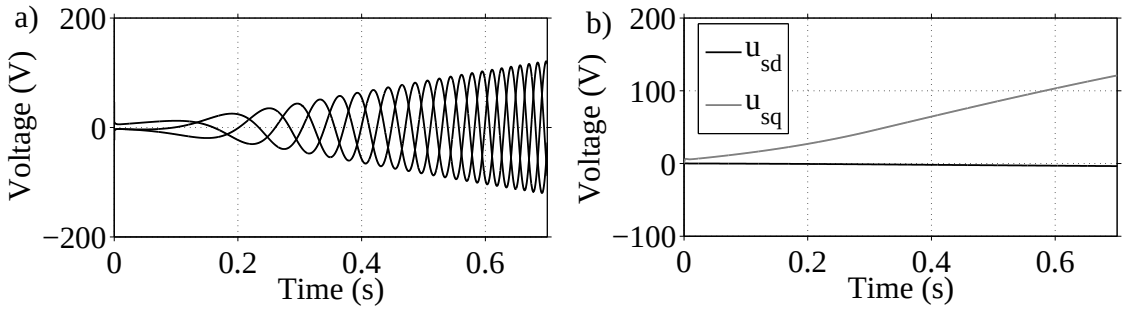

Figure 4.45: PMSM voltage waveforms during the startup test. a) Stator voltages u_{sa}, u_{sb}, u_{sc}. b) Stator voltages u_{sd}, u_{sq}.

From Fig. 4.44 a) and Fig. 4.45 a), it can be found that the voltage drop in the transmission system at $0.7s$ is approximately 17.8% of the VSD voltage. This value is very low, compared to the observed voltage drops in the performed V/f controlled startups, which can be attributed to the high efficiency of the vector-controlled startup.

4.4 Position-sensorless vector control

This section presents the simulation results for the implemented position-sensorless vector controller.

The performance of the controller during and after the control transition is tested and the response of the system to load disturbances is investigated. Moreover, the behaviour of the system during field-weakening operation is analyzed and the maximum achievable speed is determined.

4.4.1 Control transition

For this test, the closed-loop V/f controller is used for the startup of the PMSM and at $6s$ the control transition takes place. Figure 4.46 presents the performance of the position estimator after the transition.

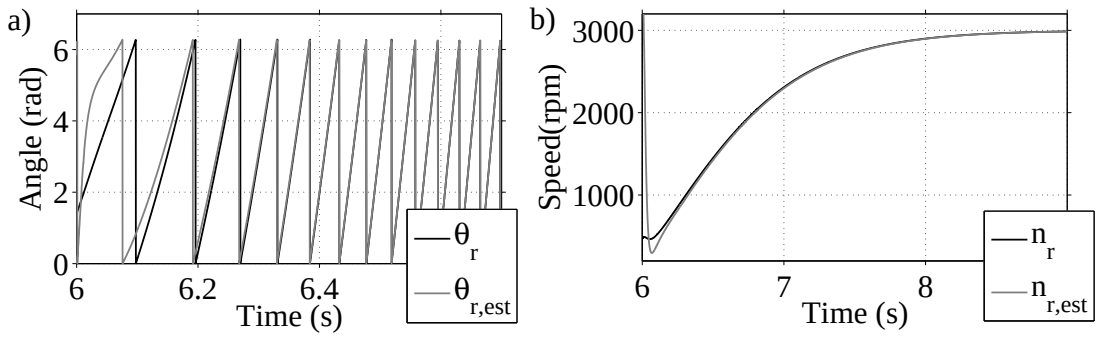

Figure 4.46: Performance of the the position estimator after the control transition. a) Actual position θ_r and estimated position $\theta_{r,est}$. b) Actual speed n_r and estimated speed $n_{r,est}$.

Figure 4.46 a) shows that an interval of around $0.4s$ needs to pass, before accurate position estimates can be produced. The estimated and the actual dq currents during this interval are shown in Fig 4.47.

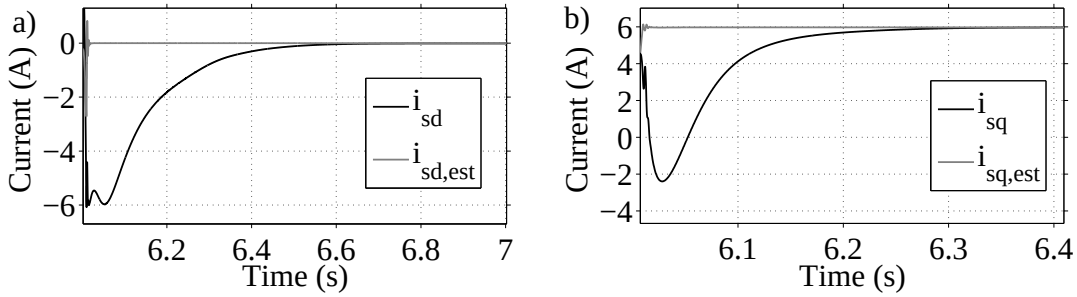

Figure 4.47: Actual and estimated currents after the control transition. a) i_{sd} and $i_{sd,est}$. b) i_{sq} and $i_{sq,est}$.

It can be observed that the initial inability of the controller to produce accurate position estimates temporarily affects the precision of the performed dq transformations. This results in significant errors between the actual and the estimated currents during the initial interval after the transition.

During this interval, the actual d-axis and q-axis currents become negative, which means that the motor temporarily experiences a reduction in its magnetic flux linkage and a negative electromagnetic torque. This is demonstrated in Fig. 4.48.

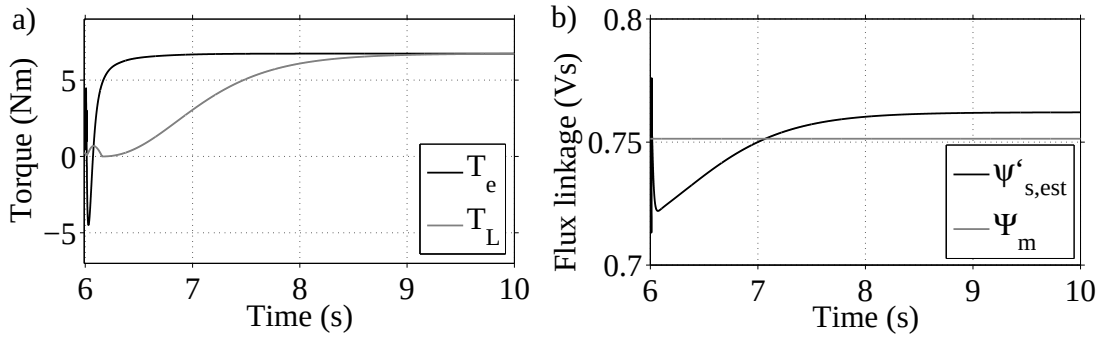

Figure 4.48: Performance of the system after the control transition. a) Electromagnetic torque T_e and load torque T_L. b) Estimated equivalent stator flux linkage $\psi'_{s,est}$ and flux linkage of the magnets Ψ_m.

Figure 4.48 b) shows that the steady-state value of the estimated flux linkage (0.762 Vs) is slightly higher than the flux linkage of the magnets (0.751 Vs). The small difference between the two values indicates high efficiency, which can be attributed to the zero value of the commanded d-axis current.

As can be seen in Fig. 4.46 b), the negative electromagnetic torque after the control transition results in a temporary speed reduction, after which the motor accelerates up to its target speed of 3000 rpm in less than 3s.

The behaviour of the current regulator after the control transition is shown in Fig. 4.49. It can be observed that the estimated d-axis and q-axis currents reach their reference values in less than 20 ms.

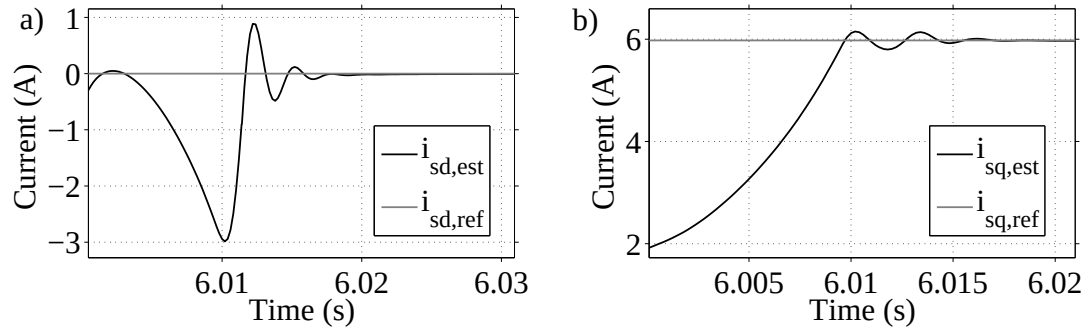

Figure 4.49: Estimated stator currents and current references after the control transition. a) $i_{sd,est}$ and i^*_{sd}. b) $i_{sq,est}$ and i^*_{sq}.

The effect of the control transition on the three-phase voltage waveforms of the VSD and the motor is shown in Fig. 4.50.

The duration of the voltage oscillations that result from the transition is approximately

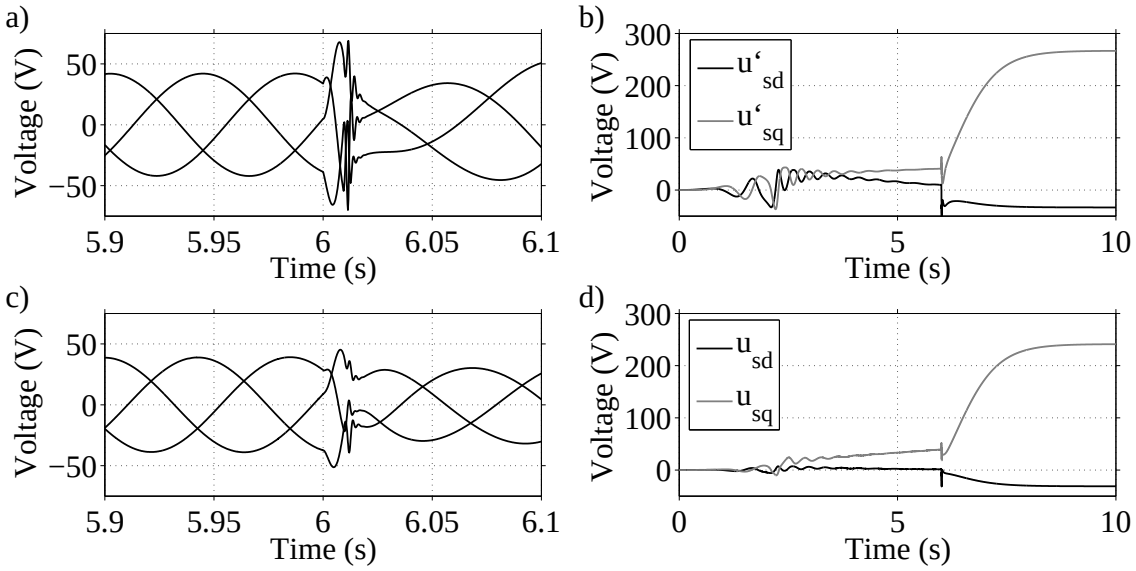

Figure 4.50: Voltage waveforms during, before and after the control transition. a) Equivalent stator voltages u'_{sa}, u'_{sb}, u'_{sc}. b) Equivalent stator voltages u'_{sd}, u'_{sq}. c) Stator voltages u_{sa}, u_{sb}, u_{sc}. d) Stator voltages u_{sd}, u_{sq}.

10 ms. By comparing Fig. 4.50 a) and Fig. 4.50 c), it can be observed that these oscillations are milder for the motor than for the VSD, thus it can be noticed that the transmission components act as a filter on the oscillations.

It can be found that the amplitude of the VSD voltage at steady state is approximately 268.7 V, which corresponds to a line-to-line rms value of around 329.1 V.

Similarly, the amplitude of the motor voltage at steady state is approximately 243.1 V, (corresponding to a line-to-line rms value of around 297.7 V), which is roughly equal to the rated voltage of the PMSM (300 V).

The steady-state voltage drop in the transmission system is around 9.5% of the VSD voltage, which is close to the target value of 10%.

4.4.2 Response to load steps

This section investigates the response of the position-sensorless controller to load variations. As usually, the PMSM is subjected to a load step-up and a load step-down test for this purpose.

Load step-up test

For this test, the closed-loop V/f controller is used for the startup of the PMSM. At $6s$ the control transition takes place and at $10s$ the load torque is stepped up by 4 Nm. The response of the system to the load increase is shown in Fig. 4.51.

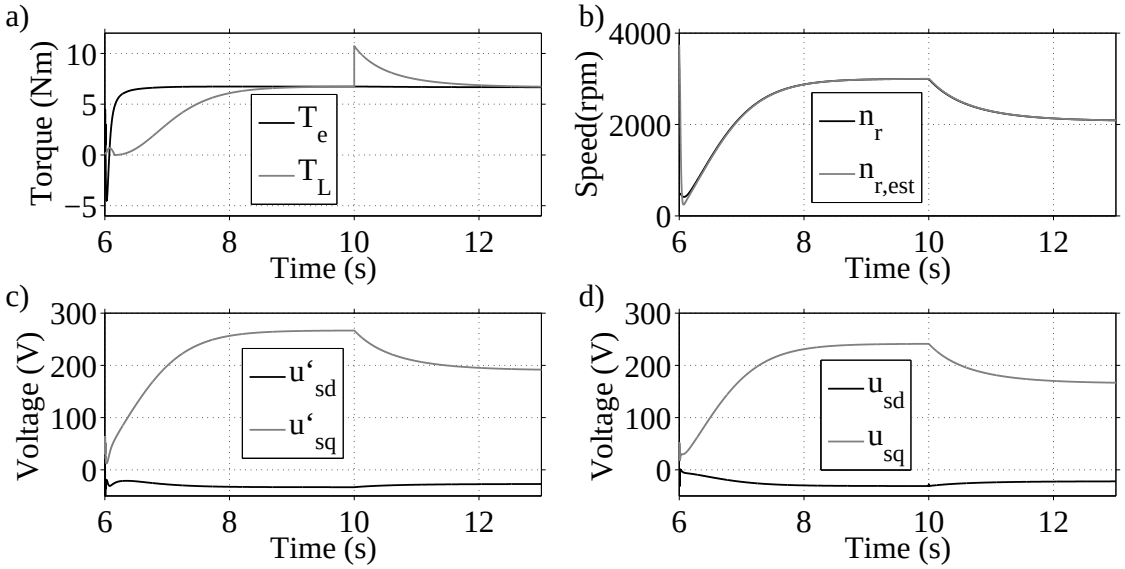

Figure 4.51: Response of the system to the load step-up. a) Electromagnetic torque T_e and load torque T_L. b) Actual speed n_r and estimated speed $n_{r,est}$. c) Equivalent stator voltages u'_{sd}, u'_{sq}. d) Stator voltages u_{sd}, u_{sq}.

The electromagnetic torque of the PMSM remains virtually unaffected, as shown in Fig. 4.51 a). Since the total load torque is temporarily higher than the produced electromagnetic torque, the motor decelerates, as can be seen in Fig. 4.51 b).

The speed decrease causes the pump torque to fall, until a new torque balance is reached at around $12.8s$. The pump torque at the new steady-state point is approximately 2.73 Nm and the corresponding speed is 2093 rpm.

Figures 4.51 c) and d) demonstrate that the q-axis voltages of the VSD and the PMSM respectively decrease as the motor decelerates. This is expectable, since the the q-axis voltage component is speed-dependent, according to (3.5).

The performance of the the position estimator after the load step-up is presented in Fig. 4.52. It can be observed that the effect of the sudden load increase on the accuracy of the position and speed estimation is insignificant.

The behaviour of the current regulator after the load step-up is shown in Fig. 4.53. The

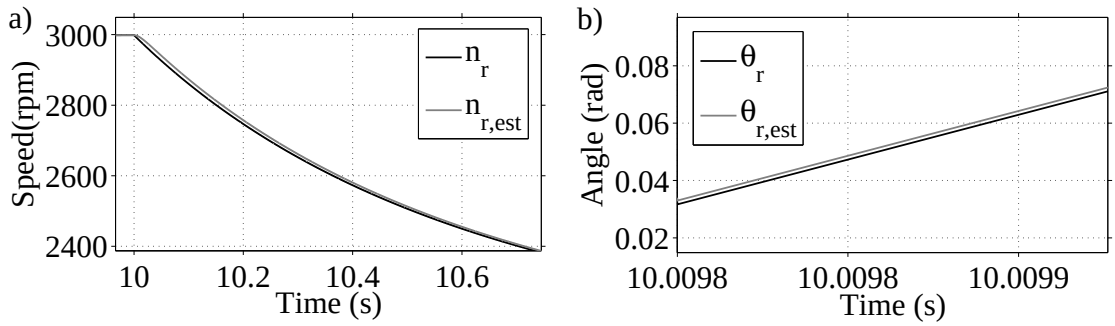

Figure 4.52: Performance of the the position estimator after the load step-up. a) Actual speed n_r and estimated speed $n_{r,est}$. b) Actual position θ_r and estimated position $\theta_{r,est}$.

deviation of the estimated d-axis current from its reference value is very small, while the q-axis current needs less than 40 ms to return to its target value.

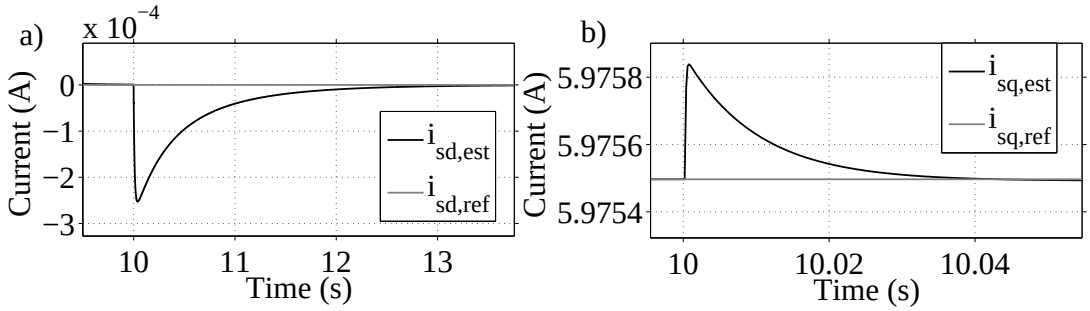

Figure 4.53: Estimated stator currents and current references after the load step-up. a) $i_{sd,est}$ and i^*_{sd}. b) $i_{sq,est}$ and i^*_{sq}.

It can be concluded that the response of the controller to the load increase is satisfactory. The precision of the position and speed estimation is not greatly affected and the current regulator limits the deviations of the controlled currents from their target values. A new torque balance is established within a few seconds through a decrease in the motor speed.

Load step-down test

In this case, the load torque is stepped down by 4 Nm at 10s and the response of the system is shown in Fig. 4.54.

As can be seen in Fig. 4.54 a), the effect of the load change on the electromagnetic torque is insignificant. The sudden load torque decrease causes the PMSM to accelerate, which results in an increase in the pump torque.

A new torque balance is established within 3s. The pump torque and the motor speed at the new operating point are approximately 10.73 Nm and 3679 rpm respectively.

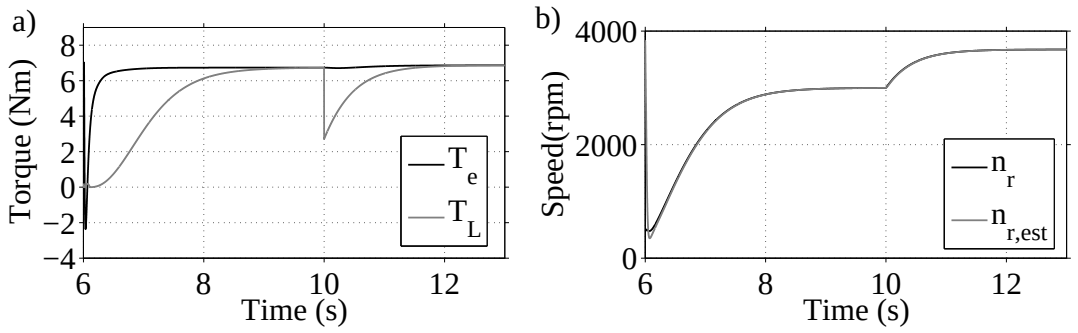

Figure 4.54: Mechanical response of the system to the load step-down. a) Electromagnetic torque T_e and load torque T_L. b) Actual speed n_r and estimated speed $n_{r,est}$.

The performance of the the position estimator after the load step-down is presented in Fig. 4.55. As in the case of the load step-up test, the effect of the load change on the estimation accuracy appears to be insignificant.

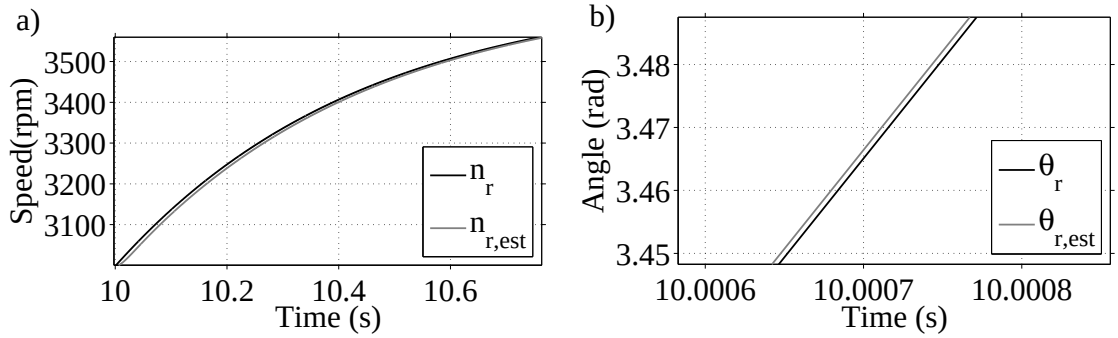

Figure 4.55: Performance of the the position estimator after the load step-down. a) Actual speed n_r and estimated speed $n_{r,est}$. b) Actual position θ_r and estimated position $\theta_{r,est}$.

Since the load decrease causes the rotor speed to exceed its rated value, the PMSM enters the field-weakening mode, as demonstrated in Fig. 4.56.

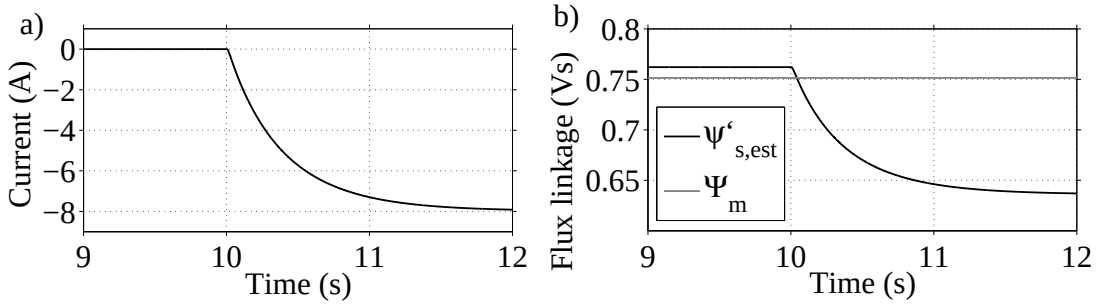

Figure 4.56: Field-weakening operation after the load step-down. a) Estimated d-axis current $i_{sd,est}$. b) Estimated equivalent stator flux linkage $\psi'_{s,est}$ and flux linkage of magnets Ψ_m.

After the field-weakening algorithm is activated, a negative magnetizing current is commanded. This causes the d-axis stator current to reach a negative value of approximately 7.95 A, which results in a decrease in the equivalent stator flux linkage. As shown in Fig. 4.56 b), the flux linkage falls from 0.762 Vs to 0.636 Vs.

The existence of the field-weakening algorithm allows the PMSM to operate above its rated speed, without experiencing voltage values that exceed its rated voltage. This is demonstrated in Fig. 4.57.

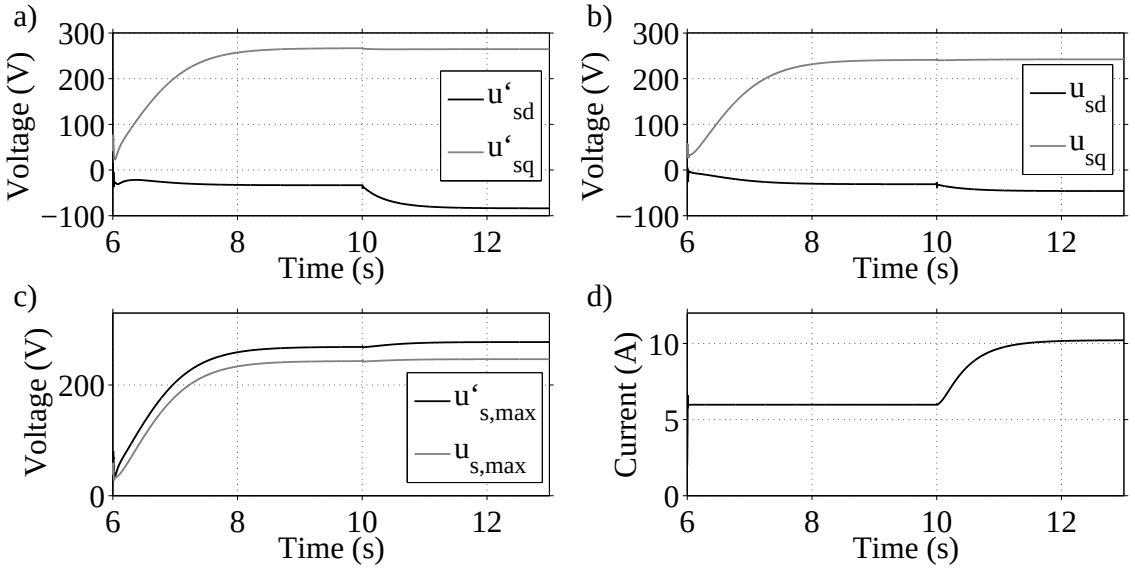

Figure 4.57: Voltage and current waveforms before and after the load step-down. a) Equivalent stator voltages u'_{sd}, u'_{sq}. b) Stator voltages u_{sd}, u_{sq}. c) Amplitude of the equivalent stator voltage $\hat{u'}_s$ and of the stator voltage $\hat{u}_s$. d) Amplitude $\hat{i}_s$ of the stator current.

A speed rise without field-weakening would normally be accompanied by an increase of the q-axis component of the motor voltage. In our case however, this component remains almost constant, while the magnitude of the d-axis voltage rises slightly, as a result of the increased magnitude of the magnetizing current.

Figure 4.57 c) demonstrates that, thanks to the field-weakening algorithm of the controller, the amplitude of the motor voltage remains close to its rated value after the load decrease.

However, the amplitude of the stator current increases substantially, as a result of the increase in the magnitude of the commanded magnetizing current. As shown in Fig. 4.57 d), the current amplitude rises from 5.98 A (which corresponds to an rms value of 4.23 A) to 9.97 A (which corresponds to an rms value of 7.05 A).

The current rise also causes an increase in the voltage drop in the transmission system, which, in turn, results in an increase in the voltage amplitude of the VSD.

As shown in Fig. 4.57 c), the amplitude of the supplied voltage rises from 268.8 V (which corresponds to a line-to-line rms value of 329.2 V) to 279.5 V (which corresponds to a line-to-line rms value of 342.3 V).

The voltage drop in the transmission system, which is approximately 9.5% of the VSD voltage before the load decrease, increases to 11% of the VSD voltage after the load step-down.

The resistive losses for the two operating points can be calculated, by considering the equivalent resistance R'_s of the system (which is approximately equal to 5.16 Ω for the selected cable length) and the current magnitude in the two cases.

It can be found that the resistive losses are approximately 276.7 W before the load step-down. When the new steady-state point is established, the resistive losses rise to almost 768.8 W. The loss increase in this case accounts for more than 177% of the losses during rated-speed operation, while the corresponding speed increase is only 23% of the rated speed.

The obtained results demonstrate that a speed increase by means of field-weakening comes at the cost of an increased voltage drop in the transmission components and significantly increased resistive losses. The field-weakening capability of the system is further investigated in Section 4.4.3.

4.4.3 Field-weakening performance

This section evaluates the possibility of extending the speed range of the PMSM, by applying the implemented field-weakening strategy. The maximum speed that can be reached is determined and the performance of the system at the corresponding operating point is investigated.

The field-weakening mode can be activated either through a decrease in the load torque (as in the case of the load step-down test in Section 4.4.2), or through an increase in the commanded torque.

In order to determine the highest speed that can be achieved for the considered pump load, it is sufficient to set a high reference torque, which forces the motor to operate at its rated current.

The current limiter that has been included in the vector controller prevents the stator current from exceeding its rated value. This sets the limit for the maximum electromagnetic torque that can be produced and, through the load characteristic, for the maximum speed that can be reached.

Determination of maximum achievable speed

For the following test, the closed-loop V/f controller is used for the startup of the PMSM and at $6s$ the position-sensorless vector controller is deployed.

The torque reference is initially set equal to the value of the load torque that corresponds to the nominal speed of the PMSM ($6.73\ Nm$). At $10s$, the commanded torque is doubled and the response of the system is presented in Fig. 4.58.

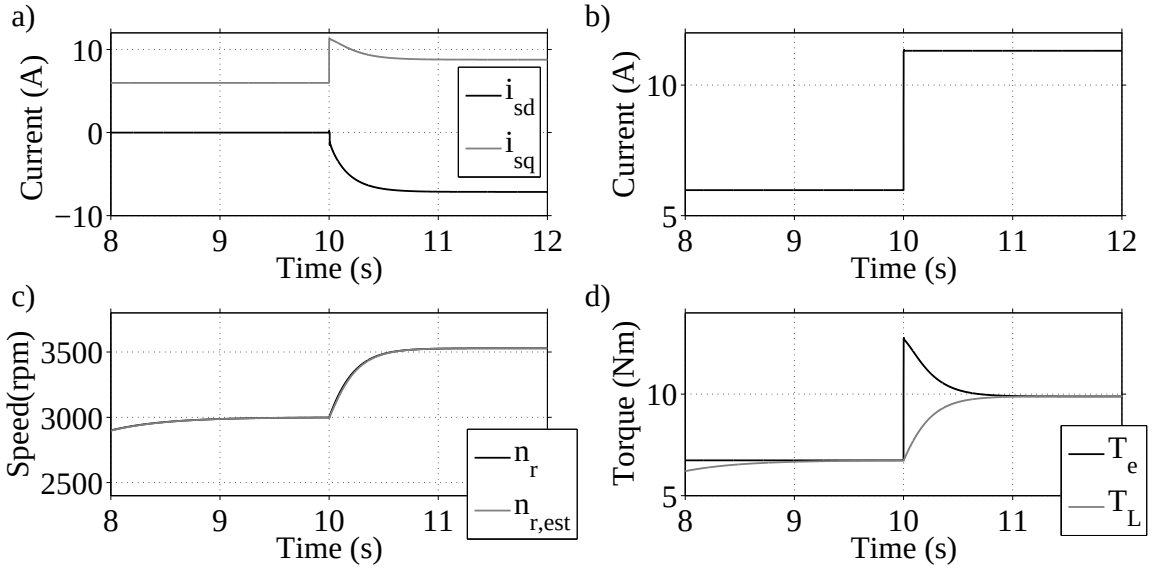

Figure 4.58: Response of the system to the torque reference step-up. a) Stator currents i_{sd}, i_{sq}. b) Amplitude $\hat{i}_s$ of the stator current. c) Actual speed n_r and estimated speed $n_{r,est}$. d) Electromagnetic torque T_e and load torque T_L.

The large increase in the ordered torque causes the q-axis current reference to exceed the rated current of the PMSM. The high commanded current results in the activation of the current limiter and the limitation of the q-axis current to the value of $11.31A$ (which corresponds to the rated rms current of 8 A).

As a result of the current limitation, the produced electromagnetic torque cannot be doubled, as commanded, but is limited to a value of approximately 12.75 Nm at 10s, as can be seen in Fig. 4.58 d).

The speed-dependent load torque cannot follow the almost instant increase of the electromagnetic torque. The resulting torque difference causes the PMSM to accelerate, as can be seen in Fig. 4.58 c).

Since the rotor speed exceeds its rated value, the field-weakening mode is entered, thus a negative d-axis current is ordered. As the speed increases, the magnitude of the commanded d-axis current increases as well (thus the magnetizing current becomes 'more negative'), as shown in Fig. 4.58 a).

As the magnitude of the d-axis reference current increases, the current limiter forces the commanded q-axis current to decrease, so that the overall stator current does not exceed its rated value. This causes the produced electromagnetic torque to decrease during the acceleration of the PMSM.

As shown in Fig. 4.58 d), as the rotor speed increases, the load torque increases too and a new torque balance is established at around 11.1s. The torque that the PMSM produces at the new steady-state point is approximately 9.88 Nm.

As can be seen in Fig. 4.58 c), the speed at the new operating point is approximately 3529 rpm. Apparently, this is the maximum speed that can be reached, without exceeding the rated current of the motor for the considered pump load.

The back-EMF amplitude, being proportional to the speed of the PMSM, also takes its maximum value at the new steady-state point. From Fig. 4.59 a), this value is found to be approximately 277.7 V (corresponding to a line-to-line rms voltage of 340.1 V).

As was discussed in Section 3.6.6, if the stator current is suddenly lost for some reason, the back-EMF of the PMSM will fall on the output of the VSD. In order to avoid damaging the drive, it is necessary for the inverter to be capable of handling the maximum back-EMF amplitude.

As can be seen in Fig. 4.59 a), the maximum back-EMF amplitude in the studied case (277.7 V) is lower than the voltage amplitude that the VSD output normally experiences during maximum-speed operation (approximately 291.7 V). Therefore, handling

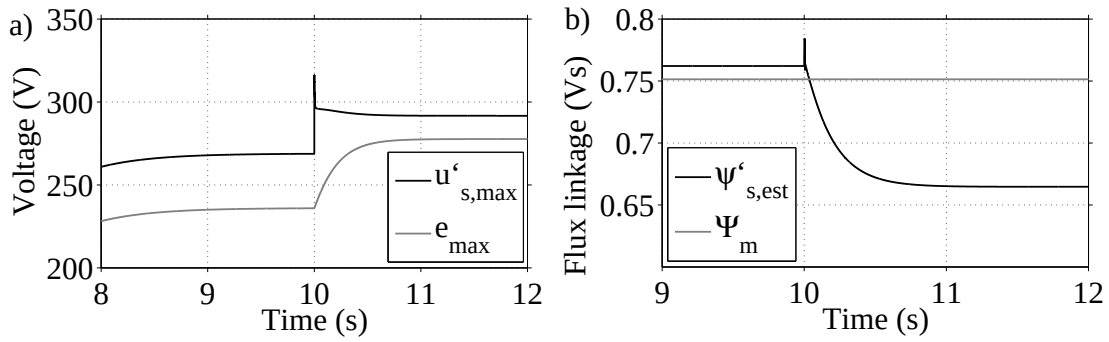

Figure 4.59: Response of the system to the torque reference step-up. a) Amplitude of the equivalent stator voltage $\hat{u'}_s$ and of the back-EMF $\hat{e}$. b) Estimated equivalent stator flux linkage $\psi'_{s,est}$ and flux linkage of magnets Ψ_m.

this back-EMF should be no problem for the inverter.

Figure 4.59 b) shows that the amplitude of the estimated flux linkage $\psi'_{s,est}$ falls to approximately 0.665 Vs after the torque reference step-up. Apparently, this is the minimum value that can be reached for the considered load.

Figure 4.58 b) demonstrates that the step-up of the torque reference at $10s$ results in an increase in the stator current magnitude up to the value of 11.31 A (which corresponds to the rated rms current of 8 A).

Although the composition of the stator current changes as the motor accelerates (as shown in Fig. 4.58 a)), its amplitude after the torque increase remains constant and equal to its maximum acceptable value.

Efficiency calculations and comparisons

The implemented field-weakening algorithm allows the motor to operate at high speeds, without experiencing any overvoltages.

The performed torque reference step-up test demonstrated that a maximum speed of approximately 3529 rpm can be reached and a maximum steady-state torque of around 9.88 Nm can be produced by the PMSM during field-weakening operation.

During the load step-down test in Section 4.4.2, it was demonstrated that even higher speeds can be reached, when lighter loads are considered. The speed that was obtained during that test was around 3679 rpm.

However, for the current analysis, the pump load that was introduced in Section 4.1.1

is considered. In this case, field-weakening can extend the speed range of the PMSM by approximately 17.6% and can result in a 46.8% increase in the produced electromagnetic torque.

It is important to note, however, that the aforementioned enhancement in the mechanical performance of the motor is achieved through a 89.2% increase in the magnitude of the stator current. The increased current results in higher losses and a larger voltage drop in the transmission system.

The total resistive losses are approximately 276.7 W, when the PMSM operates at its rated speed, while they rise to almost 990.2 W during maximum-speed operation. This corresponds to a loss increase of more than 257%.

These loss calculations have been performed by considering the same equivalent resistance R'_s for both operating points. However, by taking into account that the increased losses cause higher temperatures, which in turn increase the resistances of the motor and the transmission components, the loss increase should be expected to be even greater.

The overall efficiency of the system in the cases of rated-speed operation and maximum-speed operation can be obtained, by calculating the input and output power values for both operating points. The system considered in these calculations includes the motor and the transmission components.

The input power of the system can be calculated from the voltage and current waveforms at the output of the VSD, according to (3.25). The power factor in this relation is obtained from the phase difference between the voltage and current.

On the other hand, the output power of the system, thus the mechanical power of the PMSM, can be readily calculated as the product of the load torque and the mechanical speed of the motor.

In the case of rated-speed operation, the VSD voltage and current amplitudes are 268.8 V and 5.98 A respectively and the power factor angle is approximately 5.6^o. This yields an input power value of 2399 W. The output power, calculated for a load torque of 6.73 Nm and a speed of 314.2 rad/s (corresponding to 3000 rpm), is approximately equal to 2114 W.

By subtracting the output from the input power, the total power losses in the case of

rated-speed operation are found to be 285 W. This value is in good agreement with the total resistive losses calculated earlier (276.7 W). The efficiency of the system in this case is almost 88.1%.

In the case of maximum-speed operation, the VSD voltage and current amplitudes are 291.7 V and 11.31 A respectively and the power factor angle is roughly 20.1^o. The resulting input power is almost 4647 W. The output power, calculated for a load torque of 9.88 Nm and a speed of 369.6 rad/s (corresponding to 3529 rpm), is approximately equal to 3652 W.

The total power losses in the case of maximum-speed operation can be found to be 995 W. Once again, this value is very close to the resistive losses calculated earlier (990.2 W). The efficiency of the system in this case falls to almost 78.5%.

Apart from the decreased efficiency during field-weakening operation, the increased current magnitude also causes a larger voltage drop in the transmission system. While the drop is around 9.5% of the VSD voltage during rated-speed operation, it rises up to approximately 14.7% during maximum-speed operation.

Chapter 5

Experimental results

This chapter presents the obtained experimental results and describes the laboratory topology on which the presented measurements have been performed.

Initially, the small-scale lab model of the studied system is described and the control and monitoring topologies are introduced.

The performance of the V/f controller of the VSD is then investigated both during the startup of the system and during steady-state operation of the PMSM. In both cases, the measurements are performed for two different loads.

Finally, the behaviour of the system under position-sensorless vector control is tested after the transition from V/f control, after sudden variations of the load torque and after changes of the torque reference. The performance of the field-weakening algorithm of the vector controller is also investigated during operation at relatively high speeds.

5.1 Experimental setup

This section describes the experimental setup on which the presented measurements have been performed. As shown in Fig. 5.1, this setup includes the model of the investigated system, the monitoring topology and the control system of the drive.

The setup of the small-scale system model and the implementation of the VSD control through the drive software have not been parts of this thesis. On the other hand, the preparation of the data acquisition code in LabVIEW and the configuration of the CompactRIO device have been in the scope of this work.

The implemented data acquisition system, consisting of the CompactRIO device and the

LabVIEW code, has been used to monitor the electrical quantities of the PMSM. On the other hand, in order to measure the VSD quantities and to obtain the estimated speed and torque waveforms of the PMSM, the monitoring capabilities of the drive have been utilized.

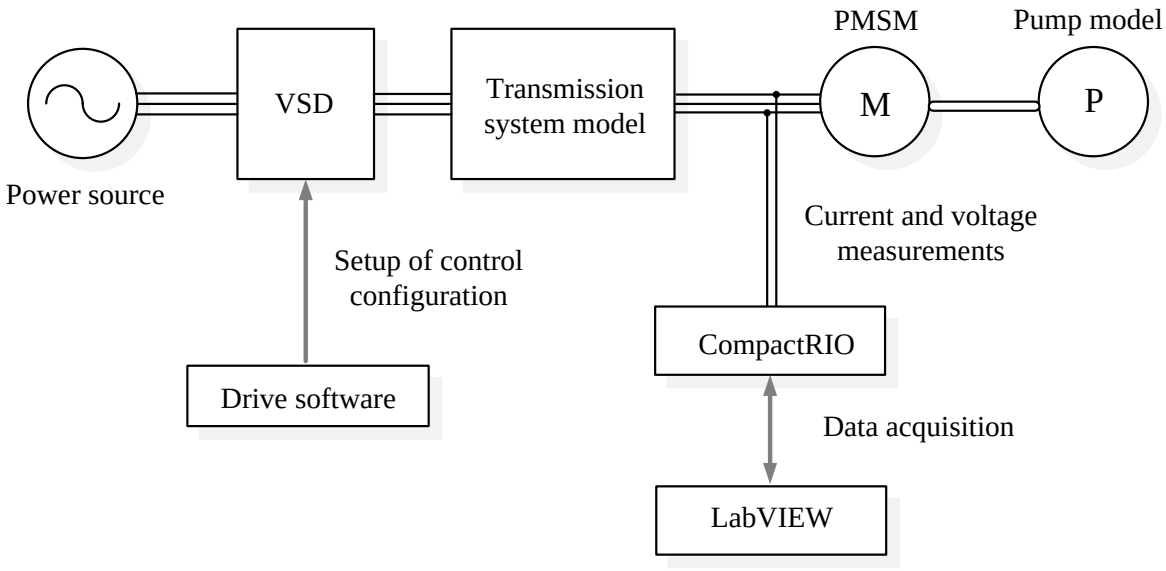

Figure 5.1: Layout of the experimental setup, consisting of the system model, the monitoring topology and the control system.

5.1.1 Small-scale laboratory model

The considered laboratory system is a small-scale model of the offshore system that is investigated in this thesis. The setup of this model has not been conducted during this thesis, but was implemented as part of a previous work [1].

As shown in Fig. 5.1, the laboratory model includes a power source, a VSD, a model of the transmission system, a PMSM and a model of the multiphase pump.

As shown in Fig. 5.2, the model of the transmission system is composed of two 1:1 transformers and a cable simulator, all connected in series with each other. The cable simulator consists of an electric circuit in which the cable parameters are distributed over a number of series-connected π-equivalent elements.

The pump model represents the mechanical load of the system and consists of a permanent magnet generator, a flywheel, a break-away torque device and three identical adjustable resistors, as demonstrated in Fig. 5.3.

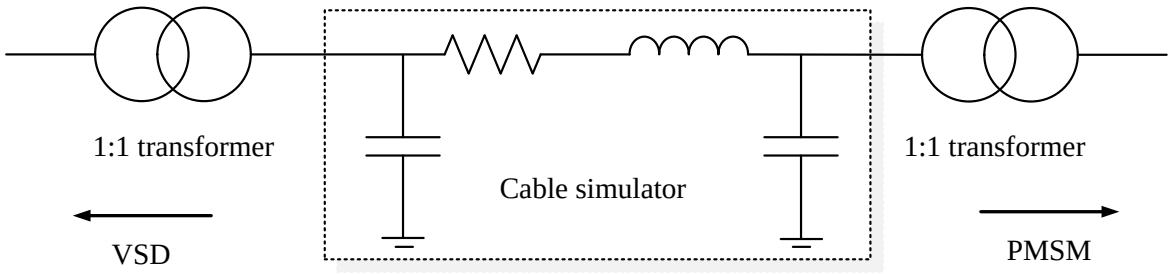

Figure 5.2: Layout of the transmission system model, consisting of two 1:1 transformers and a cable simulator.

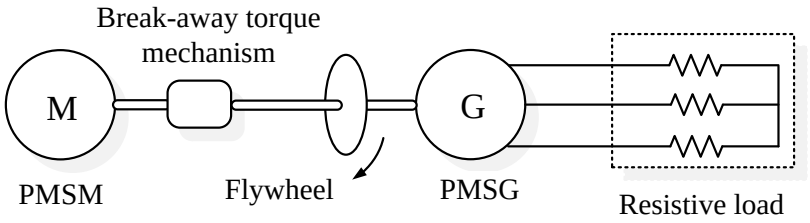

Figure 5.3: PMSM and pump model assembly, consisting of a PMSG, a flywheel, a break-away torque mechanism and a resistive load.

The generator is mechanically coupled to the motor, while the flywheel and the break-away torque mechanism are attached on the common shaft of the assembly. The mission of the flywheel is to increase the inertia of the system, while the aim of the break-away torque device is to simulate the break-away torque of the actual multiphase pump.

The resistors are connected to the stator windings of the permanent magnet generator as a symmetrical three-phase electrical load.

When the motor-generator assembly rotates, a voltage is induced at the stator windings of the generator and a current flows through the resistive load. This current results in an electromagnetic torque that opposes the torque produced by the PMSM and, therefore, acts as a load torque for the motor.

By assuming almost 100% efficiency for the PMSG, thus by considering that its electric power output $p_{e,gen}$ is almost equal to its mechanical power input p_m, the load torque of the motor can be obtained from

$$p_m \simeq p_{e,gen} \Rightarrow T_L \frac{\omega_r}{n_p} \simeq \frac{3}{2} \frac{\hat{u}_{s,gen}^2}{R_{gen}} \simeq \frac{3}{2} \frac{\omega_r^2 \hat{\psi}_{s,gen}^2}{R_{gen}} \Rightarrow T_L \simeq \frac{3}{2} \frac{n_p \hat{\psi}_{s,gen}^2}{R_{gen}} \omega_r \tag{5.1}$$

where R_{gen} is the per-phase load resistance and $\hat{u}_{s,gen}$ and $\hat{\psi}_{s,gen}$ are the amplitudes of the stator voltage and the stator flux linkage of the generator respectively.

When the speed of the PMSM does not exceed its rated value, thus when the motor does not operate in field-weakening mode, the amplitude $\hat{\psi}_{s,gen}$ of the stator flux linkage can be considered to be speed-independent. Therefore, according to (5.1), the load torque can be considered to be approximately proportional to the speed of the motor.

Since (5.1) is based on (3.14), it assumes that the stator flux linkage of the generator is constant and that the voltage drop in its stator resistance is negligible. Therefore, the derived load torque expression is approximate.

5.1.2 Control and monitoring system

The PMSM of the laboratory model is controlled by the VSD through the transmission system. The VSD control is set up by dedicated drive software, which runs on a computer that is directly connected to the VSD.

The drive software allows the PMSM to be controlled in different ways and offers several monitoring possibilities. The setup of the V/f control and vector control configurations in this software has not been part of this thesis.

Two current flukes and two voltage probes were used during the performed experiments, in order to obtain measurements of two motor currents and two motor voltages respectively.

In order to collect and store the measured data, the measuring units were connected to the analog inputs of a NI CompactRIO device, which, in turn, was connected to a computer. The configuration of the CompactRio device and the development of the data acquisition code in LabVIEW has been performed in the framework of this thesis.

The developed LabVIEW code acquires the measurements from the CompactRIO input modules at a sufficient rate and stores them in the memory of the device. It also performs real-time monitoring, thus it allows the current and voltage waveforms to be shown on the screen of the computer during the execution of the experiments.

5.2 V/f control

The measurements that have been obtained during scalar-controlled operation of the system are presented in this section. The performance of the V/f controller is investigated under two different loads, both during the startup of the system and during steady-state operation of the motor.

5.2.1 Startup performance

An open-loop V/f controller is used for the startup of the PMSM and its performance is studied by monitoring and analyzing the currents and voltages of the VSD and the PMSM.

In order to obtain the drive measurements, the monitoring capabilities of the VSD have been utilized, while the motor measurements have been obtained with the implemented monitoring system, which is based on LabVIEW and CompactRIO.

Startup under full load

For the following startup tests, the load resistance R_{gen} is set equal to its minimum available value ($R_{gen} = 27\ \Omega$), which, according to (5.1), corresponds to the maximum achievable load torque T_L.

The V/f controller is used to accelerate the motor from standstill up to a specified target speed. The startup procedure is repeated for different initial rotor positions, which are randomly selected, and the waveforms of the drive current are presented in Fig. 5.4.

It can be observed that the initial current of the drive is relatively high, which can be attibuted to the static load torque of the system and to the magnetization of the two transformers.

The waveforms of the voltage references that are produced by the drive are presented in Fig. 5.5. Since the VSD uses an open-loop V/f control scheme for the startup of the motor, the commanded voltage is not affected by the actual response of the system. Therefore, the voltage reference waveforms are very similar in all tested cases.

During the performed tests, the voltage output of the VSD is not filtered. According to the discussion in Section 2.2.2, the absence of a filter is expected to result in the presence of high-order harmonics in the voltage that is supplied to the motor. Indeed, this can be

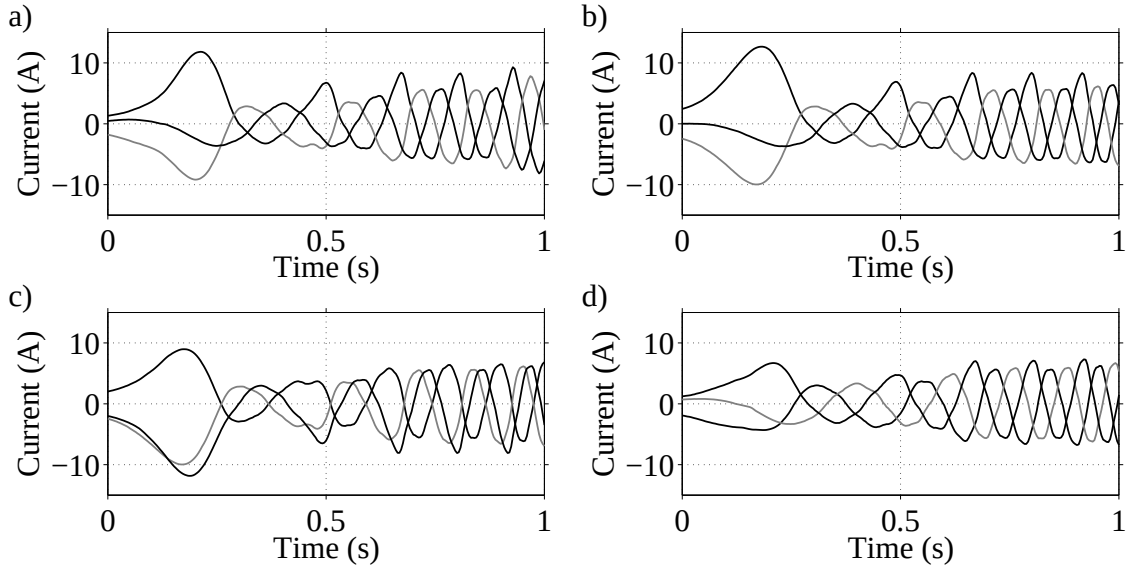

Figure 5.4: Equivalent stator currents i'_{sa}, i'_{sb}, i'_{sc} during startup under full load ($R_{gen} = 27\ \Omega$) for four random initial rotor positions.

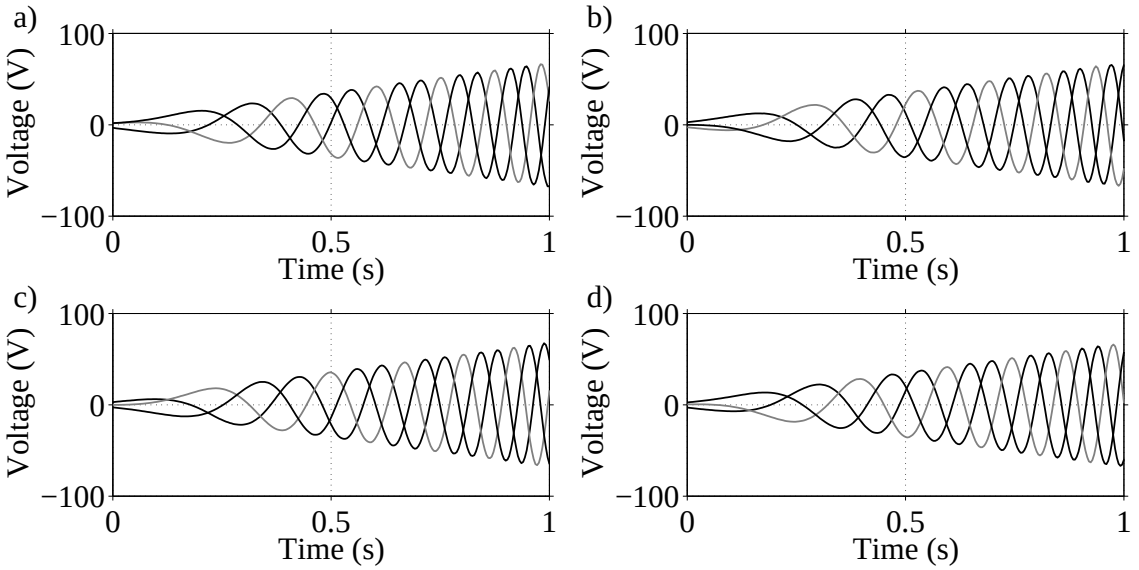

Figure 5.5: Voltage references u^*_{sa}, u^*_{sb}, u^*_{sc} during startup under full load ($R_{gen} = 27\ \Omega$) for four random initial rotor positions.

seen in the waveforms of the stator voltage, which are presented in Fig. 5.6.

By applying a digital low-pass filter on the stator voltage waveforms, most of the high-order voltage harmonics are eliminated. The resulting filtered waveforms are shown in Fig. 5.7.

By comparing Fig. 5.5 and Fig. 5.7, it can be observed that the fundamental component of the voltage that is provided to the motor differs from the voltage reference generated

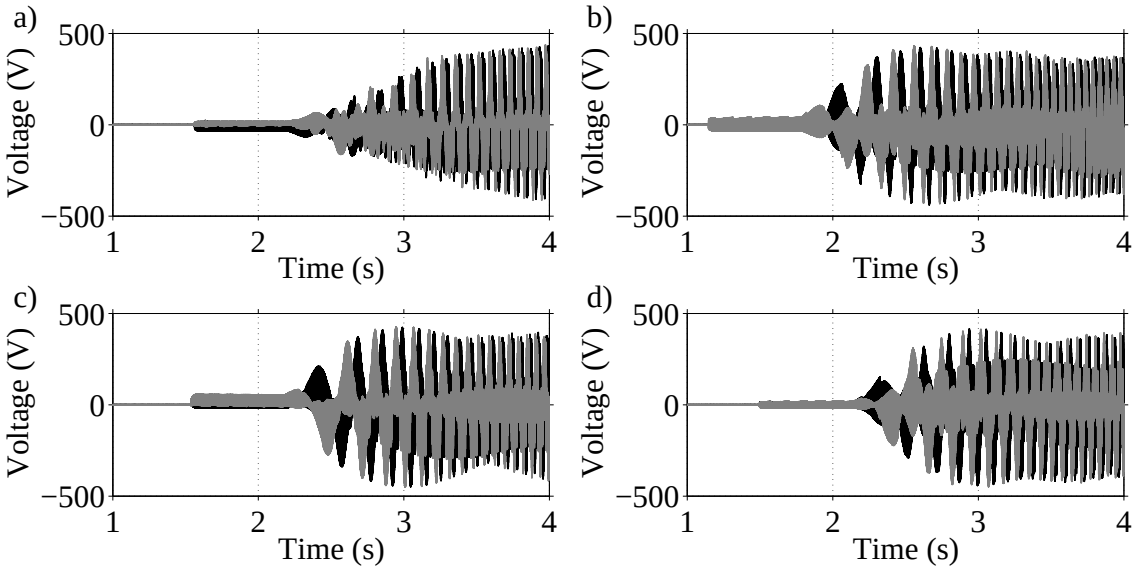

Figure 5.6: Stator voltages u_{sa}, u_{sb} during startup under full load ($R_{gen} = 27\ \Omega$) for four random initial rotor positions.

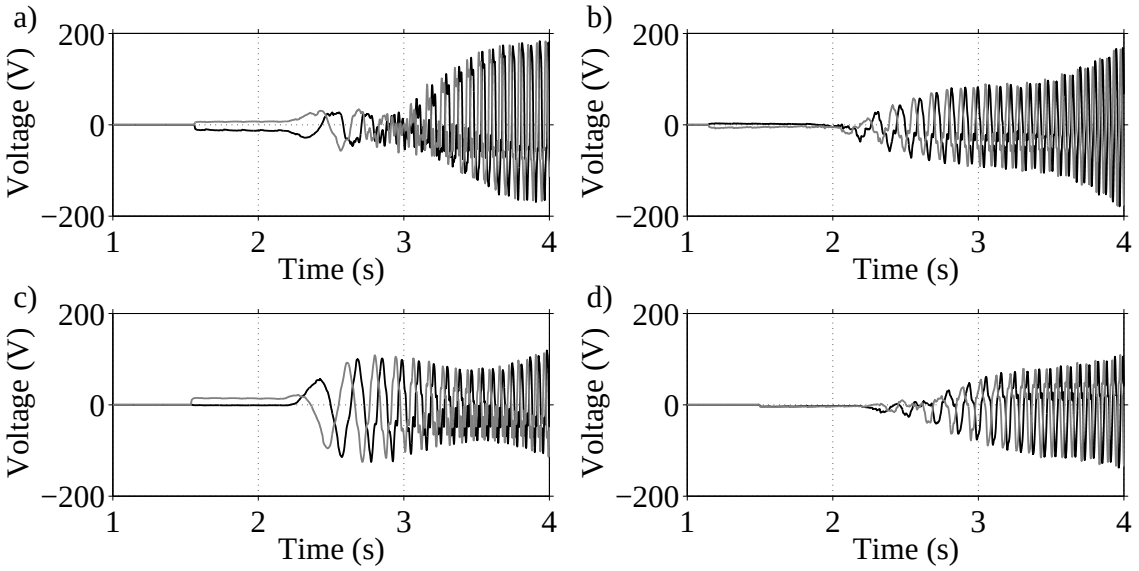

Figure 5.7: Filtered stator voltages u_{sa}, u_{sb} during startup under full load ($R_{gen} = 27\ \Omega$) for four random initial rotor positions.

by the drive. This difference may be attributed to the existence of the transmission system between the VSD and the PMSM.

Most notably, a DC voltage component can be observed in Fig. 5.7 during the initial stage of the startup. The presence of this component results in a initial DC motor current, as can be seen in Fig. 5.8.

By comparing Fig. 5.4 and Fig. 5.8, it can be noticed that the relatively high initial

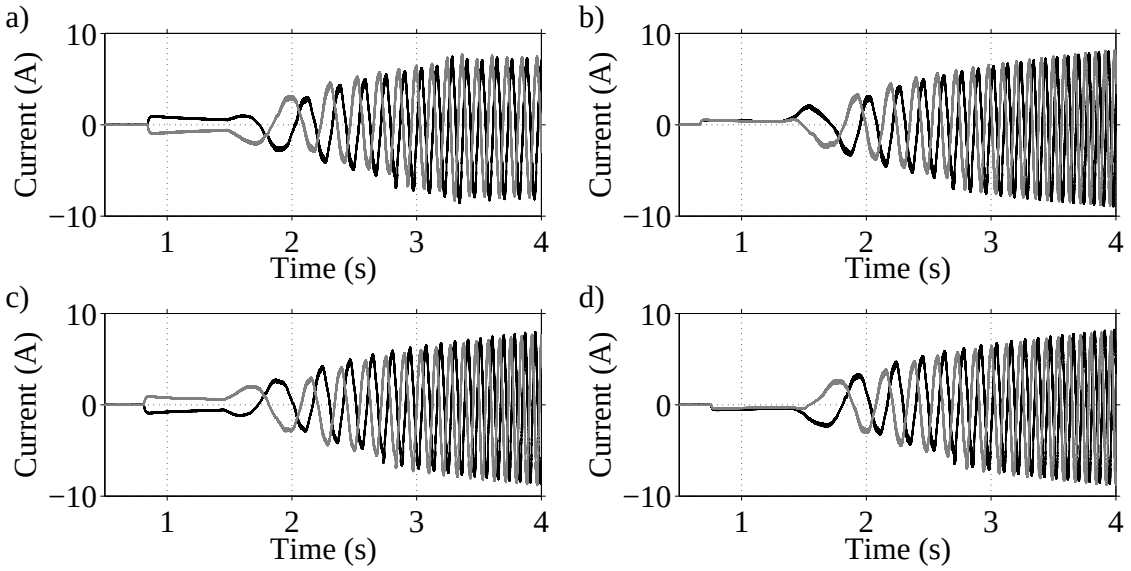

Figure 5.8: Stator currents i_{sa}, i_{sb} during startup under full load ($R_{gen} = 27\ \Omega$) for four random initial rotor positions.

current of the drive does not pass to the motor, but is used for the magnetization of the two transformers.

Startup under reduced load

For the following startup tests, the load resistance is increased to $R_{gen} = 74\ \Omega$, which, according to (5.1), results in a reduced load torque T_L. Once again, the V/f controller is used for the startup of the PMSM from four random initial rotor positions. The obtained waveforms of the motor current are presented in Fig. 5.9.

By comparing Fig. 5.8 and Fig. 5.9, it can be observed that the current values in the case of the reduced load are slightly higher than in the case of the full load.

Although the q-axis current is higher at full load, the motor seems to experience significant overexcitation during reduced-load operation. The state of overexcitation is characterized by an increased stator flux linkage and an increased d-axis current. The high magnetizing current causes the overall stator current to rise in the case of the reduced load.

This observation demonstrates the inability of the V/f controller to operate efficiently under certain load conditions. Since V/f control does not allow direct current control, it cannot prevent the undesirable state of overexcitation under light loading. This was also seen in the simulation results in Section 4.1.1.

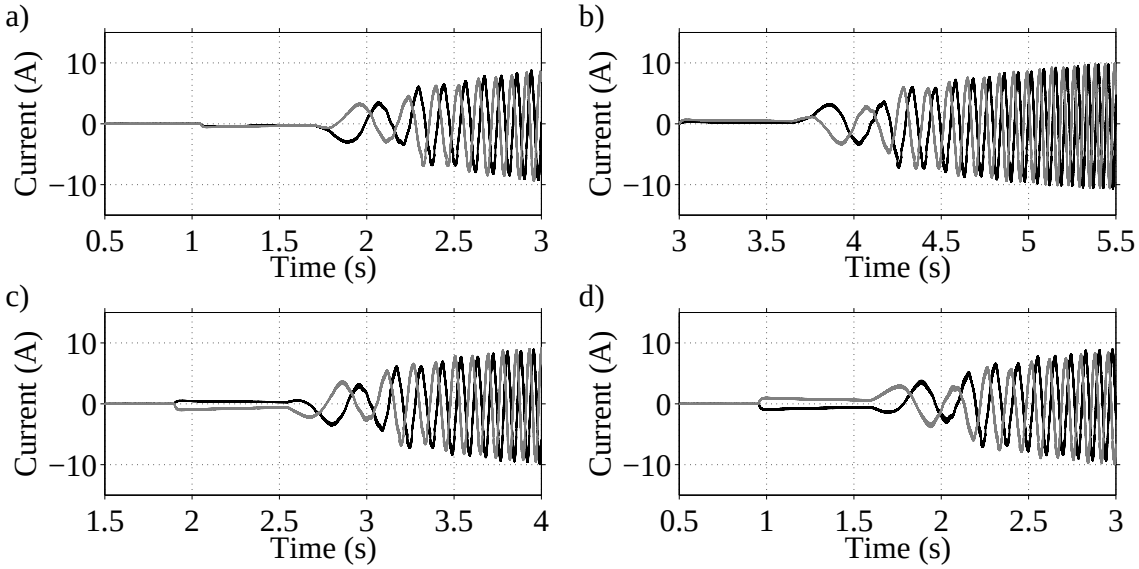

Figure 5.9: Stator currents i_{sa}, i_{sb} during startup under reduced load ($R_{gen} = 74\ \Omega$) for four random initial rotor positions.

As in the case of the full load, a DC current component can be seen in Fig. 5.9 during the initial stage of the startup. The DC current is the result of a similar component in the motor voltage, as can be seen in the filtered voltage waveforms of Fig. 5.10.

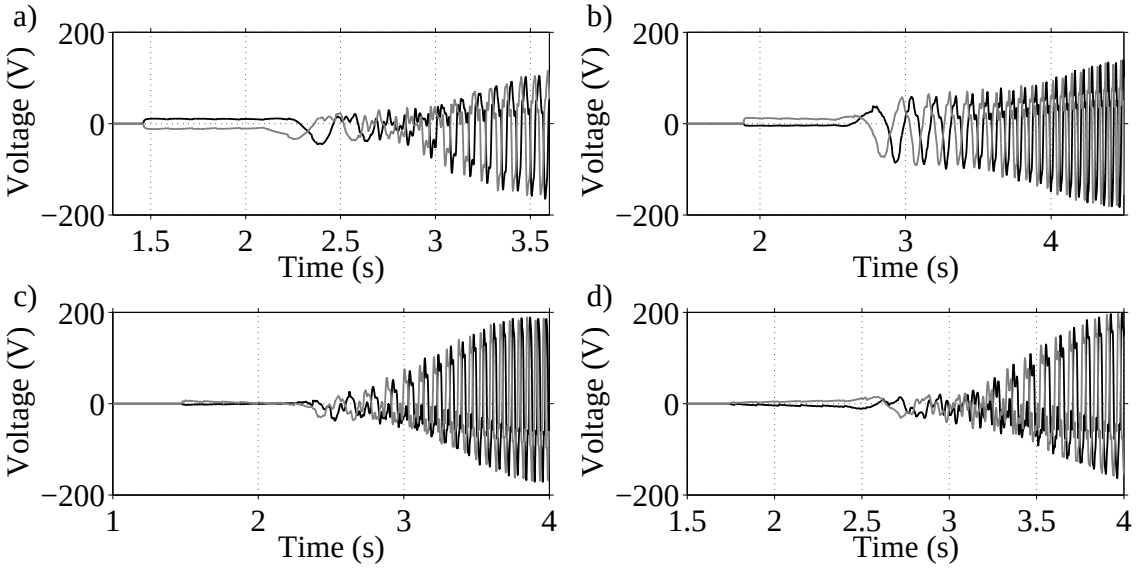

Figure 5.10: Filtered stator voltages u_{sa}, u_{sb} during startup under reduced load ($R_{gen} = 74\ \Omega$) for four random initial rotor positions.

5.2.2 Steady-state operation

For the following tests, the V/f controller is used to accelerate the PMSM from standstill up to different target speeds. The steady-state values of the equivalent stator voltage amplitude $\hat{u'}_s$ and the stator current amplitude $\hat{i}_s$ are measured at six different speeds and under two different loading conditions and are presented in Table 5.1 and Table 5.2.

Table 5.1: Steady-state measurements for operation under full load ($R_{gen} = 27\ \Omega$).

Rotor speed n_r (rpm)	500	1000	1500	2000	2500	3000
Voltage amplitude $\hat{u'}_s$ (V)	57.1	109.9	164.5	222.0	278.5	318.3
Current amplitude $\hat{i}_s$ (A)	7.9	9.9	10.5	10.9	11.9	12.4

Table 5.2: Steady-state measurements for operation under reduced load ($R_{gen} = 74\ \Omega$).

Rotor speed n_r (rpm)	500	1000	1500	2000	2500	3000
Voltage amplitude $\hat{u'}_s$ (V)	57.2	109.1	164.3	216.7	271.7	325.4
Current amplitude $\hat{i}_s$ (A)	8.2	10.3	11.8	11.9	12.5	12.4

Both tables demonstrate that the voltage amplitude produced by the drive is almost proportional to the commanded rotor speed, which is not surprising according to (3.53).

Moreover, it can be observed that the current amplitude increases for higher rotor speeds. According to (5.1), the load torque rises when the speed increases, causing an increase in the torque-producing component of the equivalent stator current and therefore an increase in the overall stator current.

By comparing Table 5.1 and Table 5.2, it can also be noticed that the current values in the case of the full load are lower than in the case of the reduced load. As was discussed in Section 5.2.1, this result can be attributed to the high d-axis current that the motor experiences under light loading.

5.3 Position-sensorless vector control

This section presents the measurements that have been obtained during vector-controlled operation of the system. In the performed tests, the V/f controller is used for the initial acceleration of the PMSM and the position-sensorless vector controller is activated after a certain speed is reached.

Initially, the behaviour of the system is studied after the transition from scalar to vector control. Different torque reference values are used for the vector controller and the tests are repeated with the field-weakening algorithm both activated and deactivated.

The performance of the vector controller after load variations is then tested, by subjecting the PMSM to sudden load increases and decreases. These tests verify that the controlled quantities stay close to their reference values after load disturbances and that the field-weakening mode is entered successfully, when a certain speed is exceeded.

Finally, the performance of the system after sudden torque reference variations is tested, by commanding a rotation reversal, thus by changing the sign of the applied torque reference. This test verifies that the controller responds properly to changes in the ordered torque and that the transition from vector to scalar control and vice versa is performed successfully at low speeds during the reversal.

5.3.1 Control transition

For the following tests, the V/f controller is used to accelerate the PMSM from standstill up to 250 rpm. After a few seconds of steady-state operation at this speed, the control transition takes place, thus the V/f controller is dismissed and the vector controller is deployed.

Initially, the behaviour of the system during the transition is investigated for two different cases. In both cases, the torque reference that is provided to the vector controller is 10 Nm. However, in the first case, the field-weakening function of the drive is deactivated, while in the second one, it is activated when the speed of the PMSM becomes higher than 2400 rpm.

Furthermore, the response of the system after the transition is obtained for different torque reference values and the measured motor currents are used to verify that the vector controller operates properly.

Test without field-weakening

The behaviour of the system during the control transition, when no field-weakening operation is considered, is shown in Fig. 5.11.

It be seen in Fig. 5.11 d) that the estimated electromagnetic torque of the motor during V/f control is approximately equal to 5.5 Nm. After the transition, the torque increases

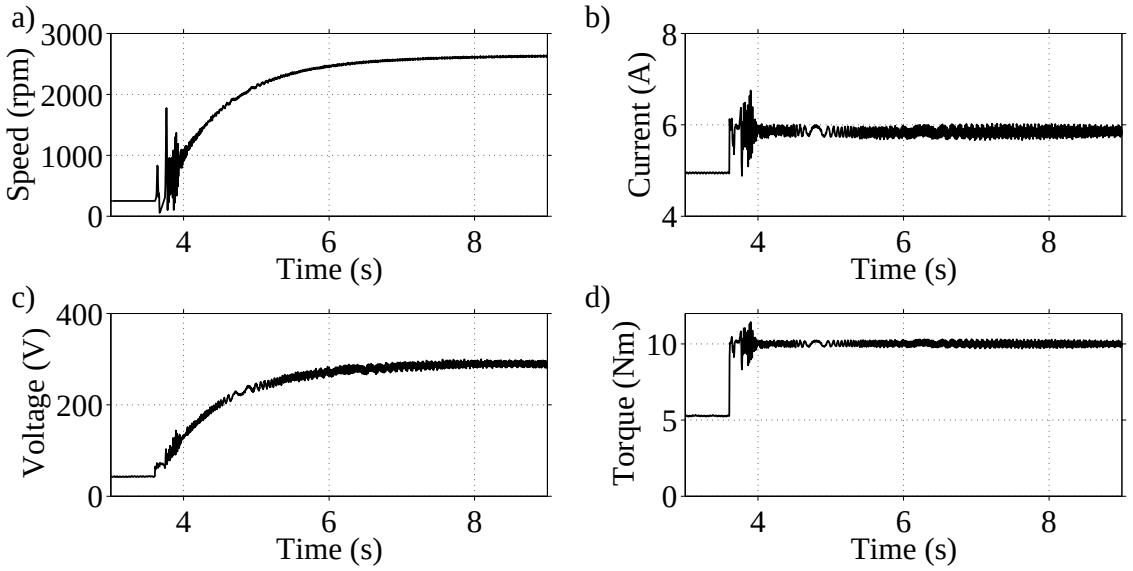

Figure 5.11: Control transition with the field-weakening function deactivated. a) Estimated rotor speed $n_{r,est}$. b) Equivalent stator current magnitude i'_s. c) Equivalent stator voltage magnitude u'_s. d) Estimated electromagnetic torque $T_{e,est}$.

to its reference value of 10 Nm.

Figure 5.11 b) shows that the magnitude of the VSD current before the transition is around 4.9 A, while, after the transition, it becomes approximately equal to 5.9 A.

It can be noticed that although the produced torque is almost 81.8% higher in the case of vector control, the respective increase in the current magnitude is only 20.4%. This demonstrates that much higher torque-to-current ratios can be achieved with vector control.

Figure 5.11 a) shows that after the transition, the estimated rotor speed increases rapidly from 250 rpm to the steady-state value that corresponds to the commanded torque (2620 rpm).

It can be seen in Fig. 5.11 c) that the speed rise is accompanied by an increase in the VSD voltage magnitude. The steady-state value of the voltage magnitude is approximately equal to 290 V.

On the other hand, Fig. 5.11 b) shows that the VSD current magnitude remains constant, since the d-axis and q-axis current references in the vector controller are also constant.

Test with field-weakening

The previous test is performed again, but this time the field-weakening function is activated when the speed exceeds the specified value of 2400 *rpm*. The behaviour of the system in this case is shown in Fig. 5.12.

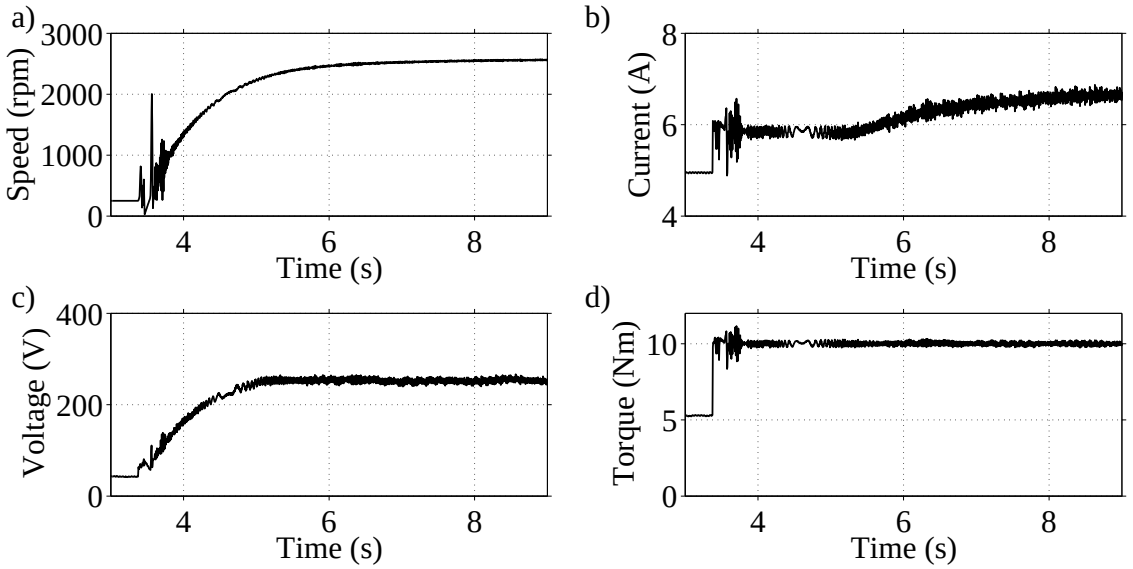

Figure 5.12: Control transition with the field-weakening function activated. a) Estimated rotor speed $n_{r,est}$. b) Equivalent stator current magnitude i'_s. c) Equivalent stator voltage magnitude u'_s. d) Estimated electromagnetic torque $T_{e,est}$.

Figure 5.12 d) demonstrates that the estimated electromagnetic torque after the transition remains constant and equal to its reference value.

As shown in Fig. 5.12 c), the speed rise after the transition is initially achieved through an increase in the voltage magnitude of the VSD. However, when the specified speed value of 2400 *rpm* is reached at approximately 5.5s, the field-weakening function is activated and the voltage magnitude stops increasing.

During the field-weakening operation, a negative d-axis current of increasing magnitude is commanded. This causes a further speed rise after 5.5s, as can be seen in Fig. 5.12 a), but also an increase in the magnitude of the overall VSD current, as shown in Fig. 5.12 b).

Different torque reference values

Next, the performance of the vector controller is tested for different values of the applied torque reference. The waveforms of two measured phase currents during the control tran-

sition are shown in Fig. 5.13 for three different torque reference values.

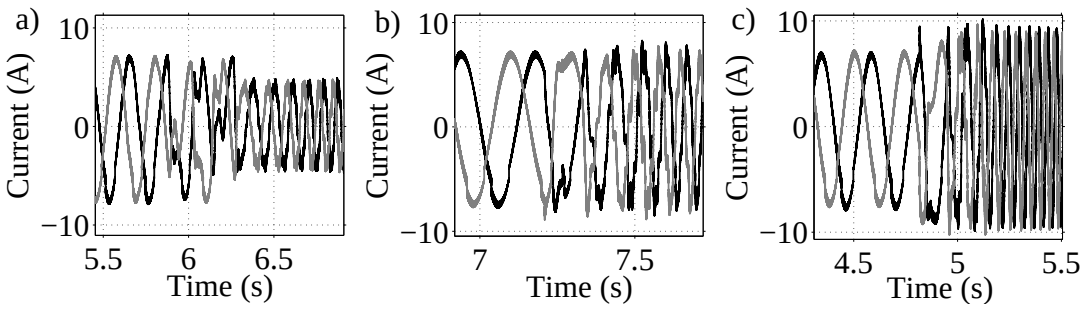

Figure 5.13: Stator currents i_{sa}, i_{sb} for different torque reference values. a) $T_e^* = 5\ Nm$. b) $T_e^* = 8\ Nm$. c) $T_e^* = 10\ Nm$.

Figure 5.13 demonstrates that the control transition is followed by a short interval of current oscillations. These oscillations last for less than $1s$ and, as in the case of the performed simulations, they might result from inaccurate position estimation during the initial interval of the vector-controlled operation.

Since no field-weakening operation is considered, the d-axis current of the motor is expected to be almost zero after the transition, which means that the amplitude of the total stator current is expected to be approximately equal to the q-axis current component.

By using (3.29), the expected stator current amplitude can be calculated for different values of the applied torque reference. The results obtained for 5 Nm, 8 Nm and 10 Nm are approximately 4.4 A, 7.1 A and 8.9 A respectively. These values are close to the current amplitudes after the control transition in Fig. 5.13.

5.3.2 Response to load steps

The aim of the following tests is to study the response of the system to load variations during vector-controlled operation.

According to (5.1), the load torque of the PMSM can be changed, by varying the resistance R_{gen} of the PMSG. In order to achieve a load step-down, the resistance in all three phases is suddenly increased, while a load step-up is obtained through a sudden decrease of the resistance.

For the following tests, the system is ordered to operate in the field-weakening mode, when the speed of the PMSM exceeds the selected value of 2400 rpm.

Load step-down test

For this test, the system operates under vector control with an applied torque reference of $5Nm$. At $4.7s$, a load step-down is applied by increasing the value of the per-phase resistance R_{gen} from 27 Ω to 74 Ω. The response of the system is shown in Fig. 5.14.

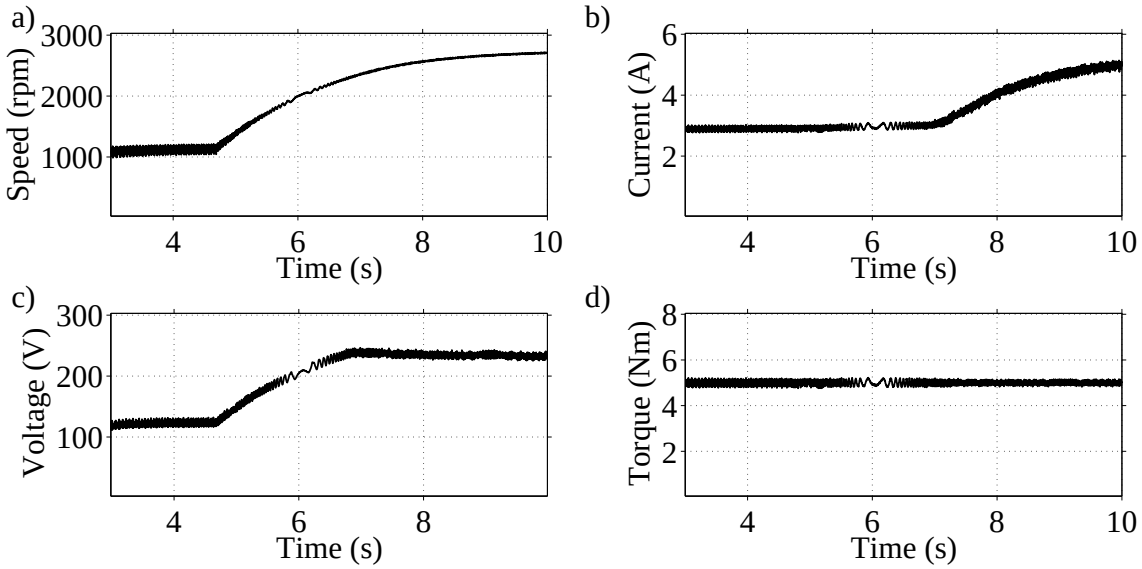

Figure 5.14: Response of the system to a load step-down. a) Estimated rotor speed $n_{r,est}$. b) Equivalent stator current magnitude i'_s. c) Equivalent stator voltage magnitude u'_s. d) Estimated electromagnetic torque $T_{e,est}$.

As shown in Fig. 5.14 d), the electromagnetic torque of the motor does not deviate from its reference value ($5\ Nm$). The resulting torque inbalance after the load step-down causes the motor to accelerate, as shown in Fig. 5.14 a).

The acceleration stops when a new torque balance is established, thus when the load torque becomes equal to the electromagnetic torque of the motor (which is approximately equal to the applied reference torque).

The field-weakening mode is entered around $7.2s$, when the speed of the motor exceeds the selected value of 2400 rpm. At this point, the voltage increase stops, as shown in Fig. 5.14 c), and further acceleration is enabled by a negative d-axis current, which increases the magnitude of the total stator current, as shown in Fig. 5.14 b).

Load step-up test

In this case, a load step-up is applied by decreasing the value of the per-phase resistance R_{gen} from 74 Ω to 27 Ω at $6.8s$. The response of the system is shown in Fig. 5.15.

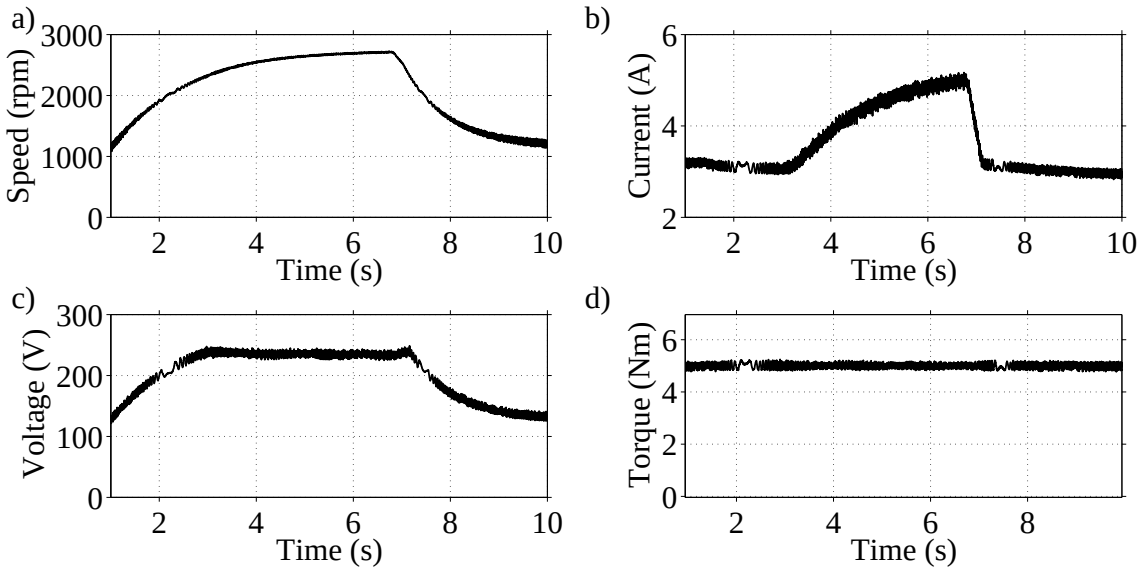

Figure 5.15: Response of the system to a load step-up. a) Estimated rotor speed $n_{r,est}$. b) Equivalent stator current magnitude i'_s. c) Equivalent stator voltage magnitude u'_s. d) Estimated electromagnetic torque $T_{e,est}$.

According to (5.1), since the initial resistance R_{gen} in this test is higher than in the previous one, the system needs to operate at a higher speed, so that a torque balance is established. As this speed exceeds the selected value of 2400 rpm, the field-weakening mode is entered at $3.1s$.

When the load step-up is applied, the resulting torque inbalance causes a speed decrease, as shown in 5.15 a). During the interval that the speed is higher than the field-weakening threshold, the voltage remains almost constant and the deceleration is accompanied by a current decrease, due to the decreasing magnitude of the commanded d-axis current.

However, when the speed becomes lower than 2400 rpm at $7.1s$, the system exits the field-weakening mode and the d-axis current reference remains constant and equal to zero. This causes the magnitude of the total stator current to stay constant, as shown in 5.15 b), and the magnitude of the commanded voltage to fall, as shown in 5.15 c).

Figure 5.15 d) demonstrates that the effect of the load variation on the estimated electromagnetic torque is not significant. This indicates that the current regulator of the vector controller operates properly.

5.3.3 Reversal of rotation

For this test, the system initially operates under vector control with a torque reference of $5Nm$. At $5s$, the commanded torque is reversed, thus a reference of $-5Nm$ is applied and the response of the system is shown in Fig. 5.16.

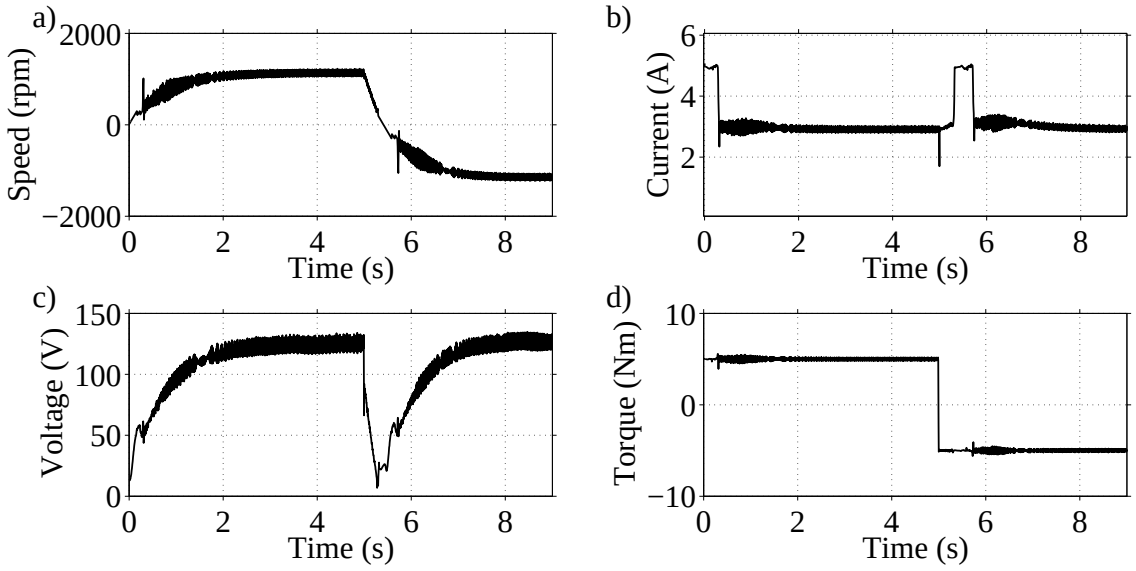

Figure 5.16: Behaviour of the system during a rotation reversal. a) Estimated rotor speed $n_{r,est}$. b) Equivalent stator current magnitude i'_s. c) Equivalent stator voltage magnitude u'_s. d) Estimated electromagnetic torque $T_{e,est}$.

The torque reversal, which is shown in 5.16 d), initially causes the PMSM to slow down. Figure 5.16 c) demonstrates that the deceleration of the motor is accompanied by a decrease in the supplied voltage.

At $5.3s$, an automatic control transition occurs, thus the VSD switches from vector control to V/f control for the low-speed operation of the PMSM.

As can be seen in 5.16 b), the current magnitude of the VSD during the V/f-controlled operation is higher than during the vector-controlled operation, despite the fact that the produced torque is almost equal in both cases.

The torque-to-current ratio in the latter case is approximately 1.73 Nm/A, while in the former case it falls to 1.01 Nm/A. This demonstrates that the vector-controlled operation of the system is significantly more efficient, compared to the V/f-controlled operation.

As discussed earlier, the reason for the superior performance of the vector controller is its ability to directly regulate the supplied current and thus to force its magnetizing com-

ponent to be equal to zero. By eliminating this component, which does not produce any electromagnetic torque, the vector controller maximizes the efficiency of the system.

The speed momentarily becomes zero at $5.5s$ and the motor starts to accelerate in the opposite direction. When the speed exceeds the value of 300 rpm, the VSD automatically switches from V/f control back to vector control.

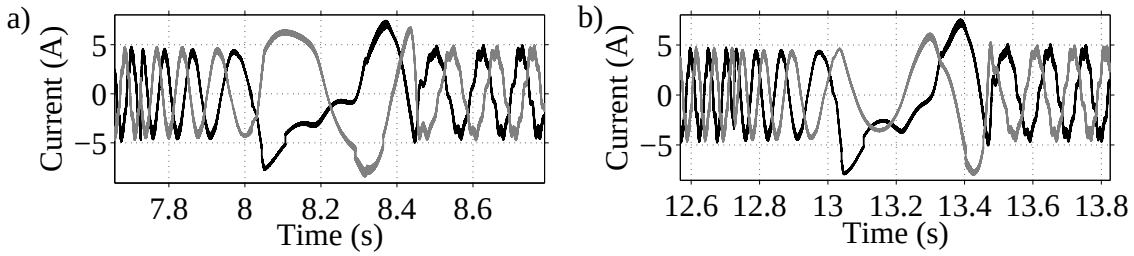

Figure 5.17: Stator currents i_{sa}, i_{sb} during two rotation reversals. a) First reversal. b) Second reversal.

The phase currents of the PMSM during two rotation reversals are shown in Fig. 5.17. Once again, it can be observed that the current amplitude increases during the V/f-controlled operation.

Chapter 6

Conclusions

This chapter summarizes the most important results of the performed simulations and experiments and presents the reached conclusions for each of the implemented control schemes. It also provides some ideas about future work on the studied system and on related topics.

6.1 Open-loop V/f control

The open-loop V/f controller is based on a simple algorithm, which requires no mechanical or electrical feedback. The results of the performed simulations and experiments indicate that this controller can always provide secure startup for the PMSM, if its parameters are properly selected.

The most important parameters of the open-loop V/f controller are the critical frequency, which has been defined as the frequency value below which voltage boosting is applied, and the frequency reference slope. The effect of these parameters on the performance of the system has been investigated, by simulating the startup of the motor for different parameter values.

The obtained results demonstrate that as the critical frequency f_{cr} of the V/f controller increases, the V/f ratio produced by the VSD decreases, but the startup performance of the system deteriorates. Too high values of the critical frequency result in unsuccessful startups, while too low values result in the need for a large topside transformer.

It has been found that the maximum critical frequency that results in successful startup is $f_{cr} \simeq 7.7\ Hz$. This value corresponds to the minimum achievable V/f ratio (12.30 V/Hz), which is equal to 2.5 times the rated ratio of the PMSM (4.90 V/Hz). For the sake of safety, a lower value has been selected for the critical frequency ($f_{cr} = 5.5\ Hz$).

This value corresponds to a V/f ratio of 15.33 V/Hz, which is equal to 3.1 times the rated ratio.

Regarding the frequency reference slope, it has been demonstrated that higher slope values cause more significant torque oscillations and higher speeds in the negative direction. The maximum value that results in successful startup is 15.1 Hz/s, but a much lower slope of 1.5 Hz/s has been selected for the sake of safety.

By performing startup simulations for different initial rotor positions and different loads, it has been observed that the starting angle and the loading conditions of the PMSM affect the startup performance significantly.

Finally, it has been found that the V/f-controlled system is capable of withstanding load disturbances without losing its stability, despite the fact that it experiences significant torque and speed oscillations during the first seconds after the disturbance.

The most important advantages of the implemented open-loop V/f controller are the simplicity of its control algorithm and the absence of feedback, which eliminates the need for current, speed and position sensors. Its most notable disadvantage is the high magnetizing currents that result from the simplistic way it calculates its voltage reference.

6.2 Closed-loop V/f control

Compared to the open-loop scheme, the closed-loop V/f controller has a more complicated structure, but provides more efficient startups for the PMSM. The most important parameter of this controller is the frequency reference slope. Some startup simulations have been performed, in order to determine its effect on the performance of the system.

It has been found that the maximum slope that allows successful startup is 4.3 Hz/s. This value corresponds to the minimum achievable V/f ratio (12.34 V/Hz), which is almost equal to the minimum ratio of the open-loop V/f controller (12.30 V/Hz).

As in the case of the open-loop V/f controller, the selected slope value is 1.5 Hz/s. The maximum V/f ratio that corresponds to this slope is 16.50 V/Hz (3.4 times the rated ratio), which is slightly higher than the corresponding ratio of the open-loop controller (15.33 V/Hz). Therefore, the required size for the topside transformer in the case of closed-loop V/f controller is slightly larger.

Similarly to the open-loop controller, the initial rotor position and the loading conditions of the PMSM affect the startup performance of the system. The response of the closed-loop controller to load disturbances is slightly inferior, despite the demonstrated positive effect of the stabilizer, which has been included in this controller.

The closed-loop V/f controller uses a more advanced algorithm, which requires current measurements, to calculate its reference voltage. Although this increases the complexity of the control structure, it also results in more accurate calculation of the produced voltage reference. As a result, much lower currents than in the case of the open-loop V/f controller are achieved.

6.3 Vector control with position sensor

The simulation results that have been obtained for the vector controller with the position sensor demonstrate its capability to provide fast and accurate control under all tested operating modes.

The proper operation of the designed current regulator has been verified from the response of the controlled currents during a startup test. It has been observed that the q-axis current increases smoothly up to its reference value, without experiencing any overshoots and with a rise time (5.21 ms) which is in good agreement with the bandwidth of the current regulator (439.8 rad/s).

The response of the controller to load disturbances is almost ideal, since the effect of these disturbances on the controlled currents and the electromagnetic torque of the PMSM is negligible.

6.4 Position-sensorless vector control

The performed tests on the sensorless vector controller indicate that the position estimator, which has replaced the mechanical sensors of the previous vector control scheme, is capable of producing accurate estimates shortly after the transition from V/f control to vector control.

By subjecting the vector-controlled system to load variations, it has been verified that the precision of the produced position and speed estimates is not significantly affected by disturbances.

Both the experimental results and the simulation results show that the effect of load steps on the current and the electromagnetic torque of the system is insignificant during vector-controlled operation. This means that the current regulator manages to keep the controlled quantities close to their target values after load variations.

The efficiency and the torque-producing capability of the vector-controlled system when the PMSM operates below its rated speed are optimal, because the d-axis current reference is equal to zero. However, when the field-weakening mode is entered, the efficiency falls as a result of the commanded demagnetizing current.

For the considered pump load, it has been found that the field-weakening algorithm of the vector controller can extend the speed range of the PMSM by up to 17.6%. Since the price that is paid for this extension is a 9.6% decrease in the system efficiency, it would be sensible to use the field-weakening mode only for short time intervals of high-speed operation.

The obtained experimental results also demonstrate the capability of the drive to accelerate the PMSM by producing a demagnetizing current, while keeping its voltage output constant. Similarly to the simulations, this results in a significant increase in the total stator current.

6.5 Future work

Since the focus of this work has been on the development and testing of different control schemes, the modeling of the considered power system has not been handled in detail. Due to the simplified representation of the transmission system in the designed models, phenomena such as the magnetization of the transformers and the charging of the cable have been neglected in the performed simulations.

In the future, the implemented control schemes can be applied on a more precise model of the system. The cable connection can be represented with one or more π-equivalent elements and the magnetizing branch of the transformers can be included in the model.

Furthermore, this thesis has assumed that the voltage at the output of the VSD is sinusoidal and equal to the three-phase voltage reference produced by the implemented controllers. Therefore, the VSD and its output filter have been represented by a simplified interface between the control circuit and the power circuit.

Future work could treat the VSD in a more realistic way. The voltage reference produced by the implemented controllers should enter a PWM stage, where it should be compared with a carrier wave. The result of the comparison should determine the form of the voltage pulses at the output of the VSD.

Finally, most of the control schemes that have been implemented in this thesis are suitable for PMSMs with surface-mounted magnets. For PMSMs with significant dq saliency, the designed models and the developed control algorithms need to be modified. This could be done in the framework of future research.

Bibliography

[1] H. B. Ulvestad, V. Kragset, T. Hollingsæter, S. Alipour, C. Ifrim, H. Allaeddini, and S. Cheng. Long step start up simulations for high speed permanent magnet motors in subsea operations. In *15th International IGTE Symposium*, page 1, Sept. 2012.

[2] D. Saban and A. Artinian. Permanent-magnet motors for sub-sea applications. *Direct Drive Systems Technical Papers*, pages 1–8, 2008.

[3] E. Thibaut, E. Meyer, and P. Bibet. Use of liquid filled motor for subsea pump applications. In *PCIC Europe Conference Record*, pages 1–8, June 2010.

[4] J. Flores, J. Burdick, R. Paes, and E. Fidler. Subsea equipment and applications, a new and emerging technology. In *Petroleum and Chemical Industry Conference Europe*, pages 1–8, June 2011.

[5] S. Chi and L. Xu. Development of sensorless vector control for a PMSM running up to 60,000 rpm. In *IEEE International Conference on Electric Machines and Drives*, pages 834–839, May 2005.

[6] S. Özçira, N. Bekiroğlu, and E. Ayçiçek. Speed control of permanent magnet synchronous motor based on direct torque control method. In *International Symposium on Power Electronics, Electrical Drives, Automation and Motion (SPEEDAM)*, pages 268–272, June 2008.

[7] E. Hamdi. *Permanent magnet and variable reluctance drive systems*. Education and Training International, Chalmers University of Technology, Göteborg, Sweden, 2003.

[8] K. Chau, C. Chan, and C. Liu. Overview of permanent-magnet brushless drives for electric and hybrid electric vehicles. *IEEE Transactions on Industrial Electronics*, 55(6):2246–2257, 2008.

[9] T. Hazel, H. Baerd, J. Bremnes, and J. Legeay. Subsea high-voltage power distribution. In *Petroleum and Chemical Industry Conference*, pages 1–9, 2011.

[10] J. Smith, D. Grant, A. Al-Mashgari, and R. Slater. Operation of subsea electrical submersible pumps supplied over extended length cable systems. *IEE Proceedings on Electric Power Applications*, 147(6):544–552, 2000.

[11] R. Yacamini, W. Phang, P. Brogan, and A. Scott. Variable speed drives for remote downhole pump applications. *Power Engineering Journal*, 14(1):29–36, 2000.

[12] M. Hernes and R. Pittini. Enabling pressure tolerant power electronic converters for subsea applications. In *13th European Conference on Power Electronics and Applications*, pages 1–10, Sept. 2009.

[13] M. Texiera and J. Houdek. Protecting submersible motors from the effects of PWM voltage. In *Brazil Conference for Quality of Electric Energy (CBQEE)*, pages 1–6, 2009.

[14] A. Petterteig, R. Pittini, M. Hernes, and Ø. Holt. Pressure tolerant power IGBTs for subsea applications. In *13th European Conference on Power Electronics and Applications*, pages 1–10, Sept. 2009.

[15] WEG Electrical Equipment, International Division. Induction motors fed by PWM frequency inverters. Technical guide, 2009.

[16] J. Steinke. Use of an LC filter to achieve a motor-friendly performance of the PWM voltage source inverter. *IEEE Transactions on Energy Conversion*, 14(3):649–654, 1999.

[17] ABB Industrial Systems. Effects of AC drives on motor insulation. Technical guide No. 102, 1998.

[18] P. Finlayson. Output filters for PWM drives with induction motors. In *Annual Pulp and Paper Industry Technical Conference*, pages 186–193, June 1997.

[19] K. Haddad. *Output filters for PWM drives*. General Electrics, Transmission, Distribution and Industrial Systems, GE Capacitors and Power Quality Products, New York, USA, 1999.

[20] M. Štulrajter, V. Hrabovcová, and M. Franko. Permanent magnet synchronous motor control theory. *Journal of Electrical Engineering*, 58(2):79–84, 2007.

[21] L. Xu and C. Wang. Implementation and experimental investigation of sensorless control schemes for PMSM in super-high variable speed operation. In *Industry Applications Conference, The 33rd IAS Annual Meeting of the IEEE*, pages 483–489, Oct. 1998.

[22] M. Fatu, R. Teodorescu, I. Boldea, G. Andreescu, and F. Blaabjerg. I-F starting method with smooth transition to EMF based motion-sensorless vector control of PM synchronous motor/generator. In *IEEE Power Electronics Specialists Conference (PESC)*, pages 1481–1487, June 2008.

[23] P. Chandana Perera, F. Blaabjerg, J. Pedersen, and P. Thøgersen. A sensorless, stable V/f control method for permanent-magnet synchronous motor drives. *IEEE Transactions on Industry Applications*, 39(3):783–791, 2003.

[24] A. Mishra, J. Makwana, P. Agarwal, and S. Srivastava. Modeling and implementation of vector control for PM synchronous motor drive. In *International Conference on Advances in Engineering, Science and Management (ICAESM)*, pages 582–585, Mar. 2012.

[25] N. Ertugrul and P. Acarnley. A new algorithm for sensorless operation of permanent magnet motors. *IEEE Transactions on Industry Applications*, 30(1):126–133, 1994.

[26] P. Chandana Perera. *Sensorless control of permanent-magnet synchronous motor drives*. Ph.D thesis, Aalborg University, Institute of Energy Technology, Aalborg, Denmark, Feb. 2002.

[27] P. Acarnley and J. Watson. Review of position-sensorless operation of brushless permanent-magnet machines. *IEEE Transactions on Industrial Electronics*, 53(2):352–362, 2006.

[28] C. French and P. Acarnley. Control of permanent magnet motor drives using a new position estimation technique. *IEEE Transactions on Industry Applications*, 32(5):1089–1097, 1996.

[29] S. Östlund and M. Brokemper. Permanent magnet synchronous motor control theory. *IEEE Transactions on Industry Applications*, 32(5):1158–1165, 1996.

[30] J. Xuewu and L. Yingchao. Field weakening control of PMSM used in an electric power steering system. In *International Conference on Electric Information and Control Engineering (ICEICE)*, pages 2194–2199, Apr. 2011.

[31] M. Zordan, P. Vas, M. Rashed, S. Bolognani, and M. Zigliotto. Field-weakening in vector controlled and DTC PMSM drives, a comparative analysis. In *Eighth International Conference on Power Electronics and Variable Speed Drives (IEE Conf. Publ. No. 475)*, pages 493–499, Sept. 2000.

[32] H. Mahmoudi and A. Lagrioui. Flux-weakening control of permanent magnet synchronous machines. *Journal of Theoretical and Applied Information Technology*, 34(2):110–117, 2011.

[33] R. Doleček, J. Novák, and O. Černý. Traction permanent magnet synchronous motor torque control with flux weakening. *Radioengineering*, 18(4):601–605, 2009.

[34] V. Jevremović and D. Marčetic. A simple closed-loop flux-weakening for permanent magnet synchronous motors. In *14th International Symposium on Power Electronics*, pages 1–4, Nov. 2007.

[35] L. Harnefors. *Control of variable-speed drives*. Applied Signal Processing and Control, Department of Electronics, Mälardalen University, Västerås, Sweden, 2002.

[36] J. Pyrhönen. *Electrical drives*. Department of Electrical Engineering, Lappeenranta University of Technology, Lappeenranta, Finland, 2009.

[37] H. Saadat. *Power System Analysis*. McGraw-Hill Series in Electrical and Computer Engineering, 1999.

[38] N. Mohan, T. Undeland, and W. Robbins. *Power Electronics: Converters, Applications, and Design*. John Wiley and Sons Inc., 1995.

[39] R. Krishnan. Control and operation of PM synchronous motor drives in the field-weakening region. In *Proceedings of the IECON '93., International Conference on Industrial Electronics, Control, and Instrumentation*, pages 745–750, Nov. 1993.

[40] P. Fajkus, B. Klima, and P. Hutak. High speed range field oriented control for permanent magnet synchronous motor. In *International Symposium on Power Electronics, Electrical Drives, Automation and Motion (SPEEDAM)*, pages 225–230, June 2012.